

**Development of Numerical Simulation Codes and
Application to Klystron Efficiency Enhancement**

1997

Kai Masuda

Contents

1. Introduction	1
2. Basic Equations and Assumptions of Numerical Model	7
2.1. Assumptions and General Structure of Simulations	7
2.2. Basic Equations	13
2.2.1. Interactions between Beams and Cavities	13
2.2.2. Focusing Magnetostatic Fields	21
2.2.3. Beam-Induced Electromagnetic Fields	22
2.2.4. Electron Dynamics	27
3. Development of an Improved Finite Element Code for Cylindrically Symmetric Eigenmodes	31
3.1. Introduction	31
3.2. Numerical Methods	33
3.2.1. Weak Formulation	33
3.2.2. Choice of the Independent Variable	35
3.2.3. Finite Element Formulation	37
3.2.4. Finding Eigenfrequencies	39

3.3. Numerical Examinations	41
3.3.1. Comparisons among Three Different Formulations	41
3.3.2. Comparisons between Linear and Quadratic Elements	44
3.3.3. Application to a Klystron Cavity	46
3.4. Concluding Remarks	48
4. Development of a Finite-Element / Boundary-Integral Hybrid Code for Unbounded Magnetostatic Fields with Nonlinear Media	49
4.1. Introduction	49
4.2. Numerical Methods	52
4.2.1. Problem Description	52
4.2.2. Solution Subspace	53
4.2.3. Formulation	55
4.2.4. Energy Functional in the Infinite Space	59
4.2.5. Treatments of Nonlinear Media	61
4.3. Numerical Examinations	62
4.4. Concluding Remarks	69
5. Development of a 2-Dimensional Klystron Simulation Code	71
5.1. Introduction	71
5.2. Numerical Methods	72
5.2.1. Initial and Beam-Injection Conditions	72
5.2.2. Flow Chart	77

5.2.3. A Stabilization Method of Numerical Instabilities in Time-Domain Field Calculations	80
5.2.4. A Method for Fast Convergence in Simulating Beam- Cavity Interactions	86
5.3. Comparisons with Experiments	91
5.4. Concluding Remarks	93
6. Application to Klystron Efficiency Enhancement	95
6.1. Introduction	95
6.2. Direct Energy Recovery from Spent Beams	96
6.2.1. Configuration for Direct Energy Recovery	96
6.2.2. Evaluation of Theoretically Maximum Efficiencies	99
6.2.3. Multistage Depressed Collector Design	103
6.3. Efficiency Enhancement by use of Hollow Beams	106
6.4. Concluding Remarks	108
7. Summary	111
Acknowledgments	115
References	117

Chapter 1

Introduction

Klystrons, originally invented by Hahn and Metcalf, and named by the Varian brothers in 1939 [1], are now widely in use in decades as radio frequency (RF) amplifiers in many applications, such as broadcasting, particle accelerator researches, plasma heating researches, and so on. The klystron amplifies RF power in the regime up to several GHz range by use of an electron beam, consisting of an electron gun to provide the beam, a drift-tube with several RF resonant cavities where the beam interacts with the cavity fields, and, at the end, a collector to dump the spent beam.

From the viewpoint of, in particular, the industrial application of the klystron, the efficiency is a very important key parameter. Especially, the efficiency enhancement is essential to reduce the operating costs in industrial accelerator applications, such as in free electron lasers, transmutation systems of radioactive fission wastes, and so on, since many number of high-power klystrons are or will be used as the CW RF sources.

It is also important for the future fusion application, since the CW klystron is a major and unique candidate for the RF source of the Lower Hybrid Current Drive (several GHz range), and the Fast Wave Current Drive (hundreds MHz), which are both required to make the steady-state operation of the tokamak reactor.

Maximizing the klystron efficiency has been and is still, therefore, a

continuing effort, while the currently designed klystrons based on the conventional technologies seem to have almost achieved theoretically maximum efficiencies, and a drastic breakthrough is called for.

Depressed collector technology is one of such that could overcome this problem with the least degradation in the klystron performance, by directly recovering the substantial energy from the spent electron beam through the decelerating electrostatic fields. The depressed collector is expected to enhance appreciably the klystron efficiency by replacing the existing water-cooled heat-removal collector. In addition, it can be made much smaller than the conventional collector because of greatly reduced heat flux onto the surfaces, in general.

So far, the depressed collector system has been successfully applied to specific klystrons, i.e. medium-power CW klystrons for broadcasting in the 60 kW and 700 MHz range, showing a remarkable efficiency enhancement from the basic efficiency of 50 % of the prototype up to a 70% overall efficiency [2,3].

However, for the currently available several MW klystrons with over 60 % efficiencies without depressed collectors, it is recognized generally difficult to incorporate them successfully, because of much broader energy spreads, higher emittances of the spent electron beams due to higher beam currents, and much stronger interactions with the cavities. Further improvements, therefore, require highly accurate and reliable klystron simulations, and collector design as well.

There is another possibility to enhance the klystron efficiency, which is use of hollow beams instead of the solid beams now preferentially used in the existing klystrons. Since the cavity fields are generally stronger in the vicinity of the cavity gaps on the drift-tube wall rather than those near the

symmetry axis, the hollow beams are supposed to result in higher klystron efficiencies through efficient interactions with the cavities. In order to examine this possibility, 2-dimensional simulations are also essential.

To investigate the above two approaches for the enhancement of the klystron efficiency, a new set of 2-dimensional numerical codes have been developed in this study, and are presented in this thesis. They can simulate effectively the klystrons as well as other RF devices, for example the RF-guns [4-6].

One of the developed codes is for calculating eignemodes of the klystron cavities. So far, many codes have been developed [7-14], and are in use as cavity design tools for many RF devices, such as klystrons, RF-guns, and particle accelerators. However, depending on the cavity geometry or the mode to be solved, they are sometimes not accurate enough, or in other words, take too much CPU time to achieve the required accuracy. For these design tools, both higher accuracy and less computational efforts are always important, and strongly required.

From this viewpoint, a new Finite Element (FE) formulation is proposed as will be described in chapter 3 [15], which aims at improved calculations of cylindrically symmetric modes applicable to the klystron simulations. This new formulation can avoid the singularity on the symmetry axis, and, consequently, it is found that the solutions have higher accuracy and smoother convergence compared with other existing formulations. It should be noted that this numerical technique is applicable not only to the present eigenmode calculations but also to calculations of other cylindrically symmetric solenoidal fields, such as magnetostatic field calculations, and time-domain calculations of electromagnetic fields.

For calculations of magnetostatic fields, the finite methods, such as the Finite Element method (FEM), and the Finite Difference method (FDM), are commonly used, while they have the disadvantage that specific conditions are required on the boundary of the finite meshes. Unfortunately, it is the essential feature of the magnetostatic fields to extend to the infinite space, and accordingly no specific boundary condition is actually available for the finite methods. On the other hand, the integral equation methods, such as the Boundary Element method (BEM) and the Moment method (MM), can effectively deal with the unbounded problems, but they cannot treat nonlinear nor inhomogeneous media.

To calculate the unbounded magnetostatic fields by the klystron focusing coils, a new FEM/MM-hybrid method is proposed in [chapter 4](#), which retains the advantageous characteristics of both methods. It is to be noted that the present FEM/MM-hybrid method can be applied to other problems where Green's functions are known, such as electromagnetic scattering problems, for example.

To model the interaction between the electron beam and the cavities, the equivalent circuit model was used in this study, which is known as the 'port-approximation' originally proposed by Yu [\[16\]](#), and also by Carlsten and Tallerico [\[17\]](#), and effectively utilized in the existing codes [\[18-20\]](#).

The simulation code in this study was developed based on the existing 2-dimensional code known as FCI (acronym for Field Charge Interaction) by Shintake [\[19, 21\]](#), and the following several improvements were made to achieve much higher accuracy sufficient enough to provide injection conditions for the depressed collector designing.

A new method based on the Newmark method is proposed to avoid numerical instabilities in calculating simultaneously the electromagnetic

fields, and the particle motions in time domain.

For a stable calculation, in general, the well-known Courant-Freidrichs condition should be fulfilled, i.e. the spatial meshes must be smaller than a specific size related to the time step. And further in some cases with high beam currents, both spatial smoothing, and artificial damping factors between the output cavity and the collector entrance are required in the field calculation [21]. Damping factors between the output cavity and the collector are suitable for calculating the klystron output power, but are found not suitable in order to calculate the spent beam for depressed collector designing.

The new method of the present study is rather straightforward, and does not require such a condition or treatments, by including damping factors in itself effectively to, eventually, damp the high-frequency fields induced by the numerical errors.

Also, in the port-approximation, since the equivalent circuit shows resonance with a high quality factor including a nonlinear term induced by the electron beam, the final periodically steady-state solution can hardly be obtained straightforwardly [21], and, therefore, some special treatments are required for fast convergence within reasonable computation time [18, 21]. Again a new approach is proposed in this study, and applied to achieve faster convergence in solving the equivalent circuit equations.

The discussions above are summarized as follows.

In this thesis, development of a set of numerical codes, and its application are presented, aiming at efficiency enhancement of klystrons.

In [chapter 2](#), the numerical model for the klystron simulation is reviewed, and assumptions made for efficient computations are summarized.

Also discussed are basic equations for the numerical model, which are derived on the assumptions from Maxwell's equations, and the relativistic equation of motion for electrons.

In [chapter 3](#), a new formulation is proposed for accurate calculations of cylindrically symmetric eigenmodes. Comparisons with the existing formulations are made to show the advantageous features of the new formulation with respect to both accuracy and smooth convergence of the solutions.

In [chapter 4](#), a new code for magnetostatic field calculations is presented, which is to be used for calculating the external focusing fields of klystrons. To deal with the unbounded magnetostatic field problem including nonlinear media, a new hybrid method combining the FEM and the MM is proposed.

In [chapter 5](#), development of the overall klystron simulation code is presented. A new method based on the Newmark method is proposed to provide high numerical stability in solving ordinary differential equations for time-varying electromagnetic fields in particle-in-cell simulations. A new approach is also proposed to achieve fast convergence in solving resonant circuit equations with high quality factors including a nonlinear term induced by the electron beam. Application to some existing klystrons is also presented to show agreements with experiments in terms of RF output powers.

By use of the verified simulation codes developed, the two approaches for the enhancement of the klystron efficiency are investigated in [chapter 6](#) [[22](#), [23](#)].

The discussions in this thesis are summarized in [chapter 7](#).

Chapter 2

Basic Equations and Assumptions of Numerical Model

In [this chapter](#), basic equations are summarized for the code development presented in [the following chapters](#). They are derived from Maxwell's equations, and the relativistic equation of motion for electrons, on some assumptions, mainly, for efficient computations.

2.1. Assumptions and General Structure of Simulations

In this section, the assumptions made for efficient computations in the klystron simulations are summarized [\[19, 21\]](#).

As schematically shown in [Fig. 2.1](#), a klystron consists of an electron gun to provide a electron beam, a drift-tube with input, idler and output cavities to modulate and bunch the electron beam, and a collector to dump the spent beam. Some external coils and pole-pieces are set to provide magnetostatic fields throughout to focus the beam.

In modeling a klystron numerically, some assumptions are made for efficient computations as follows.

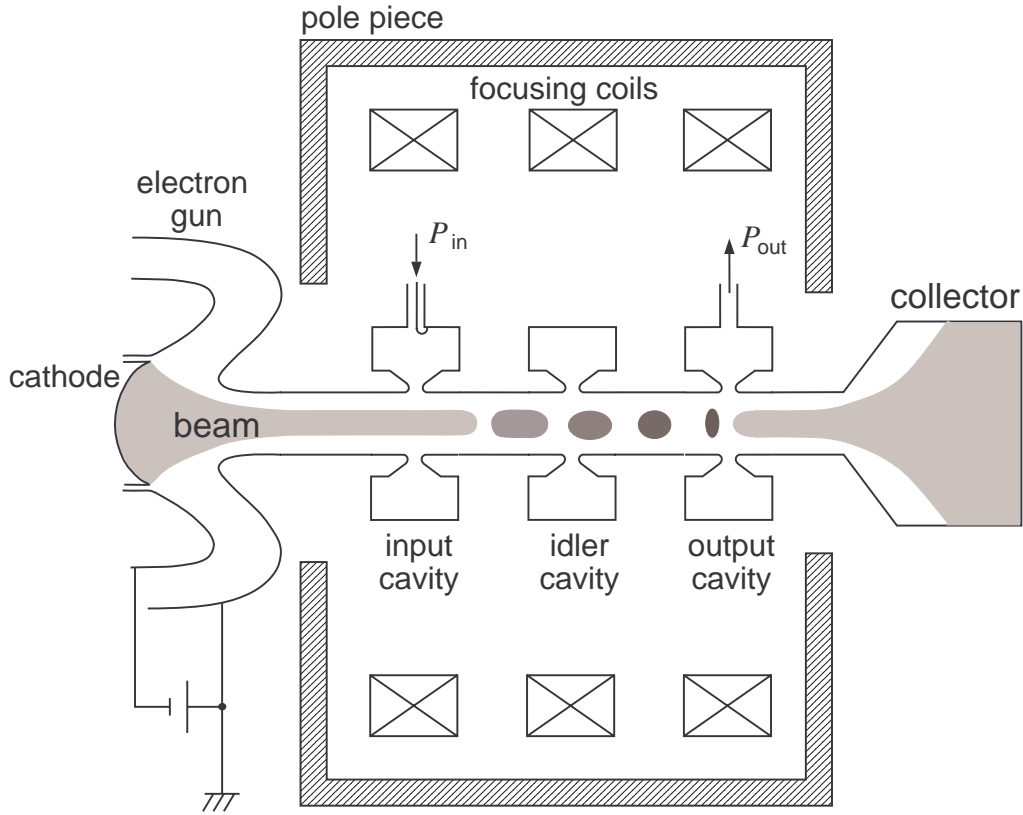


Figure 2.1. Schematic cross section of a klystron.

- (i) The electromagnetic fields are assumed to be cylindrically symmetric (no variation in the θ -direction). This assumption is appropriate since the klystron has almost complete cylindrical symmetry. Although the output cavity has a non-symmetric connection to the output wave-guide, the fields within the drift-tube can be assumed to be symmetric.
- (ii) Accordingly, the electron beam is also assumed to be cylindrically symmetric, consisting of ring particles (see [Fig. 2.2](#)) specified by their positions (z_ν, r_ν) , and velocities $(u_{\nu,z}, u_{\nu,r}, u_{\nu,\theta})$ in the cylindrical coordinates (z, r, θ) , where ν denotes the particle number.

- (iii) The fields in the electron gun are assumed to be static, without backward electromagnetic waves from the downstream drift-tube.
- (iv) It is assumed that, as shown in Fig. 2.3, the fields in the drift-tube can be separated into the resonant cavity fields, and the beam-induced fields. The latter are approximately calculated by solving Maxwell's equations without influence of the cavity configuration.
- (v) It is assumed that only one resonant mode is excited in each cavity, whose resonance frequency is closest to the klystron operating frequency.
- (vi) The cavities have almost no coupling with each other through the drift-tube, and accordingly the cavity fields can be calculated separately as schematically shown in Fig. 2.3.
- (vii) The cavity fields have the same frequency as the RF input, i.e. the operating frequency of the klystron.

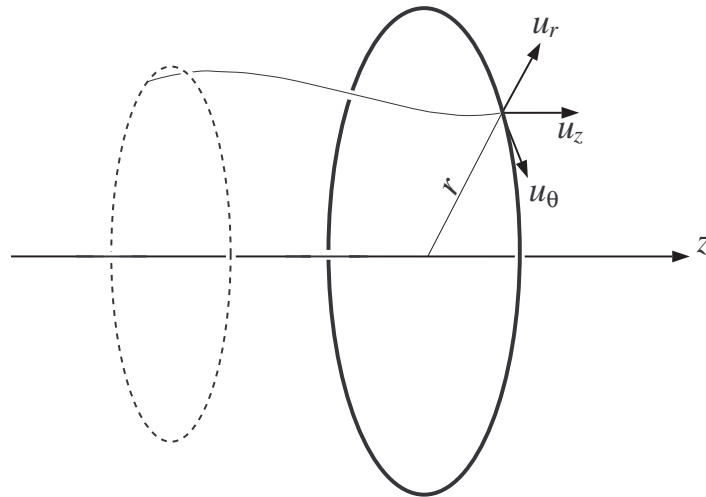
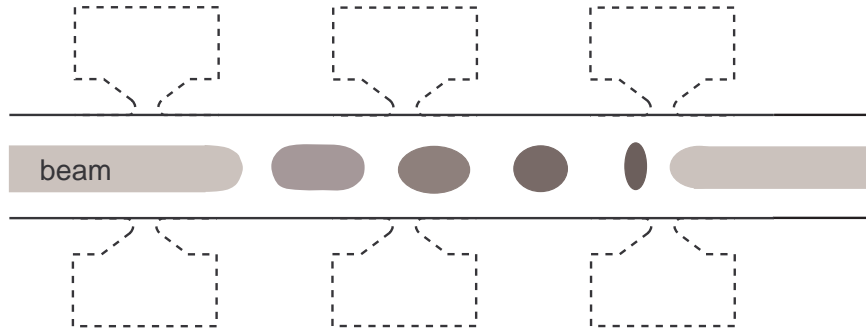


Figure 2.2. A ring particle in 2-dimensional particle simulations. It is specified by its position (z_v, r_v) , and its velocity $(u_{v,z}, u_{v,r}, u_{v,\theta})$.

beam-induced fields



cavity fields

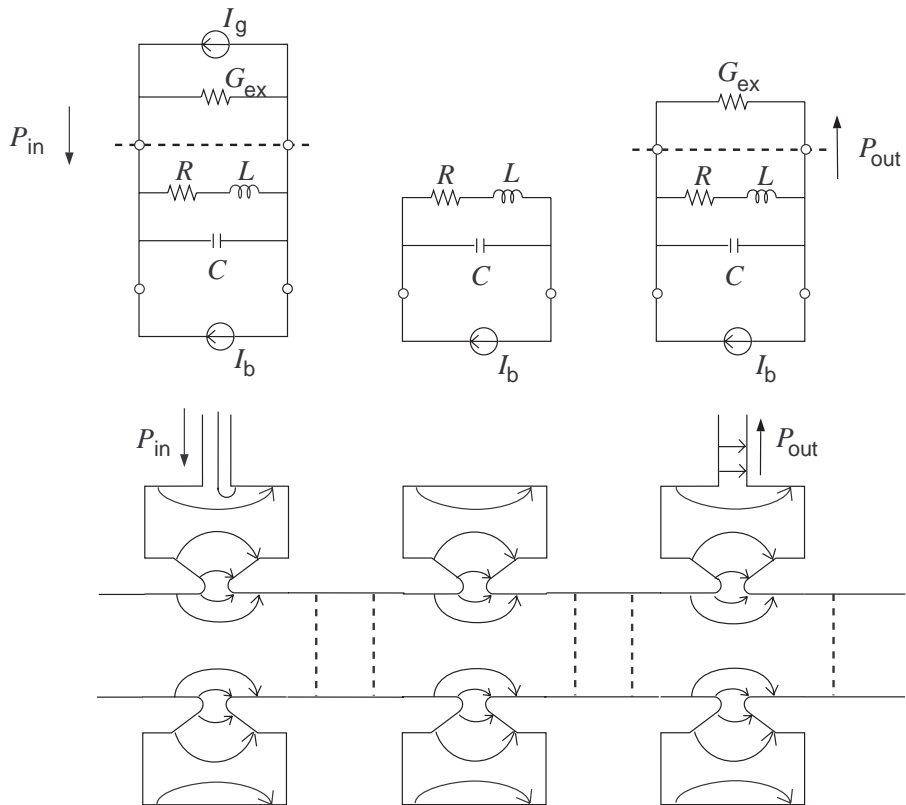


Figure 2.3. The equivalent circuit model. The beam-induced fields and the cavity fields are calculated separately.

On the assumptions above, the following set of codes have been developed in this study (see Fig. 2.4),

- (1) KUSOS (Kyoto University SOlenoidal field Solver),
- (2) KUEMS (Kyoto University EigenMode Solver),
- (3) KUAD2 (Kyoto University Advanced Dart II),
- (4) KUBLAI (Kyoto University Beam Loading AnalysIs).

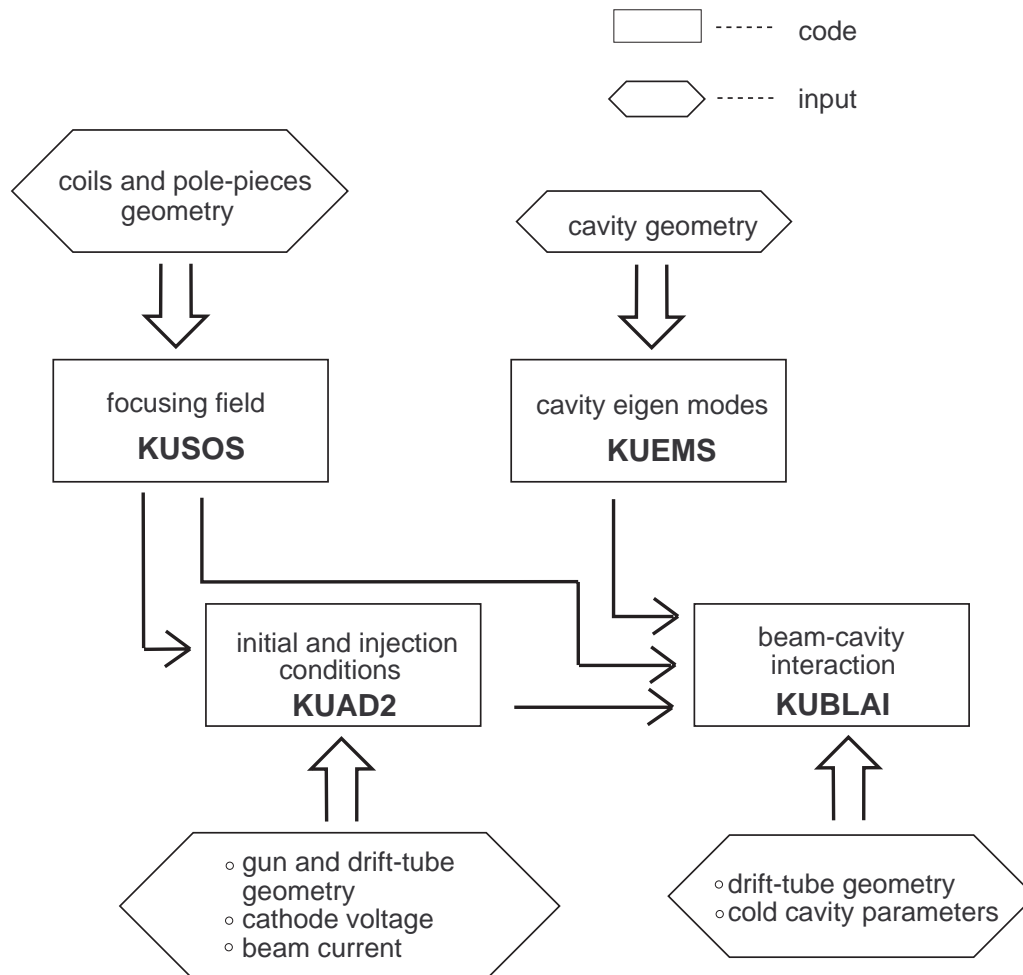


Figure 2.4. The set of codes developed for klystron simulations.

On the assumption (iii), the electron trajectories in the gun are simulated in the electro-magnetostatic fields by the KUAD2, which have been developed by modifying the recently developed KUAD code [24]. Then the results are used as the initial and beam-injection conditions for the beam-cavity interaction simulation in the drift-tube by the KUBLAI.

In the KUBLAI, on the assumption (iv), the fields \mathbf{E} and \mathbf{B} are expressed separately by the components as,

$$\mathbf{E}(z, r, t) = \mathbf{E}_b(z, r, t) + \mathbf{E}_c(z, r, t), \quad (2.1.a)$$

$$\begin{aligned} \mathbf{B}(z, r, t) &= \mathbf{B}_b(z, r, t) + \mathbf{B}_c(z, r, t) + \mathbf{B}_f(z, r) \\ &= \mathbf{B}_{b+c}(z, r, t) + \mathbf{B}_f(z, r), \end{aligned} \quad (2.1.b)$$

where \mathbf{E}_b and \mathbf{B}_b denote the electromagnetic fields induced by the beam, \mathbf{E}_c and \mathbf{B}_c the cavity fields, and \mathbf{B}_f the external focusing fields calculated by the KUSOS.

The beam-induced fields \mathbf{E}_b and \mathbf{B}_b are calculated in time domain by solving Maxwell's equations in the drift-tube without the cavities. On the other hand, on the assumptions (v) and (vi), the cavity fields \mathbf{E}_c and \mathbf{B}_c are expressed by,

$$\mathbf{E}_c(z, r, t) = \sum_i e_0^{(i)}(t) \mathbf{E}_0^{(i)}(z, r), \quad (2.2.a)$$

$$\mathbf{B}_c(z, r, t) = \mu_0 \sum_i h_0^{(i)}(t) \mathbf{H}_0^{(i)}(z, r), \quad (2.2.b)$$

where μ_0 denotes the permeability in vacuum, and $\mathbf{E}_0^{(i)}$ and $\mathbf{H}_0^{(i)}$ denote the dominant eigenmode pattern in the i -th cavity, which are calculated by the KUEMS. The time-dependent variables $e_0^{(i)}$ and $h_0^{(i)}$ (see Eqs. (2.20))

are calculated through the beam-cavity interaction simulations based on the equivalent circuit model shown in [Fig. 2.3](#).

2.2. Basic Equations

2.2.1. Interactions between Beams and Cavities

In this subsection, the equivalent circuit model (see [Fig. 2.3](#)) is derived from Maxwell's equations on the preceding assumptions.

The electromagnetic fields \mathbf{E} and \mathbf{H}_{b+c} ($=\mathbf{B}_{b+c}/\mu_0$) in the klystron are described by Maxwell's equations in vacuum,

$$\nabla \times \mathbf{E} = -\mu_0 \frac{\partial \mathbf{H}_{b+c}}{\partial t}, \quad (2.3.a)$$

$$\nabla \times \mathbf{H}_{b+c} = \varepsilon_0 \frac{\partial \mathbf{E}}{\partial t} + \mathbf{J}_b, \quad (2.3.b)$$

$$\nabla \cdot \mathbf{E} = \frac{\rho_b}{\varepsilon_0}, \quad (2.3.c)$$

$$\nabla \cdot \mathbf{H}_{b+c} = 0, \quad (2.3.d)$$

where \mathbf{J}_b and ρ_b denote, respectively, the current density and the charge density of the electron beam, and ε_0 the permittivity in vacuum. Note that, as described in [Eq. \(2.1.b\)](#), the total magnetic field \mathbf{B} is sum of \mathbf{B}_{b+c} and the focusing field \mathbf{B}_f induced by the focusing coil current density \mathbf{J}_f . The magnetic field \mathbf{H}_{b+c} will be expressed simply as \mathbf{H} hereafter for convenience in the following derivation.

As is well known, any vector function can be divided into two kinds of functions, namely solenoidal and irrotational eigenfunctions [25]. To expand Maxwell's equations, two sets of eigenfunctions $\{\mathbf{E}_a\}$ and $\{\mathbf{H}_a\}$ are defined with different boundary conditions as follows.

$$\mathbf{n} \times \mathbf{E}_a = \mathbf{0} \quad \text{on } \Gamma_1, \quad (2.4.a)$$

$$\mathbf{n} \cdot \mathbf{E}_a = 0 \quad \text{on } \Gamma_2, \quad (2.4.b)$$

$$\int_{\Omega} \mathbf{E}_a \cdot \mathbf{E}_a dV = 2W_a, \quad (2.4.c)$$

$$\int_{\Omega} \mathbf{E}_a \cdot \mathbf{E}_b dV = 0, \quad (2.4.d)$$

$$\mathbf{n} \cdot \mathbf{H}_a = 0 \quad \text{on } \Gamma_1, \quad (2.4.e)$$

$$\mathbf{n} \times \mathbf{H}_a = \mathbf{0} \quad \text{on } \Gamma_2, \quad (2.4.f)$$

$$\int_{\Omega} \mathbf{H}_a \cdot \mathbf{H}_a dV = 2W_a, \quad (2.4.g)$$

$$\int_{\Omega} \mathbf{H}_a \cdot \mathbf{H}_b dV = 0, \quad (2.4.h)$$

where a and b denote mode numbers, Γ_1 the inner surface of the cavity and the drift-tube wall, Γ_2 the cross-sectional area of the input coupler and the output wave guide, Ω the domain surrounded by $\Gamma_1 \cup \Gamma_2$ (see Fig. 2.5), and dV denotes a volume element in Ω . The value W_a in Eqs. (2.4.c) and (2.4.g) gives the normalization condition for the mode a . The set $\{\mathbf{E}_a\}$ and $\{\mathbf{H}_a\}$ each consists of solenoidal and irrotational eigenfunctions.

On one hand, the solenoidal eigefunction can be described by,

$$\nabla \times \mathbf{E}_a = k_a \mathbf{H}_a, \quad (2.5.a)$$

$$\nabla \times \mathbf{H}_a = k_a \mathbf{E}_a, \quad (2.5.b)$$

$$\nabla \cdot \mathbf{E}_a = 0, \quad (2.5.c)$$

$$\nabla \cdot \mathbf{H}_a = 0, \quad (2.5.d)$$

which represent a resonant eigenmode, with a resonance frequency $ck_a/2\pi$, electromagnetic fields $\mathbf{E}_a(z, r)\cos(ck_at)/\sqrt{\epsilon_0}$, $\mathbf{H}_a(z, r)\sin(ck_at)/\sqrt{\mu_0}$, and stored energy W_a , where c is the speed of light, and k_a the wave number.

On the other hand, the irrotational functions satisfy $\nabla \times \mathbf{E}_a = \mathbf{0}$ and $\nabla \times \mathbf{H}_a = \mathbf{0}$, which can be assumed as modes with eigenfrequencies $ck_a/2\pi = 0$, and hence do not contribute to resonant fields.

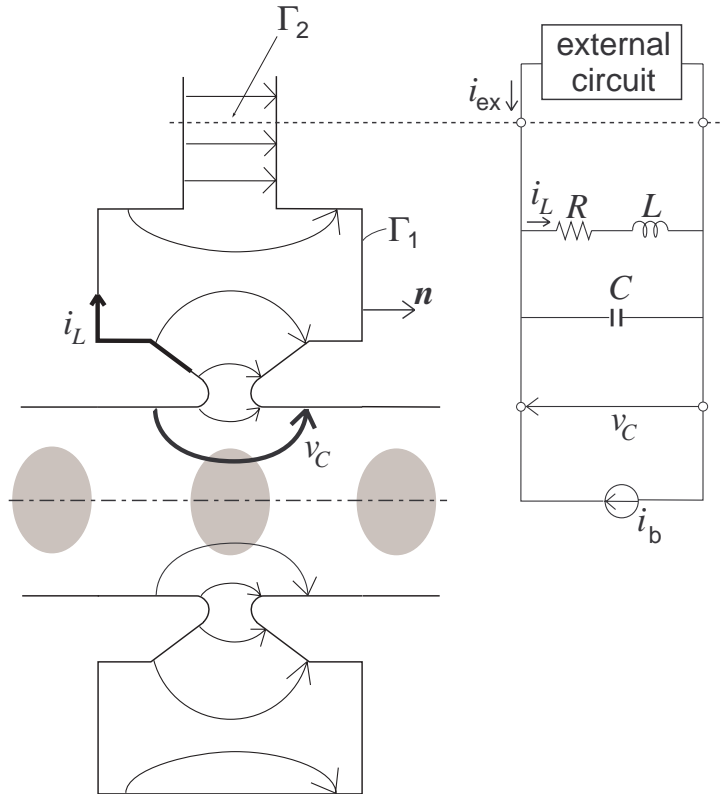


Figure 2.5. The equivalent circuit of the output cavity.

On the assumption (iv) in [section 2.1](#), the eigenfunctions $\{\mathbf{E}_a\}$ and $\{\mathbf{H}_a\}$ are divided into cavity-related solenoidal eigenmodes, and the others, i.e. solenoidal eigenmodes of the drift-tube and all the irrotational eigenfunctions.

Among the former cavity modes, on the assumption (v), only the dominant cavity modes $\{\mathbf{E}_0^{(i)}\}$ and $\{\mathbf{H}_0^{(i)}\}$ are taken into account in the KUBLAI simulations, where i denotes the cavity number, and the subscript ‘0’ means the dominant mode.

Since the beam-induced fields \mathbf{E}_b and \mathbf{B}_b consist of the latter eigenfunctions, and are approximately calculated by solving Maxwell’s equations in time domain without the cavities, the fields can be written by,

$$\mathbf{E}(z, r, t) = \mathbf{E}_b(z, r, t) + \sum_i e_0^{(i)}(t) \mathbf{E}_0^{(i)}(z, r), \quad (2.6.a)$$

$$\mathbf{H}(z, r, t) = \frac{1}{\mu_0} \mathbf{B}_b(z, r, t) + \sum_i h_0^{(i)}(t) \mathbf{H}_0^{(i)}(z, r), \quad (2.6.b)$$

where, from [Eqs. \(2.4.c\), \(2.4.d\), \(2.4.g\) and \(2.4.h\)](#),

$$e_0^{(i)}(t) = \frac{1}{2W_0^{(i)}} \int_{\Omega} \mathbf{E}(z, r, t) \cdot \mathbf{E}_0^{(i)}(z, r) dV, \quad (2.7.a)$$

$$h_0^{(i)}(t) = \frac{1}{2W_0^{(i)}} \int_{\Omega} \mathbf{H}(z, r, t) \cdot \mathbf{H}_0^{(i)}(z, r) dV. \quad (2.7.b)$$

As will be shown below, the equivalent circuit equations for the time-dependent variables $e_0^{(i)}$ and $h_0^{(i)}$ can be derived from Maxwell’s equations of [Eqs. \(2.3.a\) and \(2.3.b\)](#).

By multiplying $\mathbf{H}_0^{(i)}$ and integrating in the domain Ω , Eq. (2.3.a) becomes,

$$\int_{\Omega} \mathbf{H}_0^{(i)} \cdot (\nabla \times \mathbf{E}) dV = -2W_0^{(i)} \mu_0 \frac{dh_0^{(i)}}{dt}. \quad (2.8)$$

With Eq. (2.5.b), the integrand of Eq. (2.8) is reduced to,

$$\begin{aligned} \mathbf{H}_0^{(i)} \cdot (\nabla \times \mathbf{E}) &= \nabla \cdot (\mathbf{E} \times \mathbf{H}_0^{(i)}) + \mathbf{E} \cdot (\nabla \times \mathbf{H}_0^{(i)}) \\ &= \nabla \cdot (\mathbf{E} \times \mathbf{H}_0^{(i)}) + k_0^{(i)} \mathbf{E} \cdot \mathbf{E}_0^{(i)}. \end{aligned} \quad (2.9)$$

Then Eq. (2.8) becomes, with Gauss' divergence theorem and Eq. (2.4.f),

$$2W_0^{(i)} \left(-\omega_0^{(i)} \sqrt{\varepsilon_0} e_0^{(i)} - \frac{d(\sqrt{\mu_0} h_0^{(i)})}{dt} \right) = \int_{\Gamma_1} \left(\mathbf{E} \times \frac{\mathbf{H}_0^{(i)}}{\sqrt{\mu_0}} \right) \cdot \mathbf{n} dS, \quad (2.10.a)$$

where $\omega_0^{(i)} = ck_0^{(i)}$, and \mathbf{n} denotes the outward unit vector normal to $\Gamma_1 \cup \Gamma_2$, and dS denotes a surface element on $\Gamma_1 \cup \Gamma_2$. From Eq. (2.3.b), in the same way with Eqs. (2.4.a) and (2.5.a), the following equation is also obtained.

$$2W_0^{(i)} \left(-\omega_0^{(i)} \sqrt{\mu_0} h_0^{(i)} + \frac{d(\sqrt{\varepsilon_0} e_0^{(i)})}{dt} \right) = -\int_{\Omega} \mathbf{J} \cdot \frac{\mathbf{E}_0^{(i)}}{\sqrt{\varepsilon_0}} dV - \int_{\Gamma_2} \left(\frac{\mathbf{E}_0^{(i)}}{\sqrt{\varepsilon_0}} \times \mathbf{H} \right) \cdot \mathbf{n} dS. \quad (2.10.b)$$

With the following relations,

$$v_C^{(i)}(t) = V_0^{(i)} \sqrt{\varepsilon_0} e_0^{(i)}(t), \quad (2.11.a)$$

$$i_L^{(i)}(t) = -\frac{2W_0^{(i)} \omega_0^{(i)}}{V_0^{(i)}} \sqrt{\mu_0} h_0^{(i)}(t), \quad (2.11.b)$$

$$C^{(i)} = \frac{2W_0^{(i)}}{(V_0^{(i)})^2}, \quad (2.11.c)$$

$$L^{(i)} = \frac{(V_0^{(i)})^2}{2W_0^{(i)}(\omega_0^{(i)})^2}, \quad (2.11.d)$$

$$R^{(i)}i_L^{(i)}(t) = -\frac{V_0^{(i)}}{2W_0^{(i)}\omega_0^{(i)}} \int_{\Gamma_1} \left(\mathbf{E} \times \frac{\mathbf{H}_0^{(i)}}{\sqrt{\mu_0}} \right) \cdot \mathbf{n} dS, \quad (2.11.e)$$

$$i_b^{(i)}(t) = -\frac{1}{V_0^{(i)}} \int_{\Omega} \mathbf{J}_b \cdot \frac{\mathbf{E}_0^{(i)}}{\sqrt{\epsilon_0}} dV, \quad (2.11.f)$$

$$i_{\text{ext}}^{(i)} = -\frac{1}{V_0^{(i)}} \int_{\Gamma_2} \left(\frac{\mathbf{E}_0^{(i)}}{\sqrt{\epsilon_0}} \times \mathbf{H} \right) \cdot \mathbf{n} dS, \quad (2.11.g)$$

where $V_0^{(i)}$ is given by,

$$V_0^{(i)} = -\int_{r=0} \frac{E_{0,z}^{(i)}}{\sqrt{\epsilon_0}} dz, \quad (2.12)$$

Eqs. (2.10.a) and (2.10.b) are, respectively, expressed as,

$$v_C^{(i)} = L^{(i)} \frac{di_L^{(i)}}{dt} + R^{(i)}i_L^{(i)}, \quad (2.13.a)$$

$$C^{(i)} \frac{dv_C^{(i)}}{dt} + i_L^{(i)} = i_b^{(i)} + i_{\text{ext}}^{(i)}, \quad (2.13.b)$$

which describe the equivalent circuit shown in [Fig. 2.5](#).

The major circuit parameters, such as the voltage $v_C^{(i)}$ provided to the capacitance $C^{(i)}$, the power loss at the resistance $R^{(i)}$, the power provided by $i_b^{(i)}$ (called beam-loading current), and the power by $i_{\text{ext}}^{(i)}$ which appears only in the input and output cavities, are, respectively, expressed

from Eqs. (2.11) and (2.12) by,

$$v_C^{(i)} = -\int_{r=0} e_0^{(i)} E_{0,z}^{(i)} dz, \quad (2.14.a)$$

$$R^{(i)} (i_L^{(i)})^2 = \int_{\Gamma_1} \{ \mathbf{E} \times (h_0^{(i)} \mathbf{H}_0^{(i)}) \} \cdot \mathbf{n} dS, \quad (2.14.b)$$

$$i_b^{(i)} v_C^{(i)} = -\int_{\Omega} \mathbf{J}_b \cdot (e_0^{(i)} \mathbf{E}_0^{(i)}) dV, \quad (2.14.c)$$

$$i_{\text{ext}}^{(i)} v_C^{(i)} = -\int_{\Gamma_2} \{ (e_0^{(i)} \mathbf{E}_0^{(i)}) \times \mathbf{H} \} \cdot \mathbf{n} dS. \quad (2.14.d)$$

The parameters above are, thus, found to represent, respectively, the cavity voltage, the wall loss on Γ_1 , the power provided by the electron beam, and the power through Γ_2 .

For the input cavity ($i=1$) and the output cavity ($i=N$), $\{i_{\text{ext}}^{(i)}\}$ are given in terms of the RF input current I_g , and the external load $G^{(i)}$ as,

$$i_{\text{ext}}^{(1)} = I_g \sin(\omega t) - G^{(1)} v_C^{(1)}, \quad (2.15.a)$$

$$i_{\text{ext}}^{(N)} = -G^{(N)} v_C^{(N)}, \quad (2.15.b)$$

$$i_{\text{ext}}^{(i)} = 0 \quad (i=2, \dots, N-1), \quad (2.15.c)$$

where f ($=\omega/2\pi$) is the operating frequency of the klystron.

With the above, the equivalent circuits previously shown in Fig. 2.3 are, thus, derived.

The circuit parameters $L^{(i)}$, $C^{(i)}$, $R^{(i)}$, and $G^{(i)}$ are given from the following equations by experimentally measured cavity parameters; the dominant resonance frequency $f_0^{(i)} = \omega_0^{(i)}/2\pi$, the loaded and unloaded quality factors $Q_l^{(i)}$ and $Q_u^{(i)}$, and the R/Q-parameter $(R/Q)^{(i)}$,

$$\omega_0^{(i)} = \frac{1}{\sqrt{L^{(i)}C^{(i)}}}, \quad (2.16.a)$$

$$(R/Q)^{(i)} = \frac{1}{\omega_0^{(i)}C^{(i)}}, \quad (2.16.b)$$

$$\frac{1}{Q_1^{(i)}} = \frac{1}{Q_u^{(i)}} + \frac{1}{Q_{\text{ext}}^{(i)}}, \quad (2.16.c)$$

$$Q_u^{(i)} = \frac{\omega_0^{(i)}L^{(i)}}{R^{(i)}}, \quad (2.16.d)$$

$$Q_{\text{ext}}^{(i)} = \frac{\omega_0^{(i)}C^{(i)}}{G^{(i)}}, \quad (2.16.e)$$

where the R/Q-parameter $(R/Q)^{(i)}$ is defined in terms of the unloaded quality factor $Q_u^{(i)}$, and the shunt impedance $R_s^{(i)}$ by,

$$(R/Q)^{(i)} = \frac{R_s^{(i)}}{Q_u^{(i)}} = \frac{(V_0^{(i)})^2}{2\omega_0^{(i)}W_0^{(i)}}. \quad (2.17)$$

Finally, on the assumption (vii), with the complex beam-loading current defined by,

$$I_b^{(i)} = \frac{2}{T} \int_0^{1/f} i_b^{(i)}(t) \exp(-j\omega t) dt, \quad (2.18)$$

the equivalent circuit equations of [Eqs. \(2.13\) and \(2.15\)](#) are solved for the operating frequency f in terms of the real part of the following complex values $V_C^{(i)}$ and $I_L^{(i)}$,

$$v_C^{(i)} = \text{Re}[V_C^{(i)} \exp(j\omega t)], \quad (2.19.a)$$

$$i_L^{(i)} = \text{Re}[I_L^{(i)} \exp(j\omega t)]. \quad (2.19.b)$$

Then, from Eqs. (2.11.a), (2.11.b) and (2.17), $e_0^{(i)}$ and $h_0^{(i)}$ are consequently given by,

$$e_0^{(i)}(t) = \frac{1}{\sqrt{\epsilon_0}} \frac{1}{V_0^{(i)}} \operatorname{Re}[V_C^{(i)} \exp(j\omega t)], \quad (2.20.a)$$

$$h_0^{(i)}(t) = -\sqrt{\mu_0} \frac{(R/Q)^{(i)}}{V_0^{(i)}} \operatorname{Re}[I_L^{(i)} \exp(j\omega t)]. \quad (2.20.b)$$

Accordingly, the cavity fields \mathbf{E}_c and \mathbf{B}_c in Eqs. (2.2) are now given by,

$$\mathbf{E}_c(z, r, t) = \frac{1}{\sqrt{\epsilon_0}} \sum_i \frac{1}{V_0^{(i)}} \operatorname{Re}[V_C^{(i)} \exp(j\omega t)] \mathbf{E}_0^{(i)}(z, r), \quad (2.21.a)$$

$$\mathbf{B}_c(z, r, t) = -\sqrt{\mu_0} \sum_i \frac{(R/Q)^{(i)}}{V_0^{(i)}} \operatorname{Re}[I_L^{(i)} \exp(j\omega t)] \mathbf{H}_0^{(i)}(z, r), \quad (2.21.b)$$

2.2.2. Focusing Magnetostatic Fields

The focusing field \mathbf{B}_f can be described in terms of the vector potential \mathbf{A}_f by,

$$\nabla \times \left(\frac{1}{\mu} \nabla \times \mathbf{A}_f \right) = \mathbf{J}_f, \quad (2.22.a)$$

$$\mathbf{B}_f = \nabla \times \mathbf{A}_f, \quad (2.22.b)$$

where \mathbf{J}_f is the current density in the focusing coils. As will be described in chapter 4, the KUSOS solves Eq. (2.22.a) in the infinite space without any

boundary condition, taking into account nonlinear permeability μ as a function of $|\mathbf{B}_f|$ inside the pole-pieces.

2.2.3. Beam-Induced Electromagnetic Fields

As was described in [subsection 2.2.1](#), the beam-induced fields \mathbf{E}_b and \mathbf{B}_b are described by Maxwell's equations in vacuum without influence of the cavity configuration,

$$\nabla \times \mathbf{E}_b = -\frac{\partial \mathbf{B}_b}{\partial t}, \quad (2.23.a)$$

$$\nabla \times \mathbf{B}_b = \frac{1}{c^2} \frac{\partial \mathbf{E}_b}{\partial t} + \mu_0 \mathbf{J}_b, \quad (2.23.b)$$

$$\nabla \cdot \mathbf{E}_b = \frac{\rho_b}{\epsilon_0}, \quad (2.23.c)$$

$$\nabla \cdot \mathbf{B}_b = 0. \quad (2.23.d)$$

On the assumption of cylindrical symmetry, the fields \mathbf{E}_b and \mathbf{B}_b can be written as follows without loss of generality,

$$\mathbf{E}_b = -\nabla \phi_b - \frac{\partial (A_{b,\theta} \mathbf{i}_\theta)}{\partial t} - \nabla \times (G_{b,\theta} \mathbf{i}_\theta), \quad (2.24.a)$$

$$\mathbf{B}_b = B_{b,\theta} \mathbf{i}_\theta + \nabla \times (A_{b,\theta} \mathbf{i}_\theta), \quad (2.24.b)$$

where \mathbf{i}_θ is the unit vector in the θ -direction. The potentials ϕ_b and $A_{b,\theta}$ are, respectively, the scalar and vector potential in Coulomb gauge. The variable $G_{b,\theta}$ in [Eq. \(2.24.a\)](#) gives the other potentials $A_{b,z}$ and $A_{b,r}$ as,

$$\frac{\partial(\mathbf{A}_b - A_{b,\theta}\mathbf{i}_\theta)}{\partial t} = \nabla \times (G_{b,\theta}\mathbf{i}_\theta). \quad (2.25)$$

It is to be note that $\nabla \cdot (\mathbf{A}_b - A_{b,\theta}\mathbf{i}_\theta) = 0$ in Coulomb gauge.

Instead of the common choice of the potentials in Coulomb gauge, Lorentz gauge [19, 21], or electromagnetic fields themselves [20], this choice of the independent variables is exclusively due to the fact that scalar and θ -components of vector variables are much easier to handle on the boundary than the other z - and r -components, in the cylindrical coordinates. It is to be noted that z - and r -components do couple to each other on the drift-tube wall except for a straight drift-tube, while the variables in Eqs. (2.24) do not for any arbitrary boundary shapes.

The fields \mathbf{E}_b and \mathbf{B}_b given by Eqs. (2.24) satisfy both Eq. (2.23.d) and the θ -component of Eq. (2.23.a). From the other Eqs. (2.23), equations for ϕ_b , $A_{b,\theta}$, $B_{b,\theta}$, and $G_{b,\theta}$ are derived as follows,

$$\nabla^2 \phi_b = -\frac{\rho_b}{\epsilon_0}, \quad (2.26.a)$$

$$\nabla \times \nabla \times (A_{b,\theta}\mathbf{i}_\theta) + \frac{1}{c^2} \frac{\partial(A_{b,\theta}\mathbf{i}_\theta)}{\partial t} = \mu_0 J_{b,\theta}\mathbf{i}_\theta, \quad (2.26.b)$$

$$\nabla \times \nabla \times (B_{b,\theta}\mathbf{i}_\theta) + \frac{1}{c^2} \frac{\partial(B_{b,\theta}\mathbf{i}_\theta)}{\partial t} = \mu_0 \nabla \times (\mathbf{J}_b - J_{b,\theta}\mathbf{i}_\theta), \quad (2.26.c)$$

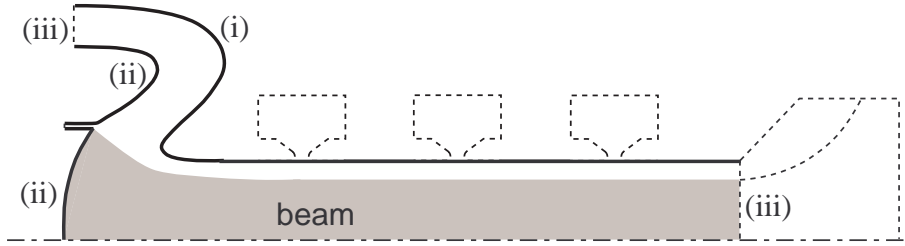
$$\nabla \times \nabla \times (G_{b,\theta}\mathbf{i}_\theta) = \frac{\partial(B_{b,\theta}\mathbf{i}_\theta)}{\partial t}. \quad (2.26.d)$$

In the KUBLAI, $A_{b,\theta}$ and $B_{b,\theta}$ are calculated by solving Eqs. (2.26.b) and (2.26.c) in time domain, while ϕ_b and $G_{b,\theta}$ (Eqs. (2.26.a) and (2.26.d)) are also calculated at each time step, from ρ_b and $\partial B_{b,\theta}/\partial t$ at that time.

The boundary conditions for the beam-induced fields in the KUBLAI are summarized in Fig. 2.6(b).

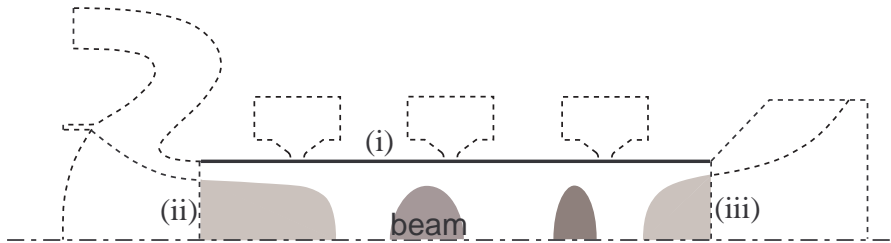
On the injection boundary, the condition $\partial/\partial t = 0$ is applied with the initial potentials given by gun simulation results by the KUAD2, on the assumption (iii) in section 2.1.

- (i) $\phi_b = 0$
- (ii) $\phi_b = -V_b$
- (iii) $\mathbf{n} \cdot \nabla \phi_b = 0$



(a) Static fields (KUAD2).

- (i) $\phi_b = 0, \frac{\partial A_{b,\theta}}{\partial t} = 0, \mathbf{n} \times \{\nabla \times (B_{b,\theta} \mathbf{i}_\theta) - \mu_0 (\mathbf{J}_b - J_{b,\theta} \mathbf{i}_\theta)\} = \mathbf{0}, \mathbf{n} \times \{\nabla \times (G_{b,\theta} \mathbf{i}_\theta)\} = \mathbf{0}$
- (ii) $\frac{\partial \phi_b}{\partial t} = 0, \frac{\partial A_{b,\theta}}{\partial t} = 0, \frac{\partial B_{b,\theta}}{\partial t} = 0, \frac{\partial G_{b,\theta}}{\partial t} = 0$
- (iii) $\frac{\partial \phi_b}{\partial z} = 0, \frac{\partial A_{b,\theta}}{\partial z} + \frac{1}{c} \frac{\partial A_{b,\theta}}{\partial t} = 0, \frac{\partial B_{b,\theta}}{\partial z} + \frac{1}{c} \frac{\partial B_{b,\theta}}{\partial t} = 0, \frac{\partial G_{b,\theta}}{\partial z} + c B_{b,\theta} = 0$



(b) Time-dependent fields (KUBLAI).

Figure 2.6. Boundary conditions for the beam-induced fields.

On the drift-tube wall at the grounded potential, the following conditions,

$$\phi_b = 0, \quad (2.27.a)$$

$$\frac{\partial A_{b,\theta}}{\partial t} = 0, \quad (2.27.b)$$

$$\mathbf{n} \times \{\nabla \times (G_{b,\theta} \mathbf{i}_\theta)\} = \mathbf{0}, \quad (2.27.c)$$

$$\mathbf{n} \times \{\nabla \times (B_{b,\theta} \mathbf{i}_\theta) - \mu_0 (\mathbf{J}_b - J_{b,\theta} \mathbf{i}_\theta)\} = \mathbf{0}, \quad (2.27.d)$$

are applied, which give the conditions,

$$\mathbf{n} \times \mathbf{E}_b = \mathbf{0}, \quad (2.28.a)$$

$$\mathbf{n} \cdot \frac{\partial \mathbf{B}_b}{\partial t} = 0. \quad (2.28.b)$$

On the beam-exit boundary, i.e. the entrance of the collector, although strictly no condition can be applied, the following conditions are approximately applied in the KUBLAI,

$$\frac{\partial \phi_b}{\partial z} = 0, \quad (2.29.a)$$

$$\frac{\partial A_{b,\theta}}{\partial z} + \frac{1}{c} \frac{\partial A_{b,\theta}}{\partial t} = 0, \quad (2.29.b)$$

$$\frac{\partial B_{b,\theta}}{\partial z} + \frac{1}{c} \frac{\partial B_{b,\theta}}{\partial t} = 0, \quad (2.29.c)$$

$$\frac{\partial G_{b,\theta}}{\partial z} + c B_{b,\theta} = 0. \quad (2.29.d)$$

Equations (2.29.b), (2.29.c) and (2.29.d) mean that the TE and TM waves in

terms of $A_{b,\theta}$, $B_{b,\theta}$ and $G_{b,\theta}$ propagate through the boundary with the light velocity without any variation. Also, [Eq. \(2.29.a\)](#) means that the irrotational electric field is perpendicular to the symmetry axis.

For the static field calculations in the KUAD2, the fields are given in terms of ϕ_b , $A_{b,\theta}$ and $B_{b,\theta}$ as follows,

$$\nabla^2 \phi_b = -\frac{\rho_b}{\varepsilon_0}, \quad (2.30.a)$$

$$\nabla \times \nabla \times (A_{b,\theta} \mathbf{i}_\theta) = \mu_0 J_{b,\theta} \mathbf{i}_\theta, \quad (2.30.b)$$

$$\nabla \times (B_{b,\theta} \mathbf{i}_\theta) = \mu_0 (\mathbf{J}_b - J_{b,\theta} \mathbf{i}_\theta), \quad (2.30.c)$$

while $G_{b,\theta} \equiv 0$ because of $\partial/\partial t \equiv 0$ in [Eq. \(2.26.d\)](#).

Although, in general, for the low beam current, the z - and r -components of the magnetic field may be well negligible compared with the external focusing field, and therefore are not calculated in the existing code KUAD [\[24\]](#), the improved KUAD2 code, on the other hand, calculates them in terms of $A_{b,\theta}$ in order to provide the initial condition for the KUBLAI simulation.

The boundary conditions in the KUAD2 are summarized in [Fig. 2.6\(a\)](#). For ϕ_b , the specific voltages are given, respectively, to the boundary conditions on the cathode at a negative potential and the drift-tube wall at the grounded potential. No boundary condition is required for $A_{b,\theta}$ by use of the technique used in the KUSOS as will be described in [chapter 4](#). And also for $B_{b,\theta}$, no boundary condition is needed.

2.2.4. Electron Dynamics

Either the KUBLAI or the KUAD2 simulates the motions of the ring particles (see Fig. 2.2). From the positions (z_ν, r_ν) , and velocities $(u_{\nu,z}, u_{\nu,r}, u_{\nu,\theta})$ of the ring particles give, as follows, the charge density ρ_b , and the current density \mathbf{J}_b of the electron beam,

$$\rho_b = \sum_\nu \frac{q_\nu}{2\pi r_\nu} \delta(z - z_\nu, r - r_\nu), \quad (2.31.a)$$

$$\mathbf{J}_b = \sum_\nu \frac{q_\nu}{2\pi r_\nu} \mathbf{u}_\nu \delta(z - z_\nu, r - r_\nu), \quad (2.31.b)$$

where ν denotes the particle number, q_ν the charge of the ν -th ring particle, and δ is the 2-dimensional Dirac's delta function.

In this subsection, the basic equations of the ring particle motion are presented.

The relativistic equation of motion for an electron with velocity $\mathbf{u}_\nu = (u_{\nu,z}, u_{\nu,r}, u_{\nu,\theta})$ is described by,

$$\frac{d(m_0 \gamma_\nu \mathbf{u}_\nu)}{dt} = -e \{ \mathbf{E}(z_\nu, r_\nu, t) + \mathbf{u}_\nu \times \mathbf{B}(z_\nu, r_\nu, t) \}, \quad (2.32)$$

where m_0 and e denote, respectively, the electron rest mass and charge, and γ_ν denotes the Lorentz factor defined by,

$$\gamma_\nu = \left(1 - \frac{|\mathbf{u}_\nu|^2}{c^2} \right)^{-1/2}. \quad (2.33)$$

With

$$m_0 c^2 \frac{d\gamma_v}{dt} = \frac{dK_v}{dt} = -e\mathbf{E} \cdot \mathbf{u}_v, \quad (2.34)$$

where K_v is the kinetic energy, Eq. (2.32) is reduced to,

$$\frac{d\mathbf{u}_v}{dt} = -\frac{e}{m_0 \gamma_v} \left(\mathbf{E} + \mathbf{u}_v \times \mathbf{B} - \frac{\mathbf{E} \cdot \mathbf{u}_v}{c^2} \mathbf{u}_v \right), \quad (2.35)$$

or, in components,

$$\frac{du_{v,z}}{dt} = -\frac{e}{m_0 \gamma_v} \left(E_z + u_{v,r} B_\theta - u_{v,\theta} B_r - \frac{\mathbf{E} \cdot \mathbf{u}_v}{c^2} u_{v,z} \right), \quad (2.36.a)$$

$$\frac{du_{v,r}}{dt} = -\frac{e}{m_0 \gamma_v} \left(E_r + u_{v,\theta} B_z - u_{v,z} B_\theta - \frac{\mathbf{E} \cdot \mathbf{u}_v}{c^2} u_{v,r} \right) + \frac{u_{v,\theta}^2}{r_v}, \quad (2.36.b)$$

$$\frac{du_{v,\theta}}{dt} = -\frac{e}{m_0 \gamma_v} \left(E_\theta + u_{v,z} B_r - u_{v,r} B_z - \frac{\mathbf{E} \cdot \mathbf{u}_v}{c^2} u_{v,\theta} \right) - \frac{u_{v,\theta} u_{v,r}}{r_v}. \quad (2.36.c)$$

On the assumption of cylindrical symmetry, the canonical angular momentum $P_{v,\theta}$ is conserved as

$$P_{v,\theta} = r_v (m_0 \gamma_v u_{v,\theta} - e A_\theta), \quad (2.37)$$

where

$$A_\theta = A_{b,\theta} + A_{f,\theta}, \quad (2.38)$$

It is to be noted that Eq. (2.37) is equivalent to Eq. (2.36.c), where Eq. (2.36.c) is derived by differentiating Eq. (2.37) with respect to time t , and thus Eq.(2.37) is used in the KUBLAI instead.

In the static fields in the KUAD2, in addition to $P_{v,\theta}$, the sum W_v of the electron kinetic energy and the electric potential energy is also conserved,

$$W_v = m_0 c^2 (\gamma_v - 1) - e\phi_b, \quad (2.39)$$

which is found equivalent to the equation $\{u_{v,z} \times (2.36.a) + u_{v,r} \times (2.36.b)\}$.

Since γ_v and $u_{v,\theta}$ can be calculated from Eqs. (2.37) and (2.39), the term $(u_{v,z}^2 + u_{v,r}^2)$ is given by the potentials ϕ_b and A_θ at the position (z_v, r_v) . When the velocity $(u_{v,z}, u_{v,r})$ makes the angle α_v with respect to the z -axis, velocity components are expressed by,

$$u_{v,z} = \sqrt{u_{v,z}^2 + u_{v,r}^2} \cos \alpha_v, \quad (2.40.a)$$

$$u_{v,r} = \sqrt{u_{v,z}^2 + u_{v,r}^2} \sin \alpha_v, \quad (2.40.b)$$

and the following equation for the angle α_v is derived from either Eq. (2.36.a) or (2.36.b).

$$\frac{d\alpha_v}{dt} = \frac{eB_\theta}{m_0\gamma_v} + \frac{1}{2\gamma_v^2(u_{v,z}^2 + u_{v,r}^2)} \left[\frac{\partial \{ \gamma_v^2 (u_{v,z}^2 + u_{v,r}^2) \}}{\partial r} u_{v,z} - \frac{\partial \{ \gamma_v^2 (u_{v,z}^2 + u_{v,r}^2) \}}{\partial z} u_{v,r} \right], \quad (2.41)$$

where the term $\gamma_v^2(u_{v,z}^2 + u_{v,r}^2)$ is given, as follows, by the conserved values $P_{v,\theta}$ and W_v , and the potentials ϕ_b and A_θ at the position (z_v, r_v) .

$$\gamma_v^2(u_{v,z}^2 + u_{v,r}^2) = \left(\frac{W_v + m_0 c^2 + e\phi_b}{m_0 c} \right)^2 - \left(\frac{P_{v,\theta} + e r_v A_\theta}{m_0 r_v} \right)^2 - c^2. \quad (2.42)$$

Chapter 3

Development of an Improved Finite Element Code for Cylindrically Symmetric Eigenmodes

Discussed in [this chapter](#) is development of an efficient eigenmode solver KUEMS (acronym for Kyoto University EigenMode Solver), suitable for calculating fundamental modes in cylindrically symmetric cavities for the application to the klystron simulations.

3.1. Introduction

Cylindrically symmetric cavities are utilized in many RF devices, such as klystrons, RF-guns and various accelerating structures in particle accelerators. Many computer codes [7-14] have been developed so far, and are in use for RF cavity designing in decades. They can evaluate reasonably well electromagnetic fields, and cavity parameters such as resonance frequency, the quality factor, and the shunt impedance, which consequently enables cavity design with least cold testing.

For cylindrically symmetric standing-wave modes in klystrons, RF-guns, and so on, probably the most preferentially used code would be the

SUPERFISH [8], which calculates eigenfrequencies and corresponding angular magnetic fields H_θ at the mesh points using the Finite Differential method (FDM) with triangular meshes. However, depending on the cavity geometry, it is sometimes not accurate enough, or, in other words, takes too much CPU time as well as many computer memories to achieve required accuracy. Since both higher accuracy and less computational efforts are always important from the viewpoint of saving time and effort for the users, continuous improvements to greater extent are called for, for specific problems as of the present study.

From this viewpoint, a new two-dimensional code KUEMS has been developed, which is aimed at improved calculations of cylindrically symmetric TM_{0nm} modes applicable to the klystron simulations. The KUEMS uses,

- (i) instead of H_θ or rH_θ preferentially used in the existing codes [7-9,12], the quantity H_θ/r to describe the electromagnetic fields, which has the advantage of not requiring any special treatment on the symmetry axis,
- (ii) the Finite Element method (FEM) with quadratic triangular elements, which has high capability to model arbitrary structures.

Described in [this chapter](#) are the numerical methods used in the KUEMS, followed by comparisons of the numerical results among the three different formulations, i.e. with H_θ/r , H_θ and rH_θ , to show the advantageous features of the new formulation with H_θ/r with respect to the accuracy in the eigenfrequencies and the electric fields on the symmetry axis. Comparisons between the linear and the quadratic elements are also made to examine the accuracy, and also with the SUPERFISH.

3.2. Numerical Methods

Described in [this section](#) are the numerical methods used in the KUEMS, including the new Finite Element (FE) formulation with the quantity H_θ/r . The essential difference from the other formulations using H_θ and rH_θ as variables is to be described in [subsection 3.2.2](#).

3.2.1. Weak Formulation

As described in [subsection 2.2.1](#), the eigenfrequencies f_a ($= \omega_a/2\pi = ck_a/2\pi$), and eigenmodes \mathbf{E}_a , and \mathbf{H}_a are described by,

$$\nabla \times \mathbf{E}_a = k_a \mathbf{H}_a \quad \text{in } \Omega, \quad (3.1.a)$$

$$\nabla \times \mathbf{H}_a = k_a \mathbf{E}_a \quad \text{in } \Omega, \quad (3.1.b)$$

$$\nabla \cdot \mathbf{E}_a = 0 \quad \text{in } \Omega, \quad (3.1.c)$$

$$\nabla \cdot \mathbf{H}_a = 0 \quad \text{in } \Omega, \quad (3.1.d)$$

$$\mathbf{n} \times \mathbf{E}_a = \mathbf{0} \quad \text{on } \Gamma, \quad (3.1.e)$$

$$\mathbf{n} \cdot \mathbf{H}_a = 0 \quad \text{on } \Gamma, \quad (3.1.f)$$

where the boundary Γ and the domain Ω denote, respectively, the inner surface of the cavity wall and its volume, and \mathbf{n} denotes the unit vector normal to the boundary Γ . The frequency and the magnetic field are, thus, reduced to the following eigenvalue problem,

$$\nabla \times \nabla \times \mathbf{H}_a = k_a^2 \mathbf{H}_a \quad \text{in } \Omega, \quad (3.2.a)$$

$$\nabla \cdot \mathbf{H}_a = 0 \quad \text{in } \Omega, \quad (3.2.b)$$

$$\mathbf{n} \times (\nabla \times \mathbf{H}_a) = \mathbf{0} \quad \text{on } \Gamma, \quad (3.2.c)$$

$$\mathbf{n} \cdot \mathbf{H}_a = 0 \quad \text{on } \Gamma, \quad (3.2.d)$$

and the corresponding electric field is calculated by,

$$\mathbf{E}_a = \frac{1}{k_a} \nabla \times \mathbf{H}_a. \quad (3.3)$$

Since cylindrically symmetric TM_{0nm} modes ($H_{0nm,z} = H_{0nm,r} = E_{0nm,\theta} = 0$, $\partial/\partial\theta \equiv 0$. See [Fig. 3.1](#), for example.) automatically satisfy [Eqs. \(3.2.b\)](#), [and \(3.2.d\)](#), they can be described only by [Eqs. \(3.2.a\) and \(3.2.c\)](#), and it is equivalent to the following formulation,

$$\begin{aligned} \int_{\Omega} \mathbf{v} \cdot \{k_{0nm}^2 \mathbf{H}_{0nm} - \nabla \times (\nabla \times \mathbf{H}_{0nm})\} dV \\ + \int_{\Gamma} \mathbf{v} \cdot \{\mathbf{n} \times (\nabla \times \mathbf{H}_{0nm})\} dS = 0, \quad \text{for any test vector } \mathbf{v}, \end{aligned} \quad (3.4)$$

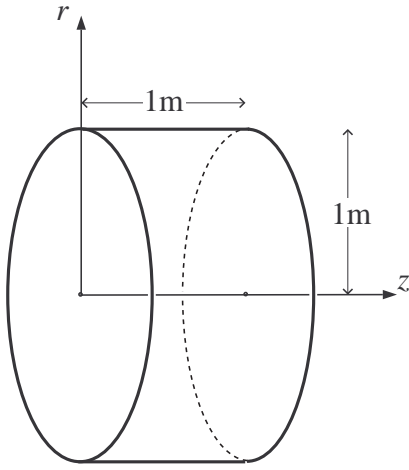
where dV and dS are, respectively, a volume element in Ω , and a surface element on Γ . With Gauss' divergence theorem, [Eq. \(3.4\)](#) can be further reduced to the following well-known weak formulation [\[13\]](#),

$$\int_{\Omega} (\nabla \times \mathbf{v}) \cdot (\nabla \times \mathbf{H}_{0nm}) dV = k_{0nm}^2 \int_{\Omega} \mathbf{v} \cdot \mathbf{H}_{0nm} dV, \quad \text{for any } \mathbf{v}, \quad (3.5)$$

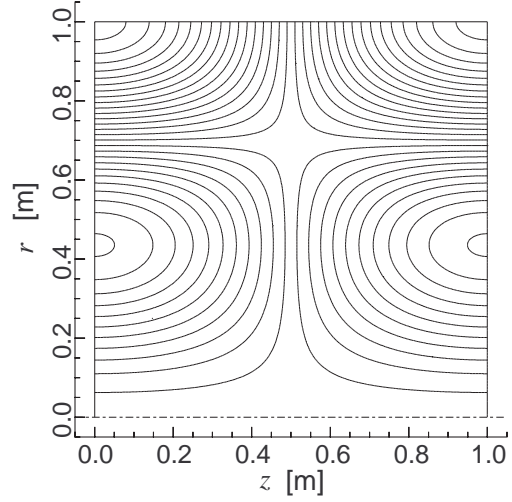
or, in components,

$$\begin{aligned} \int_{\Sigma} \left\{ \frac{\partial v_{\theta}}{\partial z} \frac{\partial H_{0nm,\theta}}{\partial z} + \frac{1}{r^2} \frac{\partial(rv_{\theta})}{\partial r} \frac{\partial(rH_{0nm,\theta})}{\partial r} \right\} 2\pi r dS \\ = k_{0nm}^2 \int_{\Sigma} v_{\theta} H_{0nm,\theta} 2\pi r dS, \quad \text{for any } v_{\theta}, \end{aligned} \quad (3.6)$$

where Σ is the cross section of the domain Ω on the z - r plane.



(a) Geometric shape of the test cavity.



(b) Typical eigenmode pattern (TM_{021} mode, contour lines with $rH_{\theta} = \text{constant}$).

Figure 3.1. Test cavity for comparisons with analytical solutions.

3.2.2. Choice of the Independent Variable

In the KUEMS, the quantity $H_{0nm,\theta}/r$ is chosen as the independent variable instead of $H_{0nm,\theta}$ or $rH_{0nm,\theta}$ preferentially used in the existing codes, exclusively due to the fact that no special treatment of the symmetry axis ($r = 0$) is required to be shown as follows.

With $\zeta = H_{0nm,\theta}/r$ and $u = v_{\theta}/r$, Eq. (3.6) can be expressed by,

$$\int_{\Sigma} \left\{ r^3 \left(\frac{\partial u}{\partial z} \frac{\partial \zeta}{\partial z} + \frac{\partial u}{\partial r} \frac{\partial \zeta}{\partial r} \right) + 2r^2 \left(u \frac{\partial \zeta}{\partial r} + \frac{\partial u}{\partial r} \zeta \right) + 4ru\zeta \right\} dS$$

$$= k_{0nm}^2 \int_{\Sigma} r^3 u \zeta dS, \quad \text{for any } u, \quad (3.7.a)$$

(this will be called ‘H/r-formulation’ hereafter). In contrast, choice of $h = H_{0nm,\theta}$, $v = v_{\theta}$ (‘H-formulation’), and choice of $\xi = rH_{0nm,\theta}$, $w = rv_{\theta}$ (‘rH-formulation’) lead to the following weak formulations, respectively,

$$\int_{\Sigma} \left\{ r \left(\frac{\partial v}{\partial z} \frac{\partial h}{\partial z} + \frac{\partial v}{\partial r} \frac{\partial h}{\partial r} \right) + \left(v \frac{\partial h}{\partial r} + \frac{\partial v}{\partial r} h \right) + \frac{vh}{r} \right\} dS = k_{0nm}^2 \int_{\Sigma} rvh dS, \quad \text{for any } v, \quad (3.7.b)$$

$$\int_{\Sigma} \frac{1}{r} \left(\frac{\partial w}{\partial z} \frac{\partial \xi}{\partial z} + \frac{\partial w}{\partial r} \frac{\partial \xi}{\partial r} \right) dS = k_{0nm}^2 \int_{\Sigma} \frac{w\xi}{r} dS, \quad \text{for any } w, \quad (3.7.c)$$

It is clearly seen that, for the integration of Eq. (3.7.b) with the term vh/r on the left, $h=0$ is always required on the axis ($r=0$) to avoid infinity, and also, for Eq. (3.7.c), $\nabla \xi = \mathbf{0}$ is always required on the axis in addition, both of which are consequently equivalent to the cylindrically symmetric conditions $H_{0nm,\theta} = E_{0nm,r} = 0$, and the existence of finite $E_{0nm,z}$ on the axis.

In the present ‘H/r-formulation’, on the other hand, these requirements are automatically satisfied so long as ζ and $\nabla \zeta$ remain finite, since $H_{0nm,\theta}$, $E_{0nm,z}$ and $E_{0nm,r}$ are all given in terms of ζ by,

$$H_{0nm,\theta} = r\zeta, \quad k_{0nm} E_{0nm,z} = 2\zeta + r \frac{\partial \zeta}{\partial r}, \quad k_{0nm} E_{0nm,r} = -r \frac{\partial \zeta}{\partial z}. \quad (3.8.a)$$

In contrast, the fields in the other formulations are given by,

$$H_{0nm,\theta} = h, \quad k_{0nm} E_{0nm,z} = \frac{h}{r} + \frac{\partial h}{\partial r}, \quad k_{0nm} E_{0nm,r} = -\frac{\partial h}{\partial z}, \quad (3.8.b)$$

$$H_{0nm,\theta} = \frac{\xi}{r}, \quad k_{0nm} E_{0nm,z} = \frac{1}{r} \frac{\partial \xi}{\partial r}, \quad k_{0nm} E_{0nm,r} = -\frac{1}{r} \frac{\partial \xi}{\partial z}. \quad (3.8.c)$$

The ‘H/r-formulation’ is, thus, shown not to require any specific conditions on the symmetry axis as the symmetry axis is actually not the ‘boundary’, and, with further following additional reasons, it is applied to the KUEMS,

- (i) analytical integration of [Eq.\(3.7.a\)](#) is easily carried out in the FE formulation described in [the following subsection](#), while, for the other formulations, special treatments are required on the symmetry axis,
- (ii) the ‘H/r-formulation’ is expected to result in higher accuracy in the fundamental TM_{010} modes, since $H_{010,\theta}/r \approx \text{constant}$ near the symmetry axis,
- (iii) the ‘H/r-formulation’ is found to result in smoother convergence in calculating the electric field on the axis, as will be shown in [subsection 3.3.1](#).

3.2.3. Finite Element Formulation

To solve numerically the weak formulation of [Eq. \(3.7.a\)](#), an N -dimensional subspace is applied to both the unknown function ζ , and the test function u . Suppose ζ is a linear combination of N basis functions $\{w_i\}$, and an infinite number of test functions u can be reduced to N test functions. Then, with the expression,

$$\zeta(z, r) = \sum_{j=1}^N x_{0nm,j} w_j(z, r), \quad (3.9.a)$$

$$u(z, r) = w_i(z, r), \quad (3.9.b)$$

the weak formulation of Eq. (3.7.a) can be reduced to a Galerkin formulation,

$$\sum_{j=1}^N a_{ij} x_{0nm,j} = k_{0nm}^2 \sum_{j=1}^N b_{ij} x_{0nm,j}, \quad \text{for any } 1 \leq i \leq N, \quad (3.10)$$

or, simply to an algebraic eigenvalue problem,

$$\mathbf{A} \mathbf{x}_{0nm} = k_{0nm}^2 \mathbf{B} \mathbf{x}_{0nm}, \quad (3.11)$$

where,

$$a_{ij} = 2\pi \int_{\Sigma} \left\{ r^3 \left(\frac{\partial w_i}{\partial z} \frac{\partial w_j}{\partial z} + \frac{\partial w_i}{\partial r} \frac{\partial w_j}{\partial r} \right) + 2r^2 \left(w_i \frac{\partial w_j}{\partial r} + \frac{\partial w_i}{\partial r} w_j \right) + 4r w_i w_j \right\} dS, \quad (3.12.a)$$

$$b_{ij} = 2\pi \int_{\Sigma} r^3 w_i w_j dS. \quad (3.12.b)$$

The FE formulation is a Galerkin formulation above with a particular set of basis functions $\{w_i\}$. The domain Σ is divided into finite elements Σ_e with N nodes (Fig. 3.2, for example, shows 32 linear elements, and 8 quadratic elements with $N=25$ nodes), and the basis function w_i is defined as,

- (i) $w_i = 1$ at the node i ,
- (ii) $w_i = 0$ at the others,
- (iii) continuous in Σ ,
- (iv) piecewise smooth in Σ_e .

The KUEMS uses well-known Lagrange-type quadratic basis functions, which enables the analytical integration of Eqs. (3.12).

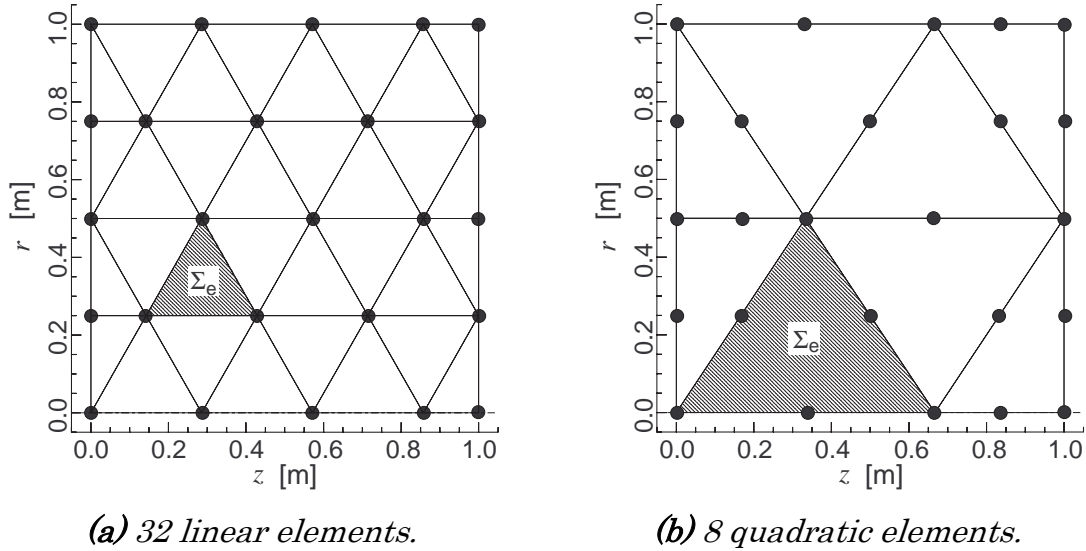


Figure 3.2. Mesh examples for the test cavity with $N = 25$ nodes.

3.2.4. Finding Eigenfrequencies

Although the KUEMS can find all eigenfrequencies at the expense of CPU time, limiting to the eigenfrequency closest to a given target frequency (i.e. the operating frequency of the klystron) $f = ck/2\pi$, it can quickly look for by use of the following numerical method based on the Power method, which finds the absolute maximum eigenvalue through iterative

calculations.

The algebraic eigenvalue problem expressed by Eq. (3.11) can be rewritten as,

$$\mathbf{C}\mathbf{x}_{0nm} = \lambda_{0nm}\mathbf{x}_{0nm}, \quad (3.13)$$

where,

$$\lambda_{0nm} = \frac{1}{k_{0nm}^2 - k^2}, \quad (3.14.a)$$

$$\mathbf{C} = (\mathbf{A} - k^2\mathbf{B})^{-1}\mathbf{B}. \quad (3.14.b)$$

The absolute maximum eigenvalue λ_{0nm} of the $N \times N$ matrix \mathbf{C} is found using the Power method, which proceeds the following simple iterative calculations, with an arbitrary initial vector $\mathbf{x}_{(0)}$ normalized as $x_{(0),i} = 1$, where i ($1 \leq i \leq N$) is an arbitrary number,

- (I) calculate $\mathbf{y}_{(n)} = \mathbf{C}\mathbf{x}_{(n)}$,
- (II) calculate $\mathbf{x}_{(n+1)} = \mathbf{y}_{(n)} / \lambda_{(n)}$, where $\lambda_{(n)} = y_{(n),i}$,
- (III) if $\mathbf{x}_{(n+1)} \neq \mathbf{x}_{(n)}$, go back to (I).

For the calculation of $\mathbf{y}_{(n)}$ at step (I), in order to save computer memory, the matrices \mathbf{B} and $(\mathbf{A} - k^2\mathbf{B})$ are stored instead of \mathbf{C} (note that \mathbf{C} is not sparse despite both \mathbf{B} and $(\mathbf{A} - k^2\mathbf{B})$ are quite sparse), and the Conjugate Gradient method is applied to the linear system

$(A - k^2 \mathbf{B})\mathbf{y}_{(n)} = \mathbf{B}\mathbf{x}_{(n)}$. Step (II) normalizes $\mathbf{x}_{(n+1)}$ as $x_{(n+1),i} = 1$.

As a consequence, the absolute maximum eigenvalue λ_{0nm} gives the eigenfrequency f_{0nm} with the least $|f_{0nm}^2 - f^2|$ by

$$f_{0nm} = \sqrt{f^2 + \frac{1}{\lambda_{0nm}} \left(\frac{2\pi}{c}\right)^2}. \quad (3.15)$$

3.3. Numerical Examinations

To verify the accuracy of the developed KUEMS, calculations were carried out for analytically solvable modes in a test cavity. The numerical error from the ideal (not measured) value is, in general, mainly attributed to the two errors:

- (i) the error due to inaccurate modeling of geometric shape with a finite number of elements,
- (ii) the discretization error of the formulation.

To restrict discussions here to the latter one, a pillbox, whose cross section on the $z-r$ plane has no curvature, is chosen as the test cavity (see [Fig. 3.1](#)).

In [subsection 3.3.3](#), however, the KUEMS is applied to a practical klystron cavity with curvatures.

3.3.1. Comparisons among Three Different Formulations

To verify the accuracy of the ‘H/r-formulation’ used in the KUEMS,

calculations were performed using three different formulations, namely the ‘H/r-’, ‘H-’ and ‘rH-formulation’, with the linear elements. The configuration used here is the pillbox of a 1 m radius, and a 1 m length shown in [Fig. 3.1](#).

[Figure 3.3](#) shows the relative errors of eigenfrequencies f_{0nm} (solid lines) and cavity voltages V_{0nm} (dashed lines) from the analytical accurate solutions (refer to [Table 3.1](#)), where the eigenmodes \mathbf{E}_{0nm} and \mathbf{H}_{0nm} are normalized as the stored energies $W_{0nm} = 1$ Joule, and V_{0nm} is defined by

$$V_{0nm} = \frac{1}{\sqrt{\epsilon_0}} \int_{r=0} |E_{0nm,z}| dz . \quad (3.16)$$

As for the frequencies f_{0nm} , it is found that, as was expected, the ‘H/r-formulation’ results in remarkably higher accuracy for the fundamental TM_{010} mode than the other ‘H-’ or ‘rH-formulation’, but in almost similar accuracy for higher modes. High accuracy for the fundamental mode is, however, quite desirable, since it is most commonly utilized in klystrons. This advantage results from the fact that $\zeta = H_{010,\theta}/r \approx \text{constant}$ for TM_{010} mode near the symmetry axis.

On the other hand, in the cavity voltages V_{0nm} , the ‘H/r-formulation’ seems to show less accuracy for some modes (TM_{020} mode in [Fig. 3.3\(c\)](#), for example). However, it is rather to be noted that the voltages calculated with the ‘H/r-formulation’ are found to converge smoothly as N increases, while those with the ‘H-’ and the ‘rH-formulation’ do not.

Smooth convergence is remarkably important, since rough convergence would make extrapolation difficult. This advantage also results from the fact that the quantity $\zeta = H_{0nm,\theta}/r$ used in the ‘H/r-formulation’ has higher degree of freedom around the axis, compared with the other

formulations by $h = H_{0nm,\theta}$ and $\xi = rH_{0nm,\theta}$, because no condition is applied to the axis in the ‘H/r-formulation’.

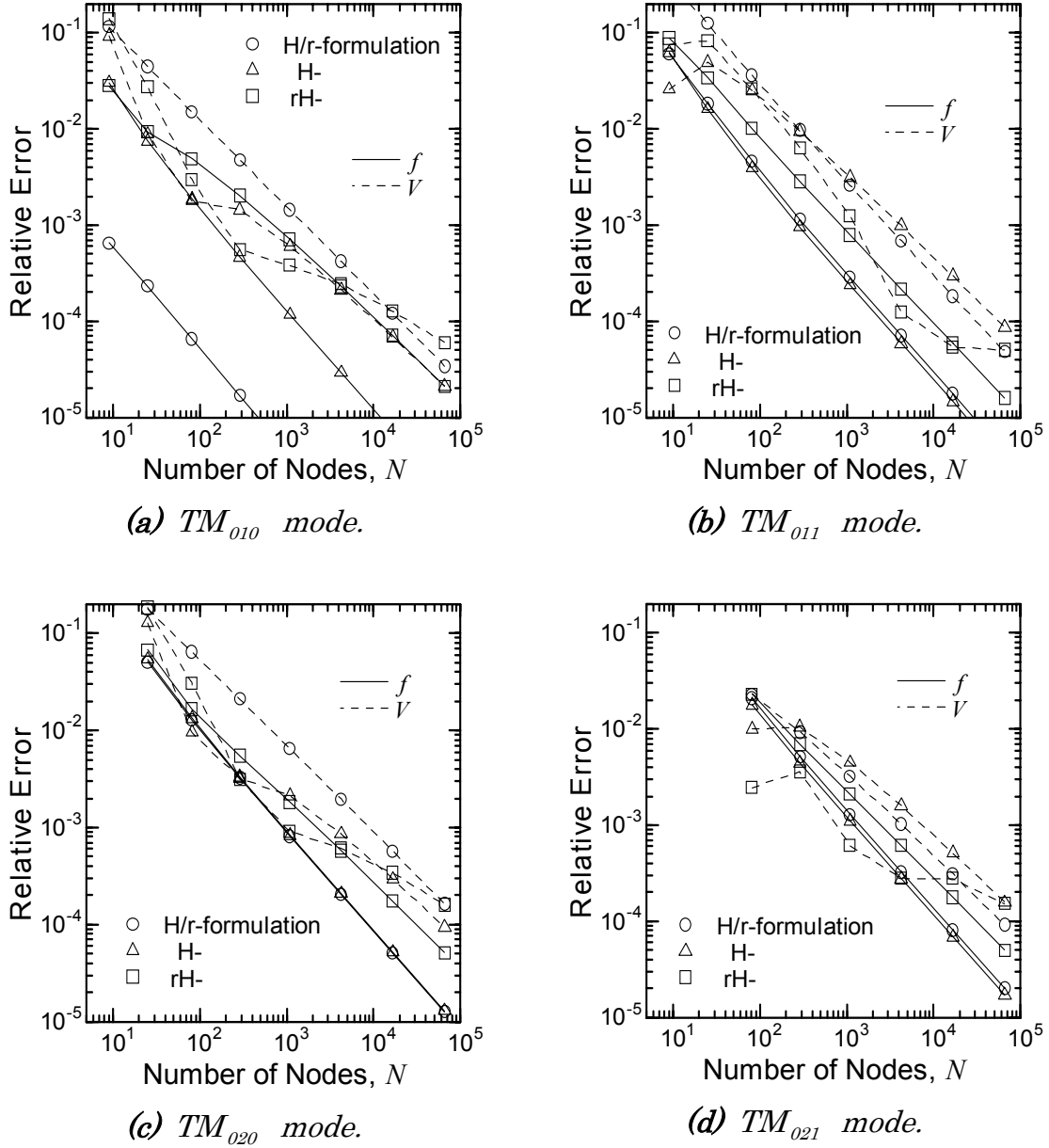


Figure 3.3. Relative errors in eigenfrequencies f_{0nm} , and cavity voltages V_{0nm} for the test cavity, comparing three different formulations.

Table 3.1. Analytical solutions of eigenfrequencies f_{0nm} and cavity voltages V_{0nm} of TM_{0nm} modes in a pillbox of a 1 m radius and a 1 m length.

	f_{0nm} [MHz]	V_{0nm} [kV]
TM ₀₁₀	114.7425278	516.5054777
TM ₀₁₁	188.7716270	282.6556994
TM ₀₂₀	263.3819797	788.0407287
TM ₀₂₁	303.0494130	616.6182798

3.3.2. Comparisons between Linear and Quadratic Elements

Since the quadratic elements are generally regarded to show higher accuracy than the linear elements for the same number of nodes, they were actually applied to some eigenmode solvers [9,11-13] as well as to the present KUEMS.

However, it is not obvious whether they may result in higher accuracy within the same CPU time, in which the users are very much interested. To make this clear, comparisons were made between the linear and the quadratic elements with the ‘H/r-formulation’ for the lowest three TM_{0nm} modes in the pillbox. For comparison, the SUPERFISH, which uses the FDM of the first order, is also applied to the same modes.

As shown in Fig. 3.4(a), the relative frequency errors $\Delta f_{0nm}/f_{0nm}$ are found to scale as $\Delta f_{0nm}/f_{0nm} \propto N^{-2.0 \sim -2.2}$ for the quadratic elements, while $\Delta f_{0nm}/f_{0nm} \propto N^{-1.0 \sim -1.1}$ for the linear elements, and the SUPERFISH. It is also important that, as shown in Fig. 3.4(b), the CPU time T is found also to

increase with the same order for either the linear or the quadratic elements, as N increases. The CPU time scales as $T \propto N^{1.7}$ for the linear and the quadratic elements, and $T \propto N^{1.8}$ for the SUPERFISH. Consequently, as shown in Fig. 3.5, the quadratic element scheme is found to take the least CPU time among the three for all the three modes.

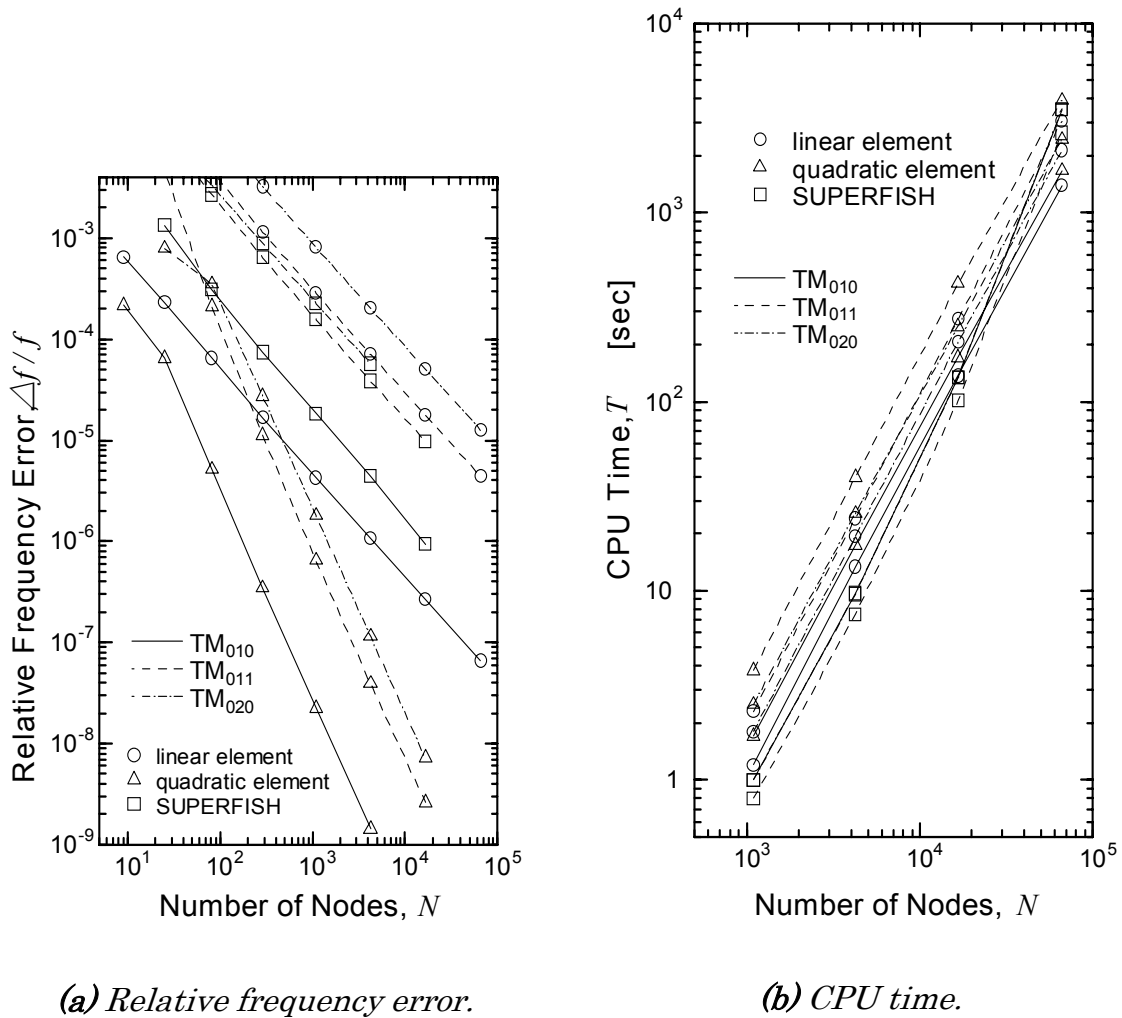


Figure 3.4. Relative frequency error $\Delta f_{0nm}/f_{0nm}$, and CPU time T as functions of number of nodes N , comparing linear element scheme, quadratic element scheme, and the SUPERFISH.

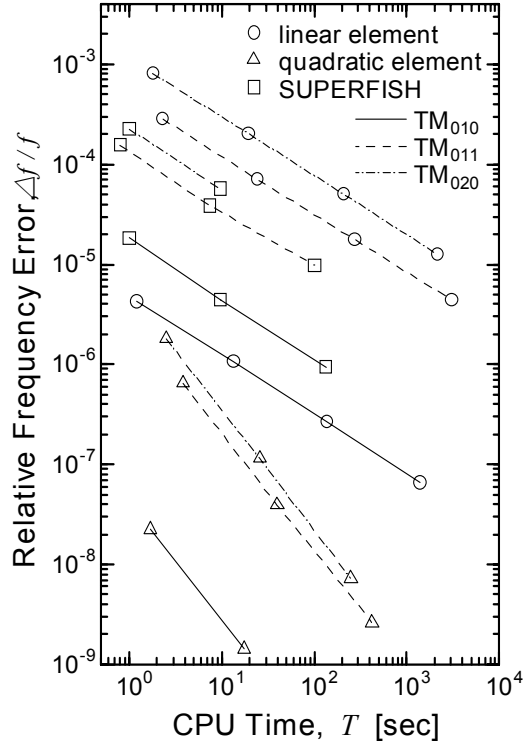


Figure 3.5. Relative frequency error $\Delta f_{0nm}/f_{0nm}$ as functions of CPU time T , comparing linear element scheme, quadratic element scheme and the SUPERFISH.

3.3.3. Application to a Klystron Cavity

The KUEMS was applied to a fundamental mode of a klystron cavity shown in Fig. 3.6. Considering the symmetry involved, the elements were placed in the region of $z \geq 0$, $r \geq 0$. The boundary on the right is located relatively far enough at $z = 60$ mm, and $E_z = 0$ is applied as the boundary condition. This approximation seems very reasonable, since a klystron is designed so that the cut-off frequency of the drift-tube should be much higher than the operating frequency.

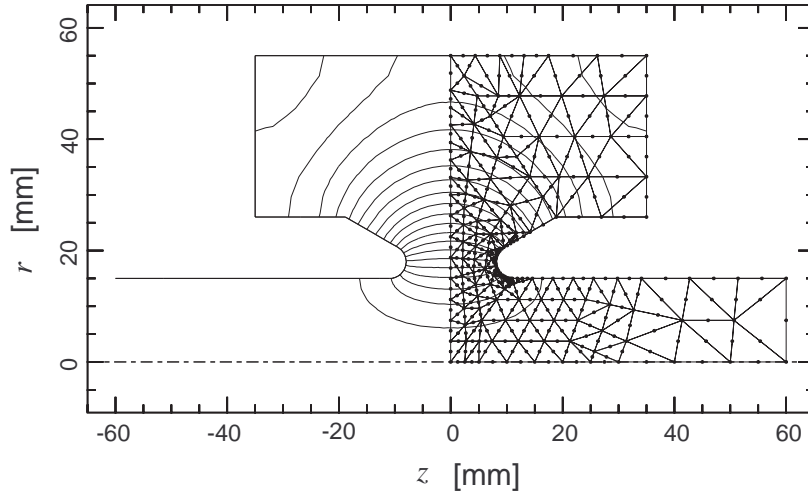


Figure 3.6. Meshes ($N = 503$) and a fundamental mode pattern in a klystron cavity.

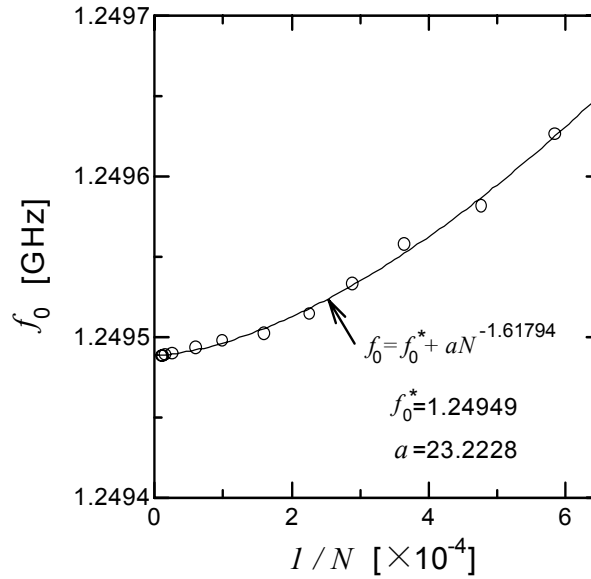


Figure 3.7. Calculated frequency of the fundamental mode f_0 as a function of number of nodes N .

In order to verify the solution convergence of the KUEMS, the number of nodes N was varied. **Figure 3.7** shows the calculated eigenfrequency f_0 of the fundamental mode, as a function of N . The results show smooth convergence of $N^{-1.6}$ order. The slower convergence

than the previous case of $\Delta f_{0nm}/f_{0nm} \propto N^{-2.0 \sim -2.2}$ for the pillbox is due to the modeling error of the cavity nose curvature.

In the application to the klystron simulation in [chapter 5 and 6](#), around 10,000 nodes are used, leading to less than 10^{-5} relative frequency error evaluated from the extrapolated value f_0^* .

3.4. Concluding Remarks

A new two-dimensional code KUEMS has been developed based on the FEM, making it ideal for calculating cylindrically symmetric eigenmodes.

The quantity $H_{0nm,\theta}/r$, which has the advantage of not requiring any conditions on the symmetry axis, is used to represent the electromagnetic fields, instead of $H_{0nm,\theta}$, or $rH_{0nm,\theta}$ used so far in the existing codes. It is found that the new FE formulation with $H_{0nm,\theta}/r$ results in remarkably higher accuracy in the eigenfrequency of the fundamental mode, but no less accuracy in the other higher modes. It also results in smoother convergence of the calculation of the electric field on the symmetry axis, with respect to number of the mesh points.

It is also found that, by use of the quadratic elements, faster convergence can be achieved compared with the linear elements or the SUPERFISH. The numerical error in the eigenfrequencies $\Delta f_{0nm}/f_{0nm}$ in terms of the CPU time T is found to scale as $\Delta f_{0nm}/f_{0nm} \propto T^{-1.2}$ for the quadratic elements, and $\Delta f_{0nm}/f_{0nm} \propto T^{-0.6}$ for the linear elements and the SUPERFISH.

All these results are remarkable and encouraging from the viewpoint of saving time and efforts for both the computers and the users.

Chapter 4

Development of a Finite-Element / Boundary-Integral Hybrid Code for Unbounded Magnetostatic Fields with Nonlinear Media

Presented in this chapter is a hybrid Finite Element (FE) code KUSOS (acronym for Kyoto University SOlenoidal field Solver), which has been developed in this study, and is to be used for calculating focusing magnetostatic fields in klystrons. The new formulation in the KUSOS gives a minimum for the energy functional in the infinite space, taking into account nonlinearity in media.

4.1. Introduction

The Finite Element method (FEM) is commonly used for calculations of electromagnetic fields. The FEM suffers, however, the disadvantage that only a finite number of elements can be used to discretise a given problem. In some situations, one can use the FEM for unbounded problems with an artificial boundary remote enough from the center of the problem. However,

this truncation does not guarantee solutions within any desired accuracy for many problems, such as magnetostatic fields, electromagnetic scattering, radiation from antennas, and so on, even though much computational efforts are made.

To deal with such unbounded problems, many methods based on the FEM have been developed so far. Many of them are listed in a previous review paper [26], and, since that time, many others have been developed mainly for electromagnetic scattering [27-35]. Representative methods are:

- (i) the infinite element technique which extends elements to the infinite space by use of decay functions as basis functions,
- (ii) the ballooning technique in which a single super element is constructed by merging successive concentric rings in an iterative manner,
- (iii) the iterative field-feedback methods for approximating the boundary condition on the fictitious boundary,
- (iv) the hybrid methods combining the FEM with integral equation methods, such as the Boundary Element method (BEM), the Moment method (MM), and the methods with eigenfunctions as basis functions.

Among these techniques, the hybrid FEMs yield accurate and reliable solutions that give minima for the energy functional in the infinite space. It is a well-known fact that the integral equation methods deal with unbounded problems very effectively, but cannot treat inhomogeneous, nor nonlinear media. The FEM, in contrast, can easily deal with inhomogeneous and nonlinear media. The hybrid FEMs retain the efficient characteristics of both methods by applying,

- (i) the FEM to the region inside the fictitious boundary within which all nonlinear media are placed,
- (ii) the integral equation methods to the exterior homogeneous region.

Presented in this chapter is a new FEM/MM-hybrid code KUSOS developed in this study for unbounded magnetostatic field problems with nonlinear media, having good features as follows;

- (i) the solution gives a minimum for the energy functional in the infinite space, as most of the hybrid methods do,
- (ii) the fictitious boundary can have an arbitrary shape,
- (iii) difficulties associated with singularity of Green's functions on the fictitious boundary are avoided,
- (iv) continuity of both tangential and normal fields on the boundary are fulfilled in an integral manner.

There is a previously presented FEM/MM-hybrid method for electromagnetic scattering [27] similar to the method presented here, but the latter has remarkable difference on the point (iii). Also, a technique similar to (iii) was presented in an FEM/BEM-hybrid method [36], while it does not fulfill the field continuity in an integral manner, but by a point-matching technique.

As a consequence of (iii) and (iv), the solutions by the new FEM/MM-hybrid method are expected to be well continuous and smooth on the fictitious boundaries.

4.2. Numerical Methods

4.2.1. Problem Description

Consider the situation shown in **Fig. 4.1**, with all source current densities \mathbf{J}_f and media ($\mu \neq \mu_0$) inside an arbitrary surface Γ (what is called a ‘picture frame’) of domain Ω_{in} , i.e. $\mu \equiv \mu_0$, and $\mathbf{J}_f \equiv \mathbf{0}$ in the exterior region Ω_{ex} . Then the basic equation for the vector potential, **Eq. (2.22.a)**, can be rewritten as follows,

$$\nabla \times \left(\frac{1}{\mu} \nabla \times \mathbf{A}_{f,\text{in}} \right) = \mathbf{J}_f \quad \text{in } \Omega_{\text{in}}, \quad (4.1.a)$$

$$\nabla \times \left(\frac{1}{\mu_0} \nabla \times \mathbf{A}_{f,\text{ex}} \right) = \mathbf{0} \quad \text{in } \Omega_{\text{ex}}, \quad (4.1.b)$$

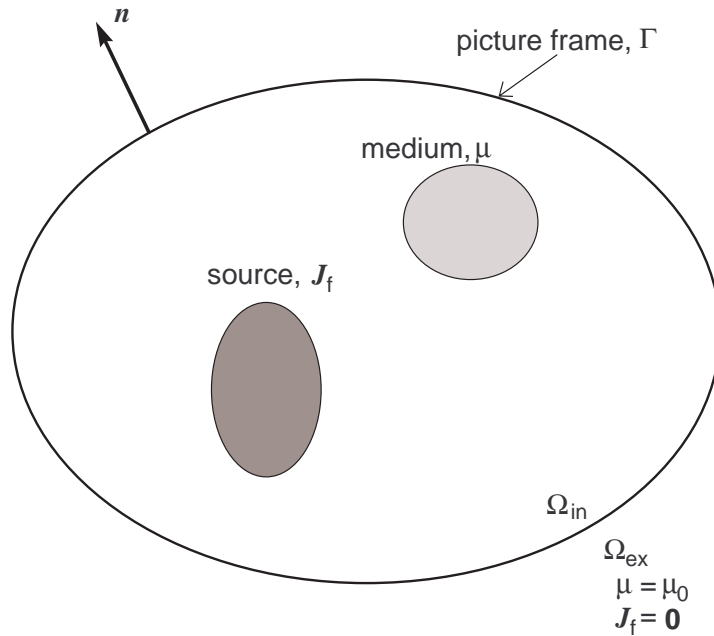


Figure 4.1. Problem description for the FEM/MM-hybrid method.

where $\mathbf{A}_{f,\text{in}}$, and $\mathbf{A}_{f,\text{ex}}$ denote, respectively, the vector potential inside, and outside the picture frame. To fulfill the field continuity on Γ , $\mathbf{A}_{f,\text{in}}$ and $\mathbf{A}_{f,\text{ex}}$ must satisfy, in addition,

$$\mathbf{n} \cdot (\nabla \times \mathbf{A}_{f,\text{in}}) = \mathbf{n} \cdot (\nabla \times \mathbf{A}_{f,\text{ex}}) \quad \text{on } \Gamma, \quad (4.1.c)$$

$$\mathbf{n} \times \left(\frac{1}{\mu} \nabla \times \mathbf{A}_{f,\text{in}} \right) = \mathbf{n} \times \left(\frac{1}{\mu_0} \nabla \times \mathbf{A}_{f,\text{ex}} \right) \quad \text{on } \Gamma. \quad (4.1.d)$$

4.2.2. Solution Subspace

Described in [this subsection](#) is choice of solution subspace, which characterizes the new FEM/MM-hybrid method used in the KUSOS.

Suppose $\mathbf{A}_{f,\text{in}}$, and $\mathbf{A}_{f,\text{ex}}$ are linear combinations of N basis functions $\{\mathbf{w}_{\text{in},i}\}$, and M functions $\{\mathbf{w}_{\text{ex},i}\}$ expressed by, respectively,

$$\mathbf{A}_{f,\text{in}}(z, r) = \sum_{i=1}^N x_i \mathbf{w}_{\text{in},i}(z, r), \quad (4.2.a)$$

$$\mathbf{A}_{f,\text{ex}}(z, r) = \sum_{i=1}^M y_i \mathbf{w}_{\text{ex},i}(z, r). \quad (4.2.b)$$

For the potential $\mathbf{A}_{f,\text{in}}$ within the picture frame, the same subspace is applied as in the KUEMS described in [chapter 3](#); the cross section of the domain Ω_{in} on the z - r plane is divided into finite elements with N nodes, and the Lagrange-type quadratic functions $\{w_i(z, r)\}$ are used as the N basis functions $\{\mathbf{w}_{\text{in},i} = r w_i \mathbf{i}_\theta\}$, where \mathbf{i}_θ is the unit vector in the

θ -direction.

For the exterior field $A_{i,\text{ex}}$, on the other hand, M numbers of Green's functions in free space are used as the basis functions,

$$\mathbf{w}_{\text{ex},i}(z, r) = \mathbf{i}_\theta \frac{r_i \mu_0}{2\pi} \int_0^\pi \frac{\cos \theta}{\sqrt{r^2 - 2rr_i \cos \theta + r_i^2 + (z - z_i)^2}} d\theta, \quad (4.3)$$

which satisfies,

$$\nabla \times \left(\frac{1}{\mu_0} \nabla \times \mathbf{w}_{\text{ex},i} \right) = \mathbf{i}_\theta \delta(z - z_i, r - r_i), \quad (4.4.a)$$

where, δ is Dirac's delta function. The M point sources (z_i, r_i) are located at the nodes within the sources \mathbf{J}_f , and those on the surfaces of the media (see Fig. 4.2). Because all the point sources (z_i, r_i) are located inside the picture frame Γ , the basis functions $\{\mathbf{w}_{\text{ex},i}\}$ satisfy,

$$\nabla \times \left(\frac{1}{\mu_0} \nabla \times \mathbf{w}_{\text{ex},i} \right) = \mathbf{0} \quad \text{in } \Omega_{\text{ex}} \cup \Gamma. \quad (4.4.b)$$

The condition $\nabla \times \nabla \times \mathbf{w}_{\text{ex},i} = \mathbf{0}$ on Γ , i.e. no point source on Γ , is essential for the field continuity in the present FEM/MM method, as will be described in the following subsection.

Thus, in addition to the potential values $A_{i,\text{in},\theta}/r$ on the nodes, equivalent point loop currents on the surface of the media are the unknown variables $\{y_i\}$, while a part of $\{y_i\}$ associated with the nodes within the

sources \mathbf{J}_f are known. Note that, because all point sources (z_i, r_i) are located inside the picture frame, the exterior field $\mathbf{A}_{f,ex}$ in terms of Eq. (4.2.b) satisfies Eq. (4.1.b) for any $\{y_i\}$.

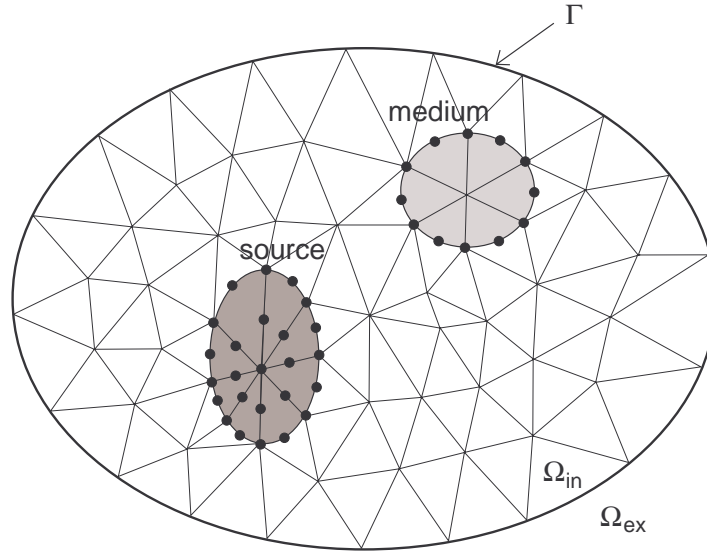


Figure 4.2. Distribution of the equivalent point sources in the FEM/MM-hybrid method.

4.2.3. Formulation

In [this subsection](#), the FEM/MM- hybrid formulation in the solution subspace is derived from [Eqs. \(4.1.a\), \(4.1.c\) and \(4.1.d\)](#), while [Eq. \(4.1.b\)](#) is always satisfied in the solution subspace, as described in [the previous subsection](#). The derivation here is based on the Garlarkin method, in order to show clearly how the continuities of both tangential and normal fields are preserved, although the same formulation can be obtained more easily from the energy functional in [subsection 4.2.4](#).

Satisfaction of both Eqs. (4.1.a) and (4.1.d) is equivalent to the following formulation,

$$\int_{\Omega_{\text{in}}} \mathbf{v} \cdot \left\{ \nabla \times \left(\frac{1}{\mu} \nabla \times \mathbf{A}_{\text{f, in}} \right) - \mathbf{J}_{\text{f}} \right\} dV + \int_{\Gamma} \mathbf{v} \cdot \left\{ \mathbf{n} \times \left(\frac{1}{\mu} \nabla \times \mathbf{A}_{\text{f, in}} - \frac{1}{\mu_0} \nabla \times \mathbf{A}_{\text{f, ex}} \right) \right\} dS = 0, \quad \text{for any test vector } \mathbf{v}, \quad (4.5)$$

where dV , and dS denote a volume element in Ω_{in} , and a surface element on Γ , respectively, and \mathbf{n} denotes the outward unit vector normal to Γ . With Gauss' divergence theorem, it can be reduced to the following weak formulation,

$$\int_{\Omega_{\text{in}}} \frac{1}{\mu} (\nabla \times \mathbf{v}) \cdot (\nabla \times \mathbf{A}_{\text{f, in}}) dV + \int_{\Gamma} \mathbf{v} \cdot \left\{ \mathbf{n} \times \left(\frac{1}{\mu_0} \nabla \times \mathbf{A}_{\text{f, ex}} \right) \right\} dS = \int_{\Omega_{\text{in}}} \mathbf{v} \cdot \mathbf{J}_{\text{f}} dV, \quad \text{for any } \mathbf{v}. \quad (4.6)$$

By applying the N -dimensional subspace $\{\mathbf{w}_{\text{in}, i}\}$ to both the unknown function $\mathbf{A}_{\text{f, in}}$ and the test vector \mathbf{v} , and M -dimensional subspace $\{\mathbf{w}_{\text{ex}, i}\}$ to $\mathbf{A}_{\text{f, ex}}$, the formulation becomes

$$\sum_{j=1}^N a_{ij} x_j + \sum_{j=1}^M b_{ij} y_j = f_i, \quad \text{for any } i \quad (1 \leq i \leq N), \quad (4.7)$$

or, an algebraic formulation,

$$\mathbf{Ax} + \mathbf{By} = \mathbf{f}, \quad (4.8)$$

where $\mathbf{A} \in \mathbb{R}^{N \times N}$, $\mathbf{B} \in \mathbb{R}^{N \times M}$, and $\mathbf{f} \in \mathbb{R}^N$ are given by,

$$a_{ij} = \int_{\Omega_{\text{in}}} \frac{1}{\mu} (\nabla \times \mathbf{w}_{\text{in},i}) \cdot (\nabla \times \mathbf{w}_{\text{in},j}) dV, \quad (4.9.a)$$

$$b_{ij} = \int_{\Gamma} \mathbf{w}_{\text{in},i} \cdot \left\{ \mathbf{n} \times \left(\frac{1}{\mu_0} \nabla \times \mathbf{w}_{\text{ex},j} \right) \right\} dS, \quad (4.9.b)$$

$$f_i = \int_{\Omega} \mathbf{w}_{\text{in},i} \cdot \mathbf{J}_f dV. \quad (4.9.c)$$

In the situation without a medium, the equivalent loop currents $\{y_i\}$ are all given by the sources \mathbf{J}_f . In that situation, the formulation of Eq. (4.8) becomes a basic FE formulation with the boundary condition (tangential magnetic field on Γ) given by the analytical solution for the sources \mathbf{J}_f described by the equivalent point sources. With media, on the other hand, in order to give the unknown equivalent currents $\{y_i\}$ on the media surfaces, additional formulation is required, which is derived from Eq. (4.1.c) as follows.

Equation (4.1.c) is equivalent to the following formulation,

$$\int_{\Gamma} u (\nabla \times \mathbf{A}_{f,\text{in}}) \cdot \mathbf{n} dS = \int_{\Gamma} u (\nabla \times \mathbf{A}_{f,\text{ex}}) \cdot \mathbf{n} dS, \quad \text{for any } u. \quad (4.10)$$

With Stokes' theorem, and $\mathbf{v} = -\nabla u$, it becomes

$$-\int_{\Gamma} \mathbf{v} \cdot (\mathbf{n} \times \mathbf{A}_{f,\text{in}}) dS = -\int_{\Gamma} \mathbf{v} \cdot (\mathbf{n} \times \mathbf{A}_{f,\text{ex}}) dS, \quad (4.11)$$

for any \mathbf{v} such that $\nabla \times \mathbf{v} = \mathbf{0}$.

By applying the subspace $\{\mathbf{w}_{\text{in},i}\}$, and $\{\mathbf{w}_{\text{ex},i}\}$ to $\mathbf{A}_{f,\text{in}}$, and $\mathbf{A}_{f,\text{ex}}$, respectively,

and the subspace $\{\nabla \times \mathbf{w}_{\text{ex},i}\}$ to the test vector \mathbf{v} such that $\nabla \times \mathbf{v} = \mathbf{0}$ (note that, from Eq. (4.4.b), $\nabla \times \nabla \times \mathbf{w}_{\text{ex},i} = \mathbf{0}$ on Γ), Eq. (4.11) is reduced to the following formulation,

$$\sum_{j=1}^N c_{ij} x_j = \sum_{j=1}^M d_{ij} y_j, \quad \text{for any } i \ (1 \leq i \leq M), \quad (4.12)$$

or, an algebraic formulation,

$$\mathbf{C}\mathbf{x} = \mathbf{D}\mathbf{y}, \quad (4.13)$$

where $\mathbf{C} \in \mathbb{R}^{M \times N}$, and $\mathbf{D} \in \mathbb{R}^{M \times M}$ are, respectively, given by,

$$c_{ij} = -\int_{\Gamma} \left(\frac{1}{\mu_0} \nabla \times \mathbf{w}_{\text{ex},i} \right) \cdot (\mathbf{n} \times \mathbf{w}_{\text{in},j}) dS, \quad (4.14.a)$$

$$d_{ij} = -\int_{\Gamma} \left(\frac{1}{\mu_0} \nabla \times \mathbf{w}_{\text{ex},i} \right) \cdot (\mathbf{n} \times \mathbf{w}_{\text{ex},j}) dS. \quad (4.14.b)$$

Because of $c_{ij} = b_{ji}$ from Eqs. (4.9.b) and (4.14.a), Eq. (4.13) can be rewritten as,

$$\mathbf{y} = \mathbf{D}^{-1} \mathbf{B}^T \mathbf{x}. \quad (4.15)$$

Substitution of Eq. (4.15) for \mathbf{y} into Eq. (4.8), then, yields

$$(\mathbf{A} + \mathbf{B}\mathbf{D}^{-1}\mathbf{B}^T)\mathbf{x} = \mathbf{f}. \quad (4.16)$$

By the above procedure, the hybrid formulation was derived, where

the solution \mathbf{x} gives not only the field within the picture frame, but also the exterior field from Eq. (4.15). It is convenient for saving computer memory that the matrix $(\mathbf{A} + \mathbf{B}\mathbf{D}^{-1}\mathbf{B}^T)$ is actually symmetric, since Eq. (4.14.b) becomes, with Gauss' divergence theorem and Eq. (4.4),

$$d_{ij} = \int_{\Omega_{\text{ex}}} \frac{1}{\mu_0} (\nabla \times \mathbf{w}_{\text{ex},i}) \cdot (\nabla \times \mathbf{w}_{\text{ex},j}) dV. \quad (4.17)$$

4.2.4. Energy Functional in the Infinite Space

As shown in the followings, the solution of Eq. (4.16) gives a minimum for the energy functional in the infinite space $\Omega_{\text{in}} \cup \Omega_{\text{ex}}$. This is a good feature of the hybrid method in the KUSOS, while this is not fulfilled by some existing methods for unbounded problems as well as by the basic BEM.

The energy functional $\varepsilon(\mathbf{x})$ is given by,

$$\varepsilon = \varepsilon_{\text{in}} + \varepsilon_{\text{ex}}, \quad (4.18.a)$$

$$\begin{aligned} \varepsilon_{\text{in}} &= \int_{\Omega_{\text{in}}} \left(\int H_{\text{f, in}} dB - \mathbf{A}_{\text{f}} \cdot \mathbf{J}_{\text{f}} \right) dV \\ &= \frac{1}{2} \int_{\Omega_{\text{in}}} \int \frac{1}{\mu} dB^2 dV - \int_{\Omega_{\text{in}}} \mathbf{A}_{\text{f, in}} \cdot \mathbf{J}_{\text{f}} dV, \end{aligned} \quad (4.18.b)$$

$$\begin{aligned} \varepsilon_{\text{ex}} &= \int_{\Omega_{\text{ex}}} \int H_{\text{f, ex}} dB dV \\ &= \frac{1}{2\mu_0} \int_{\Omega_{\text{ex}}} B_{\text{f, ex}}^2 dV. \end{aligned} \quad (4.18.c)$$

The energy functional takes a minimum at $\nabla\varepsilon = \mathbf{0}$. From Eq. (4.18.b), $\nabla\varepsilon_{\text{in}}$

is given as follows.

$$\begin{aligned}
\frac{\partial \varepsilon_{\text{in}}}{\partial x_i} &= \frac{1}{2} \int_{\Omega_{\text{in}}} \frac{\partial}{\partial x_i} \left(\int \frac{1}{\mu} dB^2 \right) dV - \frac{\partial}{\partial x_i} \left(\int_{\Omega_{\text{in}}} \mathbf{A}_{\text{f, in}} \cdot \mathbf{J}_{\text{f}} dV \right) \\
&= \frac{1}{2} \int_{\Omega_{\text{in}}} \frac{\partial B_{\text{f, in}}^2}{\partial x_i} \frac{d}{dB^2} \left(\int \frac{1}{\mu} dB^2 \right) dV - \frac{\partial}{\partial x_i} \left(\int_{\Omega_{\text{in}}} \mathbf{A}_{\text{f, in}} \cdot \mathbf{J}_{\text{f}} dV \right) \\
&= \frac{1}{2} \int_{\Omega_{\text{in}}} \frac{1}{\mu} \frac{\partial B_{\text{f, in}}^2}{\partial x_i} dV - \frac{\partial}{\partial x_i} \left(\int_{\Omega_{\text{in}}} \mathbf{A}_{\text{f, in}} \cdot \mathbf{J}_{\text{f}} dV \right) \\
&= \frac{1}{2} \int_{\Omega_{\text{in}}} \frac{1}{\mu} \frac{\partial}{\partial x_i} \left\{ \left(\sum_{j=1}^N x_j (\nabla \times \mathbf{w}_{\text{in}, j}) \right) \cdot \left(\sum_{k=1}^N x_k (\nabla \times \mathbf{w}_{\text{in}, k}) \right) \right\} dV \\
&\quad - \frac{\partial}{\partial x_i} \left\{ \int_{\Omega_{\text{in}}} \left(\sum_{j=1}^N x_j \mathbf{w}_{\text{in}, j} \right) \cdot \mathbf{J}_{\text{f}} dV \right\} \\
&= \int_{\Omega_{\text{in}}} \frac{1}{\mu} \sum_{j=1}^N x_j (\nabla \times \mathbf{w}_{\text{in}, j}) \cdot (\nabla \times \mathbf{w}_{\text{in}, j}) dV - \int_{\Omega_{\text{in}}} \mathbf{w}_{\text{in}, j} \cdot \mathbf{J}_{\text{f}} dV \\
&= \sum_{j=1}^N a_{ij} x_j - f_i. \tag{4.19}
\end{aligned}$$

Eq. (4.18.c), on the other hand, is reduced to, with Eqs. (4.2.b), (4.15) and (4.17),

$$\begin{aligned}
\varepsilon_{\text{ex}} &= \frac{1}{2\mu_0} \sum_{i=1}^M \sum_{j=1}^M y_i y_j \int_{\Omega_{\text{ex}}} (\nabla \times \mathbf{w}_{\text{ex}, i}) \cdot (\nabla \times \mathbf{w}_{\text{ex}, j}) dV \\
&= \frac{1}{2} \mathbf{y}^T \mathbf{D} \mathbf{y} \\
&= \frac{1}{2} \mathbf{x}^T \mathbf{B}^T \mathbf{D}^{-1} \mathbf{B} \mathbf{x}. \tag{4.20}
\end{aligned}$$

Then, from Eqs. (4.19) and (4.20), $\nabla \varepsilon$ is obtained as follows,

$$\nabla \varepsilon = \nabla \varepsilon_{\text{in}} + \nabla \varepsilon_{\text{ex}} = (\mathbf{A} \mathbf{x} - \mathbf{f}) + (\mathbf{B}^T \mathbf{D}^{-1} \mathbf{B} \mathbf{x}). \tag{4.21}$$

Thus the solution \mathbf{x} of Eq. (4.16) gives $\nabla\varepsilon=\mathbf{0}$ subject to the normal flux continuity condition of Eq. (4.15), and accordingly, gives a minimum for the energy functional ε .

4.2.5. Treatments of Nonlinear Media

In case of nonlinear media, the matrix \mathbf{A} in Eq. (4.16) depends on the solution \mathbf{x} . To deal with this nonlinearity, the KUSOS uses the Newton method, which is commonly used with the FEM for nonlinear problems [37].

With the initial vector $\mathbf{x}_{(0)}=\mathbf{0}$ and $\mathbf{r}_{(0)}=\mathbf{f}$,

- (I) calculate $\mathbf{x}_{(n+1)}=\mathbf{x}_{(n)}+\mathbf{H}^{-1}(\mathbf{x}_{(n)})\mathbf{r}_{(n)}$,
- (II) calculate $\mathbf{r}_{(n+1)}=\nabla\varepsilon(\mathbf{x}_{(n+1)})=\mathbf{f}-(\mathbf{A}(\mathbf{x}_{(n+1)})+\mathbf{B}^T\mathbf{D}^{-1}\mathbf{B})\mathbf{x}_{(n+1)}$,
- (III) unless $\mathbf{r}_{(n+1)}=\mathbf{0}$, go back to (I),

where $\mathbf{H}(\mathbf{x})$ is the Hessian matrix of the component $h_{ij}(\mathbf{x})$ of the energy functional $\varepsilon(\mathbf{x})$, i.e.,

$$\begin{aligned} h_{ij}(\mathbf{x}) &= \frac{\partial^2\varepsilon}{\partial x_i\partial x_j} \\ &= \frac{\partial}{\partial x_j} \sum_{k=1}^N (\mathbf{A} + \mathbf{B}^T\mathbf{D}^{-1}\mathbf{B})_{ik} x_k \\ &= (\mathbf{A} + \mathbf{B}^T\mathbf{D}^{-1}\mathbf{B})_{ij} + \sum_{k=1}^N \frac{\partial a_{ik}}{\partial x_j} x_k, \end{aligned} \tag{4.22.a}$$

$$\sum_{k=1}^N \frac{\partial a_{ik}}{\partial x_j} x_k = \sum_{k=1}^N \frac{\partial}{\partial x_j} \left\{ \int_{\Omega} \frac{1}{\mu} (\nabla \times \mathbf{w}_{in,i}) \cdot (\nabla \times \mathbf{w}_{in,k}) dV \right\} x_k$$

$$\begin{aligned}
&= \sum_{k=1}^N \left\{ \int_{\Omega} \frac{d}{dB^2} \left(\frac{1}{\mu} \right) (\nabla \times \mathbf{w}_{\text{in},i}) \cdot (\nabla \times \mathbf{w}_{\text{in},k}) \frac{\partial B^2}{\partial x_j} dV \right\} x_k \\
&= \sum_{k=1}^N \left[\int_{\Omega} \frac{d}{dB^2} \left(\frac{1}{\mu} \right) (\nabla \times \mathbf{w}_{\text{in},i}) \cdot (\nabla \times \mathbf{w}_{\text{in},k}) \right. \\
&\quad \left. \times \frac{\partial}{\partial x_j} \left\{ \sum_{j=1}^N \sum_{l=1}^N (\nabla \times \mathbf{w}_{\text{in},j}) \cdot (\nabla \times \mathbf{w}_{\text{in},l}) x_j x_l \right\} dV \right] x_k \\
&= \sum_{k=1}^N \sum_{l=1}^N \left\{ \int_{\Omega} \frac{d}{dB^2} \left(\frac{1}{\mu} \right) (\nabla \times \mathbf{w}_{\text{in},i}) \cdot (\nabla \times \mathbf{w}_{\text{in},k}) \right. \\
&\quad \left. \times \left\{ (\nabla \times \mathbf{w}_{\text{in},j}) \cdot (\nabla \times \mathbf{w}_{\text{in},l}) \right\} dV \right\} x_k x_l . \tag{4.22.b}
\end{aligned}$$

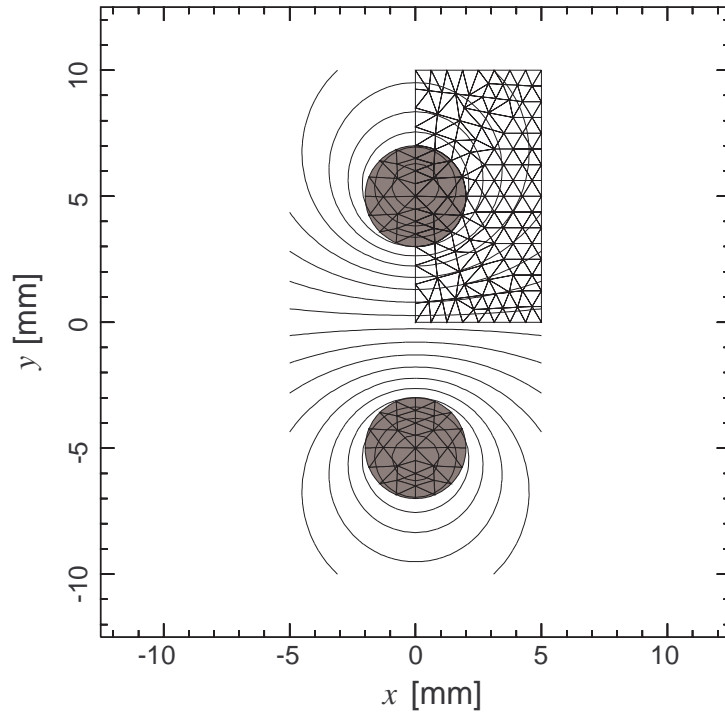
In each triangular element within nonlinear media, the volume integration is performed in a manner of Gauss' integration with 7 points [38], with μ and $d(1/\mu)/dB^2$ given as functions of B^2 .

4.3. Numerical Examinations

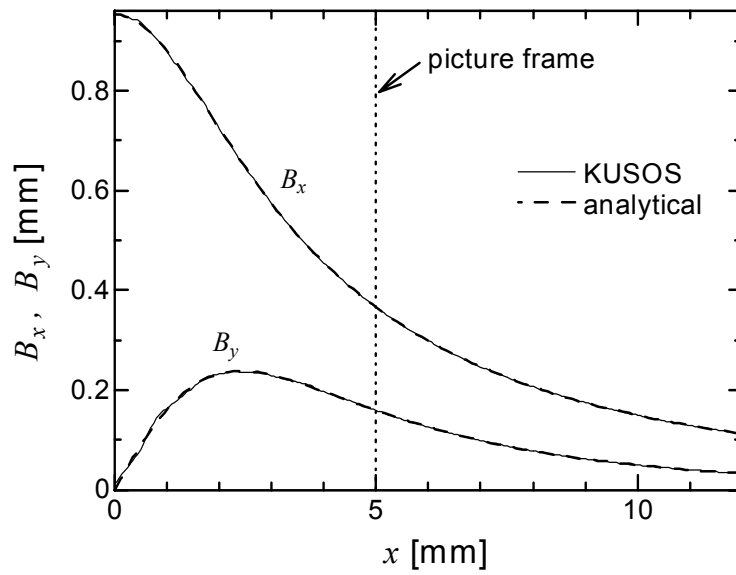
In [this section](#), numerical examinations for the verification of the KUSOS are presented.

Firstly, for comparison with analytical solutions, the KUSOS was applied to a simple situation shown in [Fig. 4.3\(a\)](#) with a pair of infinitely long conductors (no variation in the z -direction) with uniform current density in opposing directions. Considering the symmetries involved, finite elements are placed in the positive quadrant as shown in [Fig. 4.3\(a\)](#).

[Figure 4.3\(b\)](#) shows the calculated magnetic fields along $y = 2$ mm in the x -direction, together with the analytical solutions. The numerically calculated fields by the KUSOS are found to show good agreements with the analytical solutions, both inside and outside the picture frame.

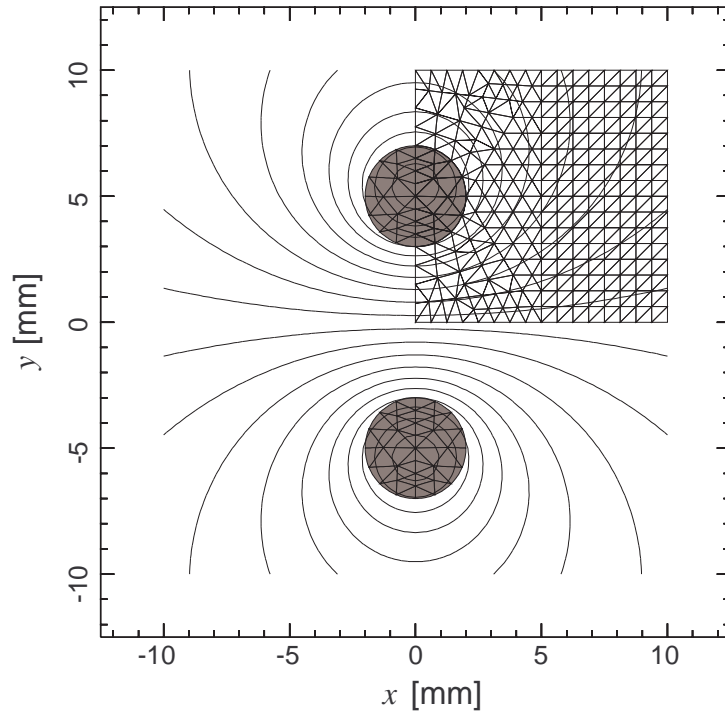


(a) Magnetic flux lines and meshes within picture frame.

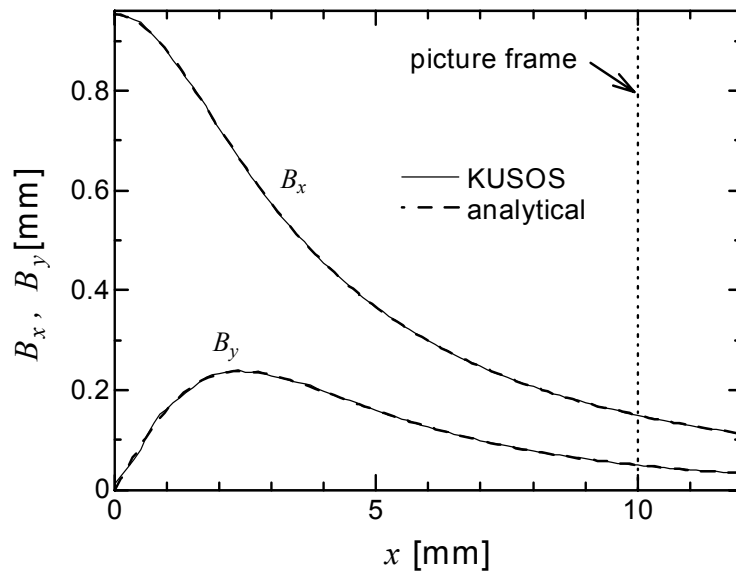


(b) Fields along $y = 2$ mm in the x -direction.

Figure 4.3. KUSOS results comparing with analytical solutions.



(a) Magnetic flux lines and meshes within picture frame.



(b) Fields along $y = 2$ mm in the x -direction.

Figure 4.4. KUSOS results with a different picture frame to the previous one shown in [Fig. 4.3](#).

Figure 4.4 shows the results for the same situation as Fig. 4.3 with another choice of picture frame, also showing good agreements with the analytical solutions.

Secondly, the KUSOS was applied to a more complex situation with a nonlinear medium whose permeability is given in Fig. 4.5. As shown in Fig. 4.6, there placed are a coil, a homogeneous medium with relative permeability $\mu/\mu_0 = 3000$, and the nonlinear medium, with three different choices of picture frames. In this situation, the analytical solution is not available for comparison, while it is clearly seen that the numerical solutions are not different among the three different choices of the picture frames. As shown in Figs 4.6(b) and (c), more than one picture frames with arbitrary shapes can be used in the present hybrid method.

Figure 4.7 shows the fields along $r = 38$ mm in the z -direction. Again, the numerical results are not different among the different choices of the picture frames. And also, the calculated fields are found well continuous and smooth on the picture frames.

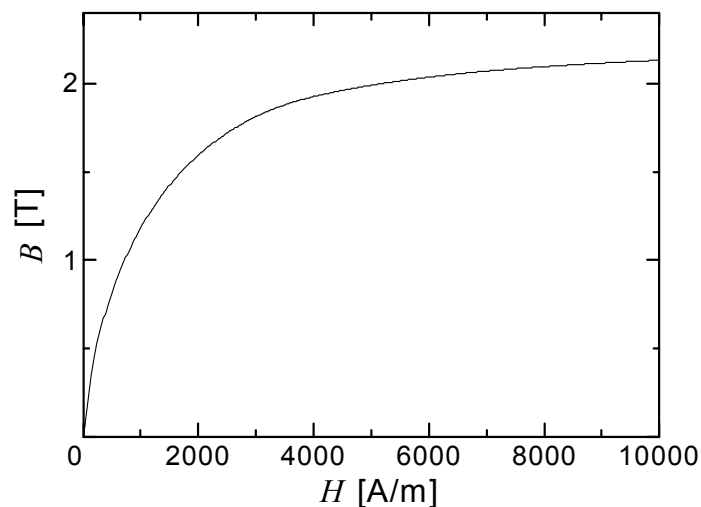
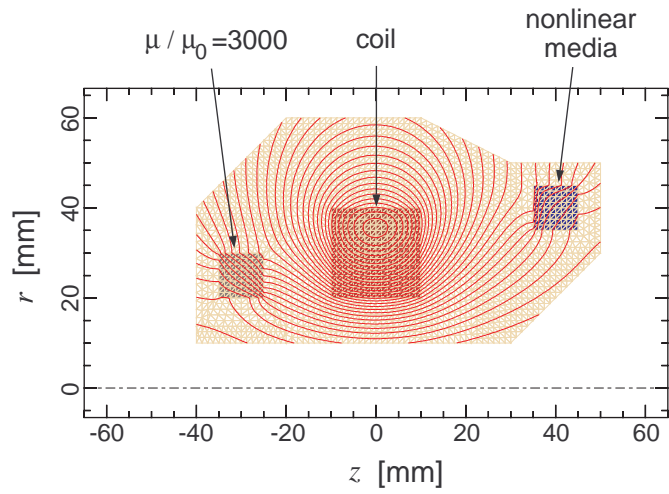
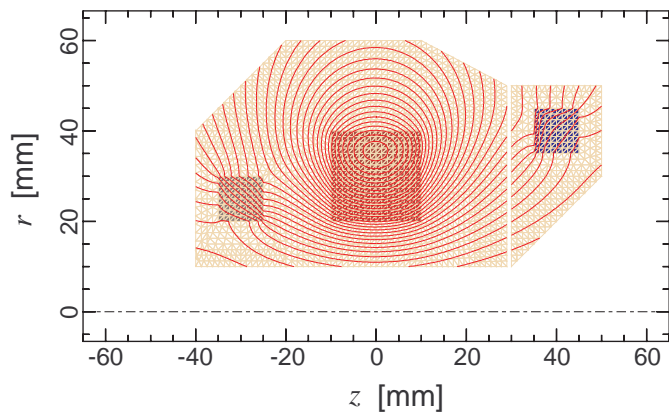


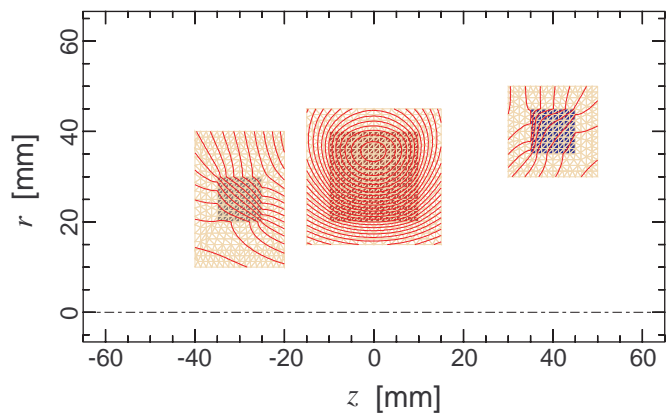
Figure 4.5. B as a function of H of the nonlinear medium in Fig. 4.6.



(a)



(b)



(c)

Figure 4.6. KUSOS results with three different picture frames, showing contour lines with $rA_\theta = \text{constanat}$, and meshes.

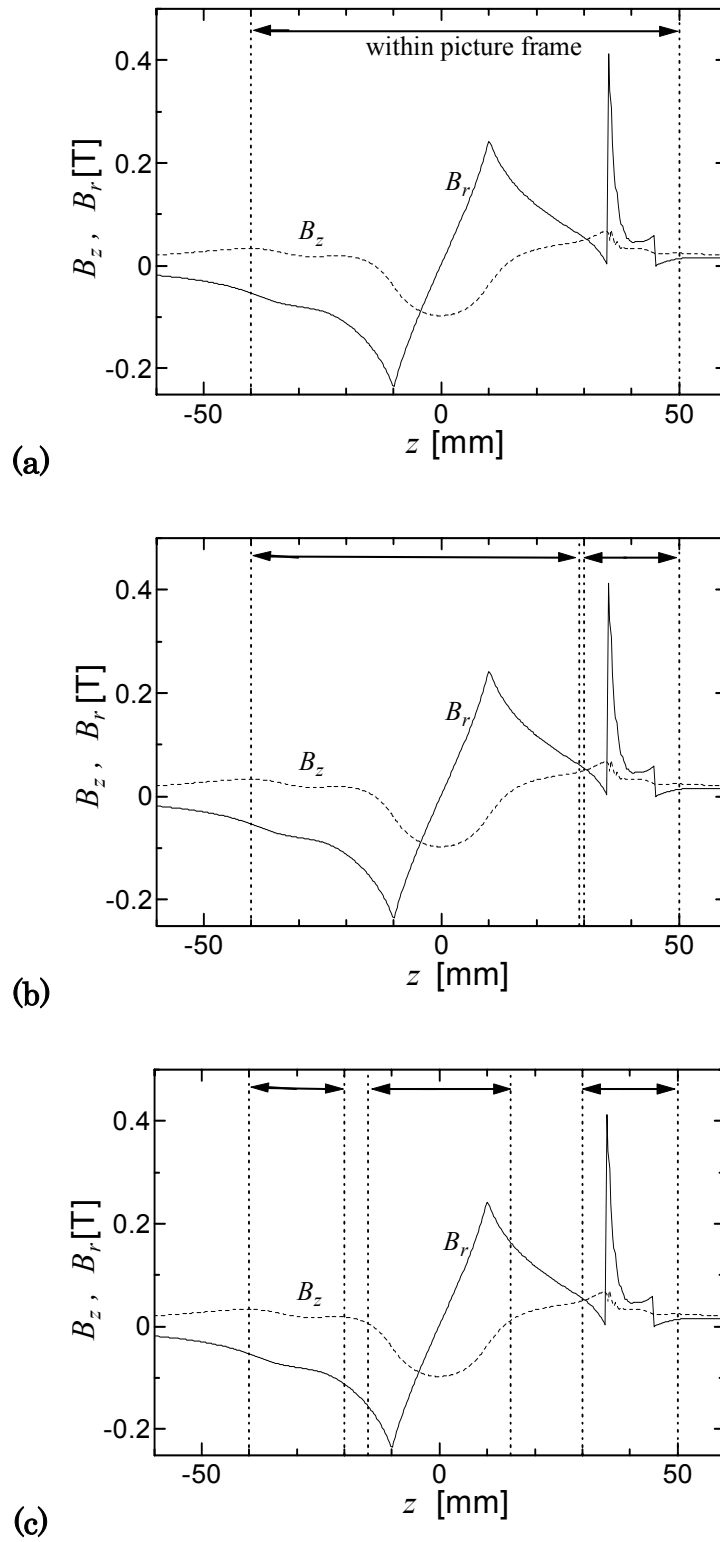
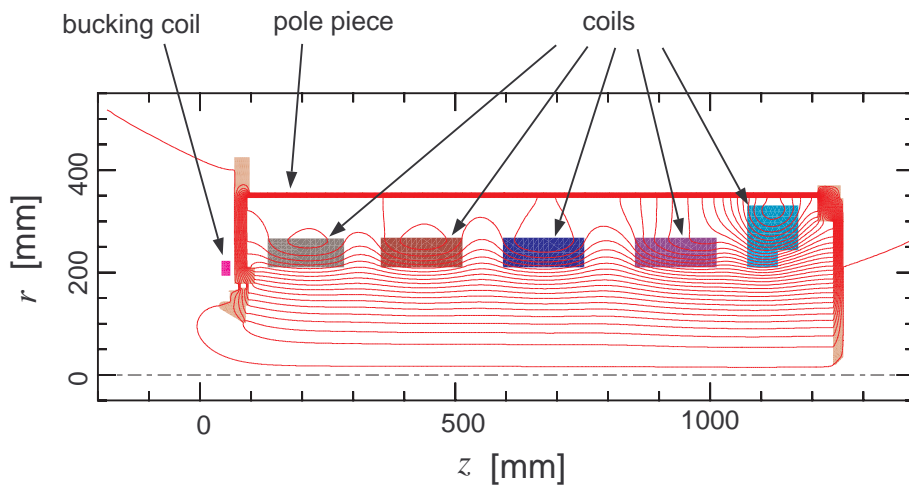
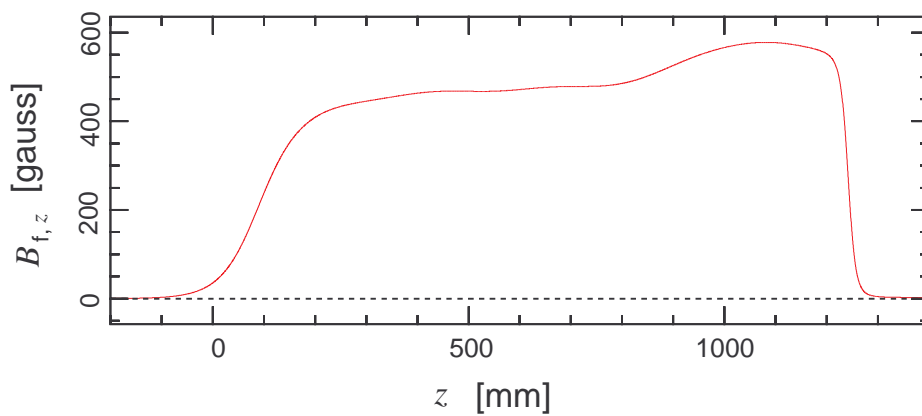


Figure 4.7. Field distributions of the KUSOS results shown in Fig. 4.6, along $r = 38$ mm in the z -direction.

Figure 4.8 shows the KUSOS results for a klystron focusing system, Toshiba E3718 (refer to Table 5.1 in Chapter 5). The calculated fields are to be used as the input data for the particle-in-cell simulations presented in the following chapters.



(a) Magnetic flux lines (contour lines with $rA_{t,\theta} = \text{constant}$).



(b) Magnetic flux on the axis.

Figure 4.8. KUSOS results for the E3718 klystron focusing coils.

4.4. Concluding Remarks

The FEM or the MM each has its own advantage and disadvantage. It is true that the FEM can easily deal with nonlinear media, but cannot with unbounded problems. The situation is opposite for the MM. The FEM/MM-hybrid method, on the other hand, retains the advantages associated with both methods, by applying the FEM to the interior region containing nonlinearity, and the MM to the exterior homogeneous region.

Presented in this chapter is a new FEM/MM-hybrid method used in the KUSOS for the unbounded magnetostatic fields with nonlinear media in 2-dimension, with the following summaries:

- (i) it gives a minimum for the energy functional in the infinite space, and consequently provides reliable solutions both inside and outside the finite elements,
- (ii) more than one picture frames can be used with arbitrary shapes, leading to efficient computations,
- (iii) the formulation guarantees both tangential and normal field continuities in an integral manner.

It is also found that the numerical test results show good agreements with analytical solutions, no difference in numerical solutions for different choices of the picture frames, and excellent continuity of magnetic fields between the interior and the exterior regions.

Chapter 5

Development of a 2-Dimensional Klystron Simulation Code

5.1. Introduction

Two particle-in-cell codes have been developed in this study, and are presented in [this chapter](#). One is the KUAD2 (acronym for Kyoto University Advanced Dart II) code for calculating trajectories in static fields applicable to electron gun simulations, and the other is the KUBLAI (Kyoto University Beam Loading Analysis) code for simulating interactions between beams and cavities. The results by the KUAD2 are to be used as the initial and beam-injection conditions for the time-domain KUBLAI simulations.

The KUAD2 is based on the recently developed KUAD (Kyoto University Advanced Dart) code [\[24, 39\]](#), and modifications have been made in this study to achieve further accuracy, which will be discussed in [subsection 5.2.1](#). The present KUAD2 was verified through comparisons with experiments in terms of gun perveances.

The KUBLAI is based on the existing klystron code known as FCI (Field Charge Interaction) developed by Shintake [\[19, 21\]](#). However, while the FCI shows reasonably high accuracy in RF output powers, following modifications have been made to improve the accuracy enough to be able to

provide injection conditions for depressed collector designing, as well as to reduce the computation time;

- (i) the KUBLAI can deal with a tapered drift-tube, which is, in the FCI, replaced approximately by a straight drift-tube of an intermediate radius for calculating the beam-induced fields,
- (ii) to stabilize the numerical instability in calculating simultaneously both the electron motions and the beam-induced fields, the FCI uses both spatial smoothing of the fields, and artificial damping factors between the output cavity and the collector, which is sufficient for the klystron designing, but not appropriate enough to obtain the parameters associated with the spent beams for the depressed collector designing. A more straightforward and appropriate method was thus developed in this study, and applied to the KUBLAI, as will be described in [subsection 5.2.3](#).
- (iii) the numerical method for calculating cavity voltages was modified to achieve faster convergence on the final periodically steady-state solutions, which will be described in [subsection 5.2.4](#).

Also presented are comparisons between the KUBLAI simulations and klystron experiments for verifications, in terms of RF output powers.

5.2. Numerical Methods

5.2.1. Initial and Beam-Injection Conditions

For the time-domain KUBLAI simulations, initial fields, initial electron distribution in the drift-tube, and beam-injection conditions are all

calculated by use of the KUAD2 code. The KUAD2 has been developed by modifying the KUAD code as follows,

- (i) instead of linear triangular elements used in the KUAD for the field calculations, the present KUAD2 uses quadratic elements, which is found to result in higher accuracy (see [chapter 3](#)),
- (ii) the KUAD2 calculates the angular component of the beam-induced vector potential, which is neglected in the KUAD.

The modification (ii) is necessary to provide the initial fields for the time-domain KUBLAI simulations.

[Figure 5.1](#) shows the flow chart of the KUAD2. Just as the same as the KUAD code, it calculates the current density distribution on the cathode, the electron trajectories in the gun and the drift-tube, and the beam-induced fields, iteratively, until self-consistent solutions are obtained.

The trajectories are calculated by solving [Eq. \(2.41\)](#) using the Runge-Kutta method. The beam-induced fields are, then, calculated by solving [Eqs. \(2.30\)](#), by use of the Finite

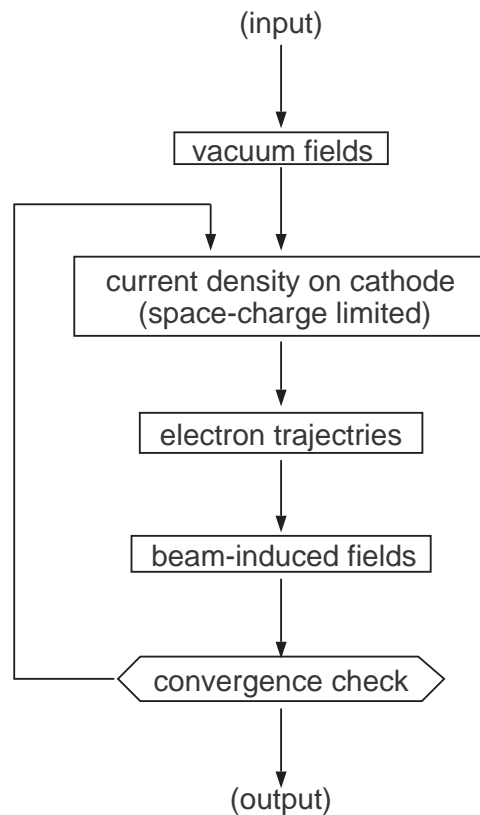


Figure 5.1. Flow chart of the KUAD2.

Element method (FEM) with quadratic triangular elements. The calculated fields, then, give the successive current density on the cathode, by applying Child Low [40] locally within the triangular elements on the cathode surface.

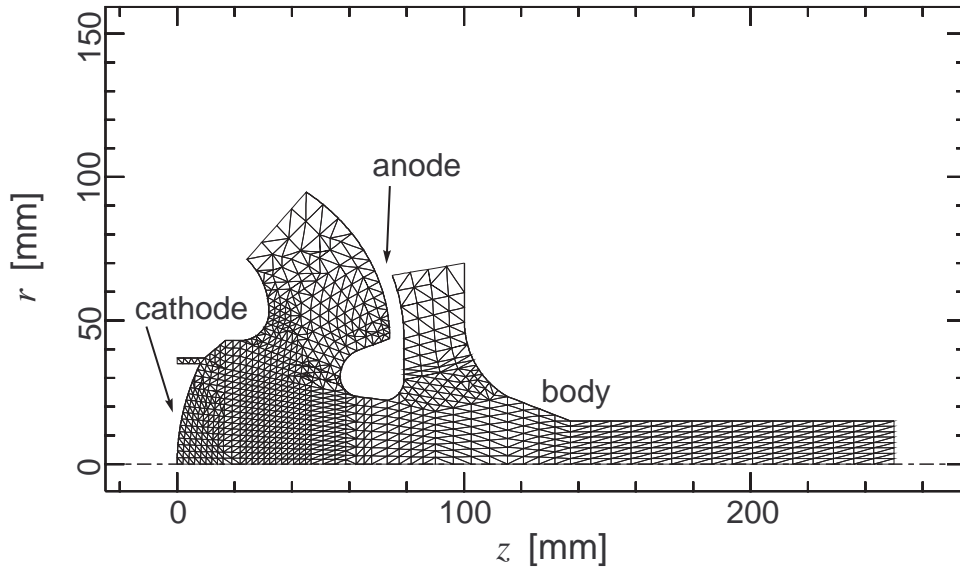
Triangular meshes and trajectories in the Toshiba klystron E3718#3 (see Table 5.1), for example, are shown in Figs. 5.2(a) and 5.2(b).

To verify the present KUAD2, gun perveances with various cathode voltages were calculated for the E3718#3 klystron. As summarized in Table 5.1, the E3718#3 has two different operational modes, namely CW and pulse operation, with different perveances.

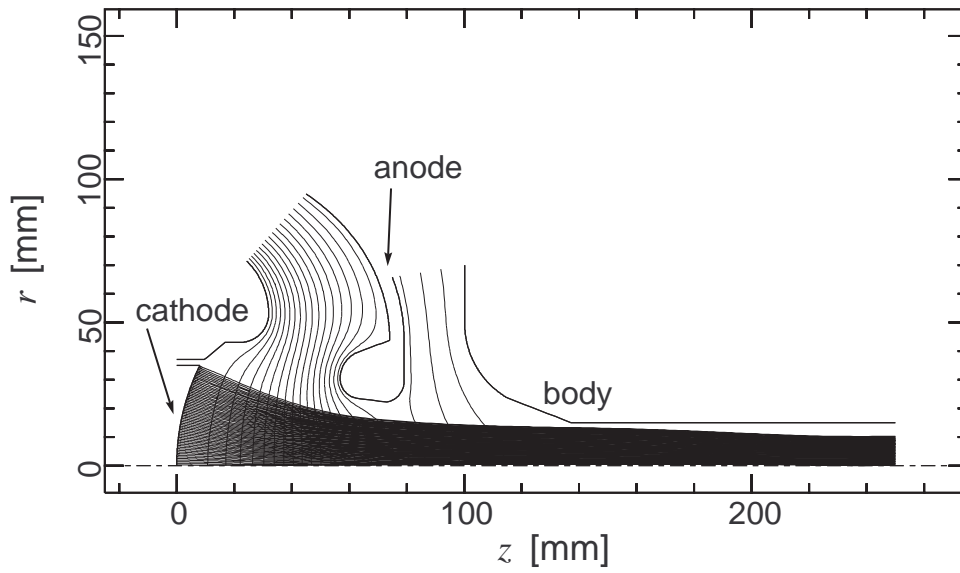
As is seen in Fig. 5.3, the KUAD2 results are found to show excellent agreements with experiments, within $-2.3\% \sim +2.4\%$ relative errors with respect to the measured values. The errors are summarized in Table 5.2.

Table 5.1. Characteristics of klystrons for code verifications.

	Toshiba E3718#3		Toshiba	SLAC
	CW	pulse	1AV56	XK-5
frequency [MHz]	1250	1250	615	2856
# of cavities	6	6	4	5
beam voltage [kV]	83	147	17	265
beam current [A]	22	57	2.2	286
beam power [MW]	1.8	8.3	0.038	76
perveance [$\mu A/V^{3/2}$]	0.9	1.0	1.0	2.1
output [MW]	1.0	3.6	17	36
efficiency [%]	58	43	45	48

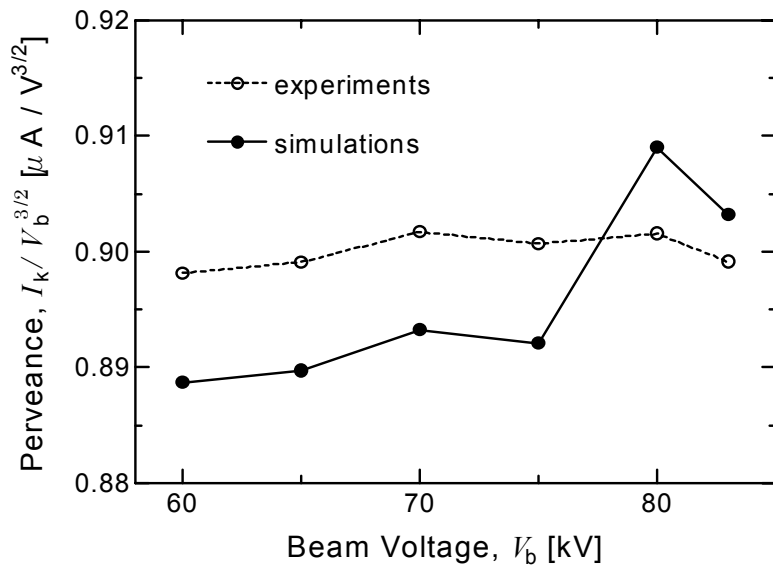


(a) Meshes.

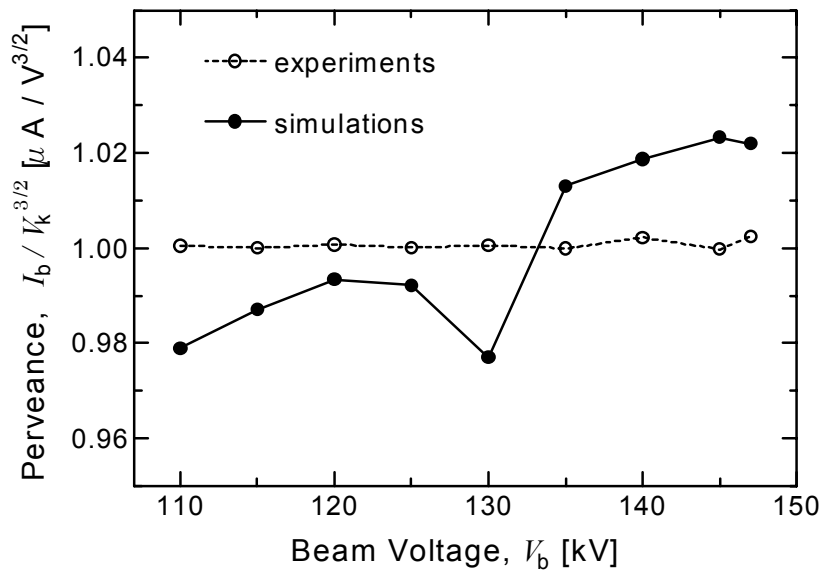


(b) Electron trajectories.

Figure 5.2. Meshes, and electron trajectories calculated by the KUAD2, in the electron gun of the E3718#3 klystron.



(a) CW mode.



(b) Pulse mode.

Figure 5.3. Gun perveance of the E3718#3 klystron as a function of beam voltage (voltage between cathode and body), comparing the KUAD2 simulations and experiments

Table 5.2. Beam current from electron gun of E3718#3, comparing KUAD2 simulations and experimental measurements.

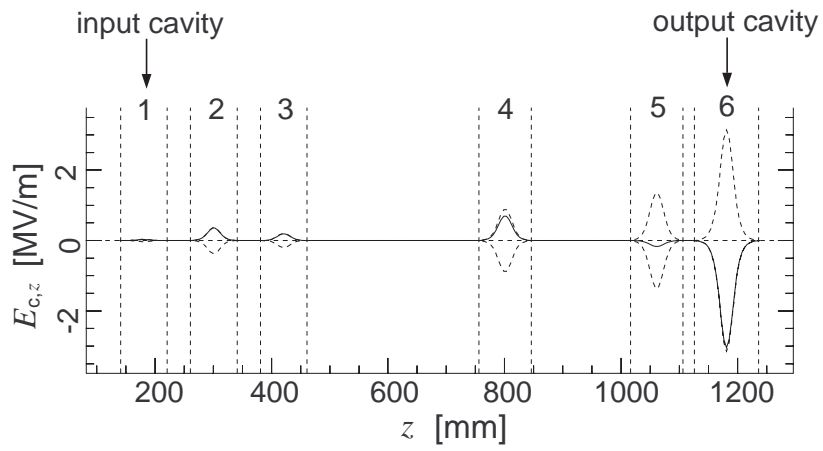
	V_b [kV]*	V_a [kV]*	current [A]		
			simulation	experiment	error [%]
CW mode	60	49.4	13.1	13.2	-0.8
	65	53.6	14.7	14.9	-1.3
	70	57.9	16.5	16.7	-1.2
	75	62.0	18.3	18.5	-1.1
	80	67.0	20.6	20.4	+1.0
	83	69.2	21.6	21.5	+0.5
pulse mode	110	97	35.7	36.5	-2.2
	115	102	38.5	39.0	-1.3
	120	107	41.3	41.6	-0.7
	125	112	43.8	44.2	-0.9
	130	117	45.8	46.9	-2.3
	135	122	50.3	49.6	+1.4
	140	127	53.4	52.5	+1.7
	145	132	56.5	55.2	+2.4
	147	133.7	57.6	56.5	+1.9

* V_b : voltage between cathode and body (drift-tube)

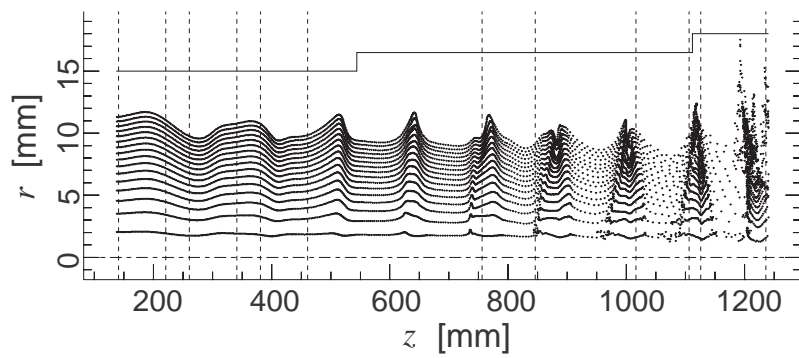
* V_a : voltage between cathode and anode

5.2.2. Flow Chart

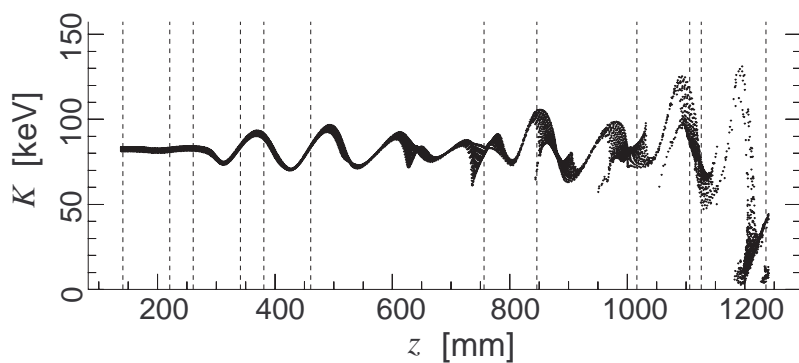
The KUBLAI simulates electron motions and beam-induced fields in time domain. It also calculates cavity voltages by use of the equivalent circuit model described in [chapter 2](#). [Figures 5.4 and 5.5](#) show, respectively, a simulation result of the E3718#3 klystron, for example, and the flow chart.



(a) Cavity fields on the axis.



(b) Electron distribution.



(c) Electron kinetic energy.

Figure 5.4. Snapshot in the E3718#3 klystron by KUBLAI simulation (beam voltage $V_b = 83$ kV, beam current $I_k = 21.5$ A). The dashed lines indicate axial positions of the cavities.

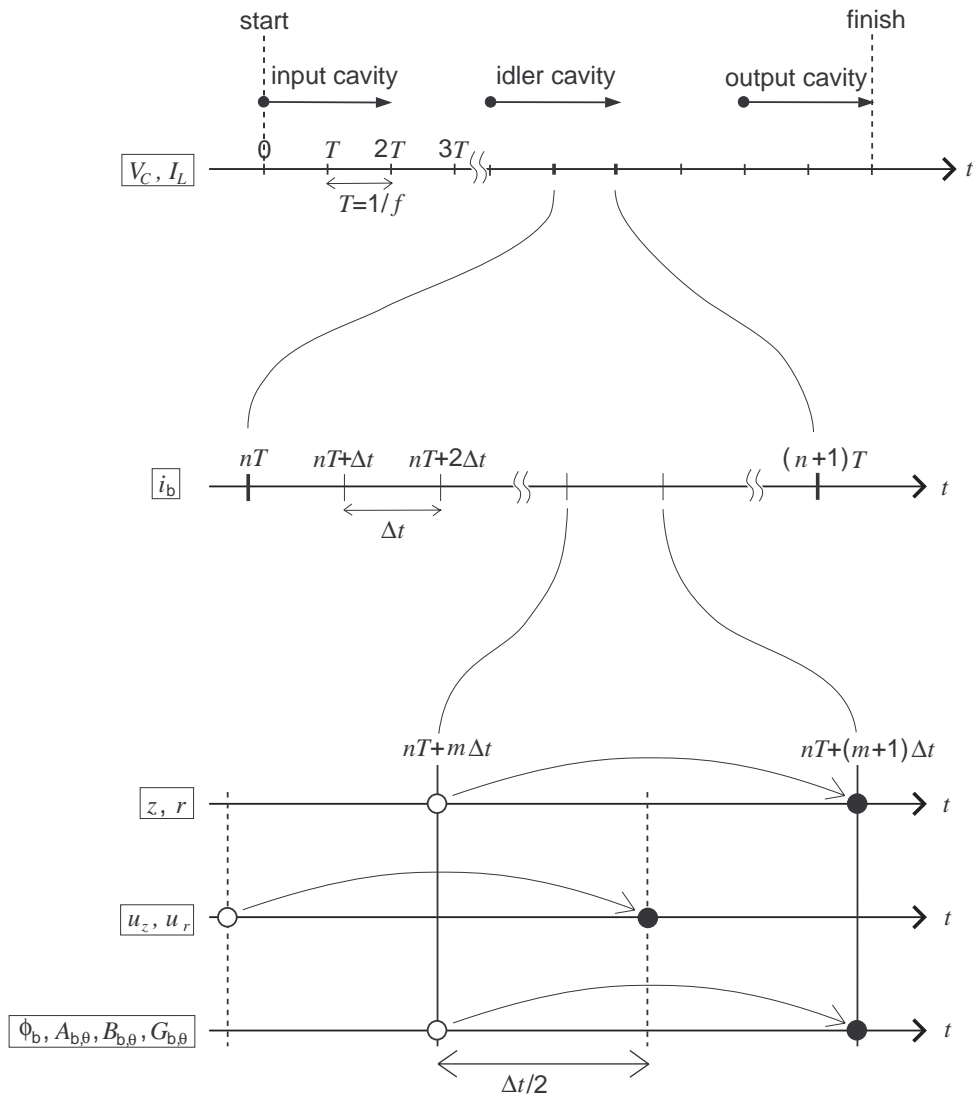


Figure 5.5. Time stepping processes of the KUBLAI.

In Fig. 5.4, the electron beam, which consists of ring particles (see Fig. 2.2), is injected through the injection boundary on the left, interacts with the cavity fields through the drift-tube, and, then, goes out of the drift-tube from the exit boundary on the right.

As shown in Fig. 5.5, the cavity voltages are calculated successively from the input cavity to the output cavity. The cavity voltage V_C is revised

in every RF periods iteratively, as will be described in [subsection 5.2.4](#). The iterations for each cavity voltage are started when the ring particles modulated by the upstream cavity reach.

In the calculations of the electron motions, and the beam-induced fields, each RF period T ($=1/f$) is divided into time steps Δt .

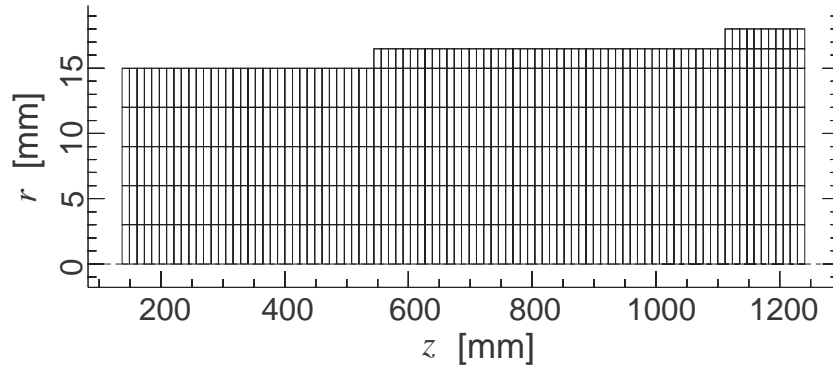
At each time step, the electron motions are calculated in a leap-frog manner as shown in [Fig. 5.5](#), by solving [Eqs. \(2.36\)](#), and, then, the beam-loading current at that time $i_b(t)$ is calculated by [Eq. \(2.11.f\)](#), and stored in computer memories. The stored beam-loading currents through one RF-period are transformed by [Eq. \(2.18\)](#) into the complex beam-loading current I_b , which is to be used for revising the cavity voltage.

The beam-induced fields are also calculated at each time step by solving [Eqs. \(2.26\)](#), as will be described in [the following subsection](#).

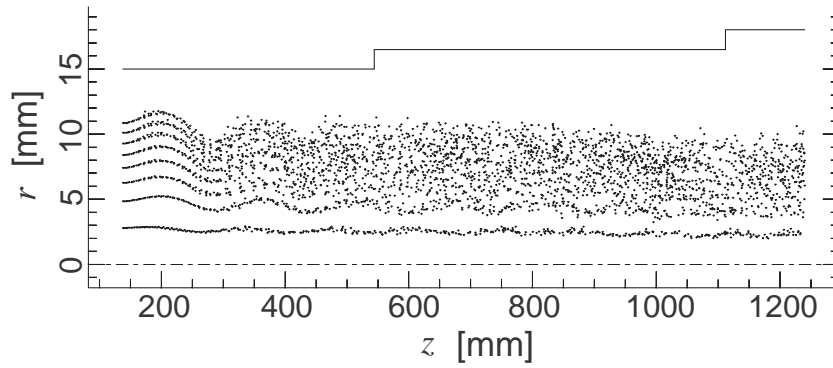
5.2.3. A Stabilization Method of Numerical Instabilities in Time-Domain Field Calculations

A numerical instability has been observed [\[21\]](#) in calculating simultaneously electromagnetic fields, and charged particle motions by use of the Finite Differential method (FDM).

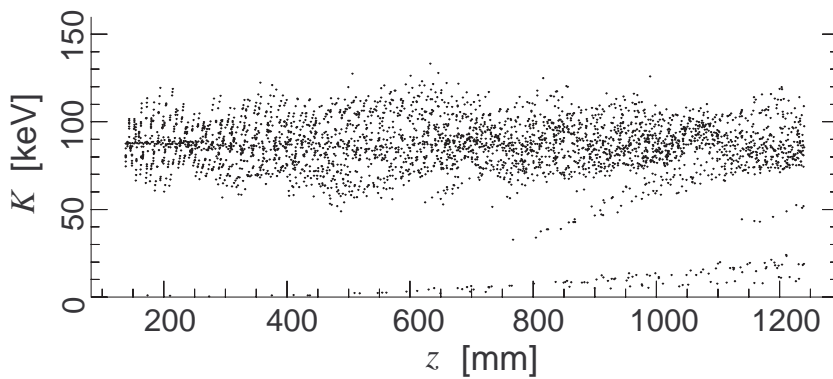
Also by use of the FEM in this study in the course of the KUBLAI code development, the high-frequency instability has been seen as shown in [Fig. 5.6](#), where the beam is found unreasonably modulated, and bunched periodically according to the mesh size. The bunched beam tends to excite the high-frequency non-physical electromagnetic fields, whereas the excited fields modulate the bunched beam further, and finally the fields are led to oscillate. This instability can hardly be avoided by use of larger numbers of meshes, nor time steps.



(a) Meshes.



(b) Electron distribution.



(c) Electron kinetic energy.

Figure 5.6. Numerical instability seen in the KUBLAI simulation with a DC beam (90 kV, 24.3 A), by use of the basic Newmark method.

In this subsection, a method is proposed to stabilize this non-physical instability.

By applying the FEM using quadratic rectangular elements with N nodes (see Fig. 5.6(a), for example), Eqs. (2.26) are reduced to simply the following ordinary differential equations,

$$A_\phi \mathbf{x}_\phi = \mathbf{f}_\phi, \quad (5.1.a)$$

$$A_A \mathbf{x}_A + B_A \frac{d\mathbf{x}_A}{dt} + C_A \frac{d^2 \mathbf{x}_A}{dt^2} = \mathbf{f}_A, \quad (5.1.b)$$

$$A_B \mathbf{x}_B + B_B \frac{d\mathbf{x}_B}{dt} + C_B \frac{d^2 \mathbf{x}_B}{dt^2} = \mathbf{f}_B, \quad (5.1.c)$$

$$A_G \mathbf{x}_G = \mathbf{f}_G, \quad (5.1.d)$$

where \mathbf{x} 's are N -dimensional unknown vectors, \mathbf{f} 's are time-dependent source terms, and A 's, B 's, and C 's are constant matrices determined by the mesh configuration.

There are many candidates for the numerical method to solve the ordinary differential equations of Eqs. (5.1.b) and (5.1.c). Among them, the Newmark method [41] has an advantageous feature of not requiring the well-known Courant-Freidrichs condition. In many other methods such as the Runge-Kutta method, the time step Δt must be set less than a specific value related to the mesh size Δz , and Δr as follows,

$$c\Delta t \leq h\sqrt{\Delta z^2 + \Delta r^2}, \quad (5.2)$$

where h is a given constant less than unity. The Courant-Freidrichs

condition of Eq. (5.2) is quite undesirable for the klystron simulation, since it tends to lead to many time steps, and accordingly too much CPU time.

For this reason, while other codes such as the FCI [19, 21], and the MAFIA [20] use the Euler method in a leap-frog manner (called the “Finite Differential Time-Domain” method), the Newmark method was originally used in the KUBLAI. In cases without beams, or with low current beams, the field calculations are found stable for any choice of the time step Δt , as was expected.

However, in the case of an intense beam, the instability previously shown in Fig. 5.6 was observed. This is exclusively due to the fact that, with high current beams, the source terms f ’s in Eqs. (5.1) show strongly nonlinear dependence on the variables \mathbf{x} ’s. Thus the Newmark method is found not always stable for nonlinear equations, although it is known to be stable for linear ones.

By modifying the Newmark method to provide higher stability even in the case of intense beams, a new method has been developed in this study, whose procedure is described as follows,

$$\mathbf{A}\mathbf{x}_{(n+1)} + \mathbf{B}\dot{\mathbf{x}}_{(n+1)} + \mathbf{C}\ddot{\mathbf{x}}_{(n+1)} = \mathbf{f}_{(n+1)}, \quad (5.3.a)$$

$$\dot{\mathbf{x}}_{(n+1)} = \dot{\mathbf{x}}_{(n)} + \Delta t \frac{\ddot{\mathbf{x}}_{(n)} + \ddot{\mathbf{x}}_{(n+1)}}{2}, \quad (5.3.b)$$

$$\mathbf{x}_{(n+1)} = \mathbf{x}_{(n)} + \Delta t \dot{\mathbf{x}}_{(n)} + \left(\frac{1}{2} + \delta\right)\Delta t^2 \ddot{\mathbf{x}}_{(n)} + \beta\Delta t^2(\ddot{\mathbf{x}}_{(n+1)} - \ddot{\mathbf{x}}_{(n)}), \quad (5.3.c)$$

where the potential at $(n+1)$ -th step, $\mathbf{x}_{(n+1)}$, $\dot{\mathbf{x}}_{(n+1)}$, and $\ddot{\mathbf{x}}_{(n+1)}$ are given by those at the previous time step, $\mathbf{x}_{(n)}$, $\dot{\mathbf{x}}_{(n)}$, and $\ddot{\mathbf{x}}_{(n)}$, and the source vector $\mathbf{f}_{(n+1)}$. The factors δ and β are constant, and the former was newly

introduced. With $\delta=0$, the present method of Eqs. (5.3) coincides with the basic Newmark method.

From Eqs. (5.3.b) and (5.3.c), the following expression can be derived,

$$\mathbf{x}_{(n+1)} = \mathbf{x}_{(n)} + \Delta t \frac{\dot{\mathbf{x}}_{(n+1)} + \dot{\mathbf{x}}_{(n)}}{2} + \delta \Delta t^2 \frac{\ddot{\mathbf{x}}_{(n+1)} + \ddot{\mathbf{x}}_{(n)}}{2} + \left(\beta - \frac{\delta}{2} - \frac{1}{4} \right) \Delta t^3 \frac{\ddot{\mathbf{x}}_{(n+1)} - \ddot{\mathbf{x}}_{(n)}}{\Delta t}. \quad (5.4)$$

This expression is found related to the stability conditions as follows.

For linear systems without beams, it is known that the basic Newmark method ($\delta=0$) is stable for any large Δt (or, for any small Δz and Δr), so long as the factor β satisfies the following condition,

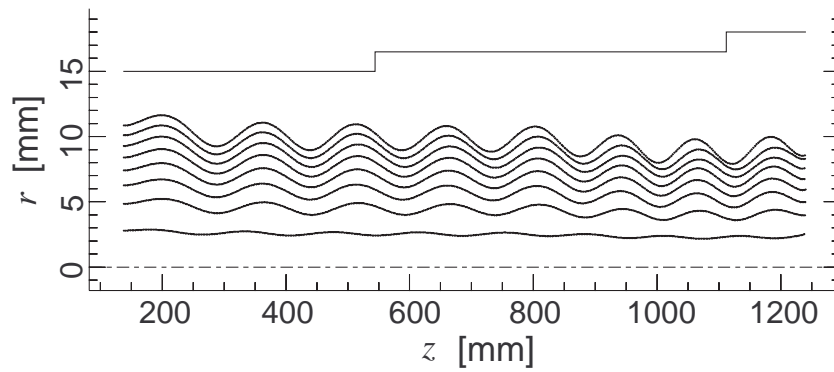
$$\beta \geq \frac{1}{4}, \quad \delta = 0. \quad (5.5)$$

In contrast, through numerical examinations with the KUBLAI varying the factors δ and β from zero to unity, the stability condition of the modified Newmark method is found,

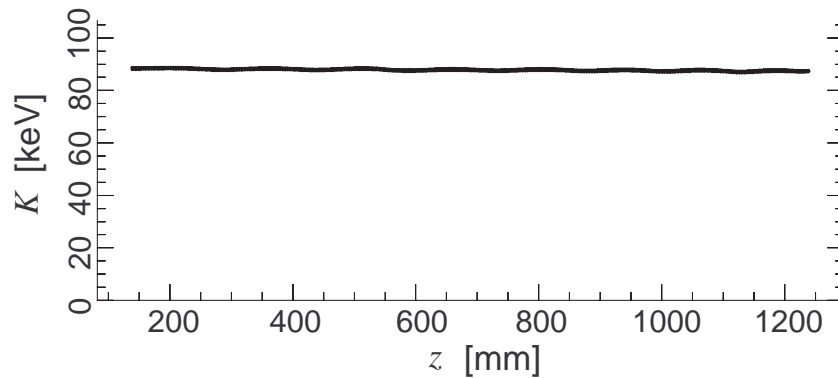
$$\beta - \frac{\delta}{2} \geq \frac{1}{4}, \quad \delta \geq 0, \quad (5.6)$$

which is easily found consistent with the condition of Eq. (5.5) for the basic Newmark method. And furthermore, the condition of Eq. (5.6) is found to indicate simply that the factors δ and $(\beta - \delta/2 - 1/4)$ in Eq. (5.4) must be positive.

For the the intense beam previously shown in Fig. 5.6, the modified Newmark method is empirically found to show quite high stability with the factors around $\delta=1/3$ and $\beta=5/12$, as shown in Fig. 5.7. The non-physical beam-modulation was not seen in Fig. 5.7 during 300 RF periods, while, with the basic Newmark method, it was observed after only 20 RF periods as seen in Fig. 5.6.



(a) *Electron distribution.*



(b) *Electron kinetic energy.*

Figure 5.7. KUBLAI results by use of the modified method. The numerical instability seen in Fig. 5.6 was stabilized.

5.2.4. A Method for Fast Convergence in Simulating Beam-Cavity Interactions

Since the equivalent circuits shown in Fig.2.2 represent resonance with high quality factors up to several thousands, it takes very much CPU time to obtain the final periodically steady-state solutions by solving Eqs. (2.13) in time domain. For example, for a cavity with a quality factor of 3000, starting at the initial cavity voltage of 0V, it will take around 3000 RF periods to approach the solution within a 2.5% error.

To overcome this problem, Eqs. (2.13) are solved in frequency-domain in the existing codes [16-21], as well as in the KUBLAI. With Eqs. (2.18) and (2.19), Eqs. (2.13) are expressed by,

$$\left(j\omega C^{(i)} + \frac{1}{R^{(i)} + j\omega L^{(i)}} \right) V_C^{(i)} = I_b^{(i)} + I_{\text{ext}}^{(i)}, \quad (5.7.a)$$

$$I_L^{(i)} = \frac{V_C^{(i)}}{R^{(i)} + j\omega L^{(i)}}, \quad (5.7.b)$$

and further with Eq. (2.15.b), for example for the output cavity, Eq. (5.7.a) can be written as,

$$Y^{(i)} V_C^{(i)} = I_b^{(i)}, \quad (5.8)$$

where,

$$Y^{(i)} = G^{(i)} + j\omega C^{(i)} + \frac{1}{R^{(i)} + j\omega L^{(i)}}. \quad (5.9)$$

Since the beam-loading current $I_b^{(i)}$, which is given by Eqs. (2.11.f)

and (2.18), depends on the electron trajectories, it depends nonlinearly on the cavity voltage $V_C^{(i)}$.

In order to obtain quickly the final steady-state cavity voltage $V_C^{(i)}$, the following three methods are used in the FCI code [21], and are reviewed in the followings:

- (i) By assuming the beam-loading current $I_b^{(i)}$ to be linear to the cavity voltage $V_C^{(i)}$ as,

$$I_b^{(i)}(V_C^{(i)}) = I_{b0}^{(i)} - Y_b^{(i)}V_C^{(i)}, \quad (5.10)$$

where, $I_{b0}^{(i)} = I_b^{(i)}(0)$ is the beam-loading current with $V_C^{(i)} = 0$, and $Y_b^{(i)}$ (called beam-admittance) is a constant determined by a previous simulation with a specific cavity voltage, the solution can be obtained immediately by,

$$V_C^{(i)} = \frac{I_{b0}^{(i)}}{Y^{(i)} + Y_b^{(i)}}. \quad (5.11)$$

This linear approximation is supposed not appropriate for high cavity voltages, and therefore, in the FCI, applied only to the cavities of lower voltages compared with the beam voltage.

- (ii) With the beam-loading current $I_{b,(n)}^{(i)} = I_b^{(i)}(V_{C,(n)}^{(i)})$ calculated by the electron motions with the cavity voltage $V_{C,(n)}^{(i)}$, the successive $V_{C,(n+1)}^{(i)}$ is given by,

$$V_{C,(n+1)}^{(i)} = \frac{V_{C,(n)}^{(i)} + \frac{I_{b,(n)}^{(i)}}{Y^{(i)}}}{2}. \quad (5.12)$$

This procedure will be continued until $V_{C,(n)}^{(i)}$ and $I_{b,(n)}^{(i)}$ satisfy Eq. (5.9). In the FCI, this method is applied to the idler cavities of high voltages. The initial voltage $V_{C,(0)}^{(i)}$ is given by the linear approximation (i).

(iii) With the expression,

$$v_C^{(i)} = \text{Re}[V_C^{(i)}(t)\exp(j\omega t)], \quad (5.13.a)$$

$$i_L^{(i)} = \text{Re}[I_L^{(i)}(t)\exp(j\omega t)], \quad (5.13.b)$$

the following differential equations can be obtained from Eqs. (2.13) and (2.15.b),

$$C^{(i)} \frac{dV_C^{(i)}}{dt} = -(G^{(i)} + j\omega C^{(i)})V_C^{(i)} - I_L^{(i)} + I_b^{(i)}, \quad (5.14.a)$$

$$L^{(i)} \frac{dI_L^{(i)}}{dt} = -(R^{(i)} + j\omega L^{(i)})I_L^{(i)} + V_C^{(i)}. \quad (5.14.b)$$

Then, successive $V_{C,(n+1)}^{(i)}$, and $I_{L,(n+1)}^{(i)}$ are given by,

$$V_{C,(n+1)}^{(i)} = V_{C,(n)}^{(i)} + \sigma T \frac{dV_C^{(i)}}{dt} (V_{C,(n)}^{(i)}, I_{L,(n)}^{(i)}), \quad (5.15.a)$$

$$I_{L,(n+1)}^{(i)} = I_{L,(n)}^{(i)} + \sigma T \frac{dI_L^{(i)}}{dt} (V_{C,(n)}^{(i)}, I_{L,(n)}^{(i)}), \quad (5.15.b)$$

where σ is a factor more than unity to fasten the solution convergence. A

larger σ results, of course, in faster convergence. However, this method has the disadvantage in that that, with too large σ , $V_C^{(i)}$ and $I_L^{(i)}$ do not converge to the final solutions, and hence care must be taken in the choice of the factor σ . And further, since σ has its upper limit (typically around 20), it still takes more than hundreds RF periods for cavities with high qualities up to 3000. In the FCI, this method is used only for the output cavity, which has some low quality factor typically less than 50.

In the present KUBLAI developed in this study, considering the disadvantages of the methods (i) and (iii), basically a method similar to (ii) is used for all cavities. But again a modification has been made to provide faster convergence to the steady-state solutions. The modified method is described by,

$$V_{C,(n+1)}^{(i)} = V_{C,(n)}^{(i)} \frac{I_{b0}^{(i)}}{Y^{(i)} V_{C,(n)}^{(i)} + I_{b0}^{(i)} - I_{b,(n)}^{(i)}}. \quad (5.16)$$

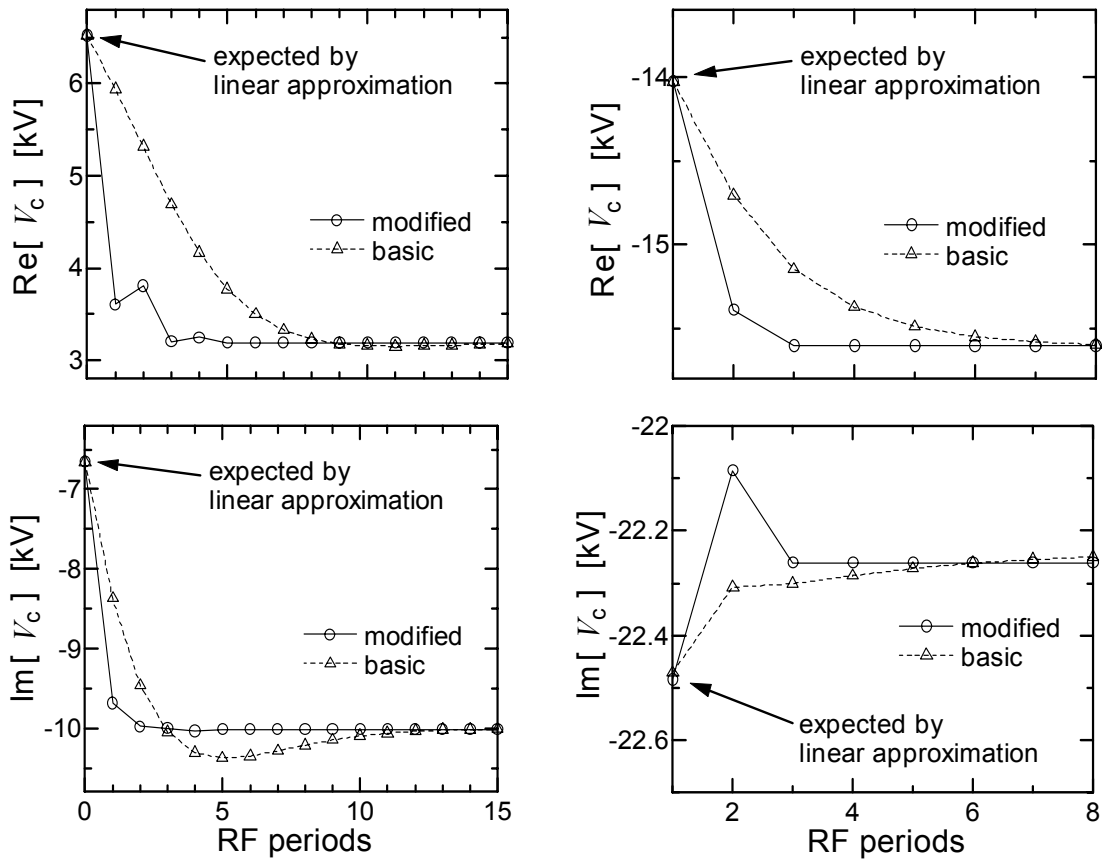
Further, Eq. (5.16) can be rewritten as,

$$V_{C,(n+1)}^{(i)} = \frac{I_{b0}^{(i)}}{Y^{(i)} + Y_{b,(n)}^{(i)}}, \quad (5.17.a)$$

$$Y_{b,(n)}^{(i)} = \frac{I_{b0}^{(i)} - I_{b,(n)}^{(i)}}{V_{C,(n)}^{(i)}}, \quad (5.17.b)$$

and, hence, the modified method is similar to the method (i) as well, with the beam-admittance $Y_{b,(n)}^{(i)}$ revised at each RF cycle n .

The method (ii), and the present method was compared through KUBLAI simulations of the E3718#3 klystron. Figure 5.7 shows variations of calculated cavity voltages through iterations, for the 2nd and 4th cavities of the E3718#3 klystron. The modified method is found to show faster convergence to the steady-state solutions, compared with the basic method (ii). With the modified method, the solutions are found to converge with 3~9 RF periods within 0.1% errors, for the E3718#3 cavities with various quality factors, and beam voltages.



(a) E3718#3, 2nd cavity ($Q = 3000$).

(b) E3718#3, 4th cavity ($Q = 3000$).

Figure 5.8. Variation of cavity voltages through iterative calculations, comparing two different methods.

5.3. Comparisons with Experiments

To verify the developed KUBLAI code, comparisons were made between calculated output powers and experimentally measured ones. Three klystrons, the E3718#3, the Toshiba 1AV56, and the SLAC XK-5, were used for comparisons, whose major characteristics are summarized in [Table 5.1](#).

[Figures 5.9 and 5.10](#) show the calculated and measured output powers for the E3718#3 klystron, [Fig. 5.11](#) for the 1AV56, and [Fig.5.12](#) for the XK-5, respectively. All these numerical results are found to show excellent agreements with experiments, within $-4.9\% \sim +6.9\%$ relative errors in the saturated output powers.

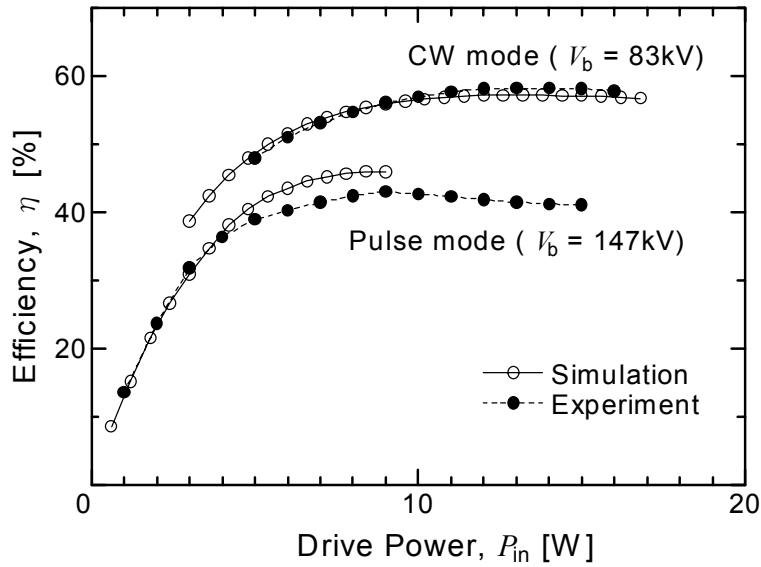


Figure 5.9. Efficiency as a function of drive power (E3718#3).

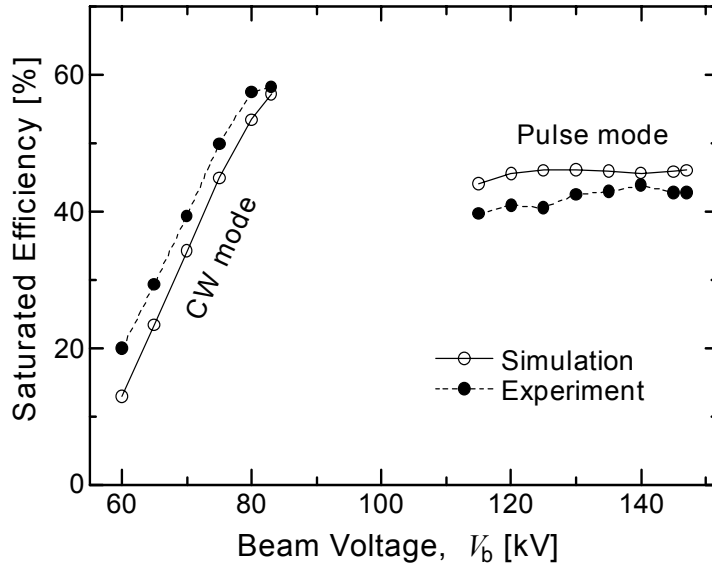


Figure 5.10. Saturated efficiencies for various beam voltages (E3718#3).

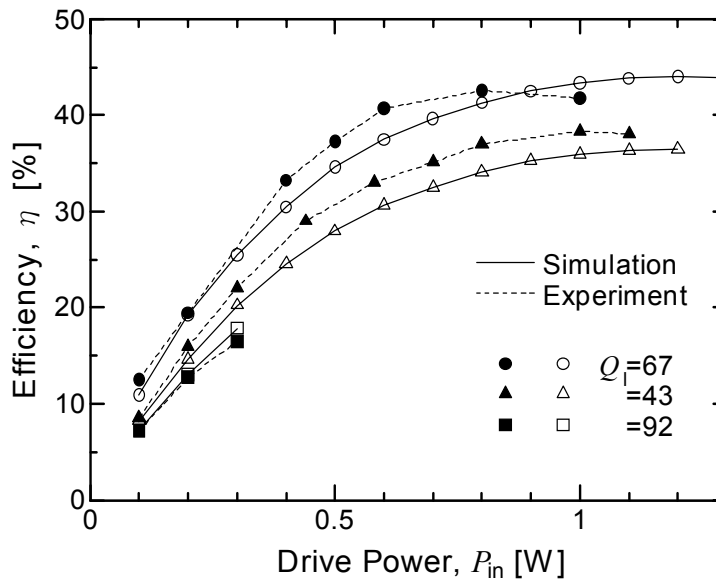


Figure 5.11. Efficiencies as functions of drive power, with three different loaded quality factor Q_l of the output cavity (1AV56).

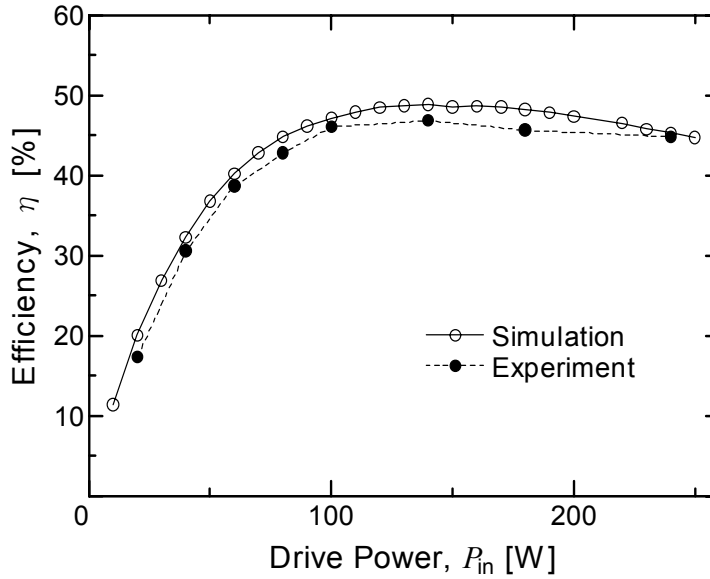


Figure 5.12. Efficiency as a function of drive power (XK-5).

5.4. Concluding Remarks

In this chapter, the 2-dimensional particle-in-cell simulation codes, namely the KUAD2, and the KUBLAI, developed in this study are presented.

The KUAD2 was verified through comparisons of gun perveances with experiments, showing good agreements within $-2.3\% \sim +2.4\%$ errors in the gun perveances.

On the development of the KUBLAI, a modified Newmark method was proposed to stabilize the numerical instability in calculating both electron motions, and beam-induced fields simultaneously. Numerical test results with the present method are found sufficiently stable.

A newly modified method for calculating cavity voltages was also

proposed, showing faster convergence to the steady-state solution than the basic method.

Comparisons were also made between output powers calculated by the developed KUBLAI code, and experimentally measured ones, showing excellent agreements within $-4.9\% \sim +6.9\%$ errors in the saturated output powers.

Chapter 6

Application to Klystron Efficiency Enhancement

6.1. Introduction

In this chapter, the two approaches for the klystron efficiency enhancement described in [chapter 1](#), namely depressed collectors, and hollow beams, are investigated by use of the developed and verified codes. An existing high-power klystron, Toshiba E3718#2 was taken as a reference in this study. The beam parameters, and the prototype performances by the KUBLAI simulations are shown in [Table 6.1](#).

Table 6.1. *Beam Parameters and calculated performances of the E3718#2 klystron.*

operating frequency	1.25 GHz
beam voltage	90 kV
beam current	24.3 A
perveance	0.9 $\mu\text{V}^{3/2}/\text{A}$
output power	1.32 MW
efficiency	60.5 %

In [section 6.2](#), the efficiency enhancements by virtue of multistage depressed collectors (MDC) are discussed. Firstly, efficiencies were calculated on the assumption of negligence of beam optics, in order to evaluate the theoretical limit of the energy recovery by MDCs, and also to determine initial design parameters such as number of electrodes, and electrode potentials, reasonably well. Secondly, a MDC was, then, designed by use of the KUAD2 particle-in-cell simulations.

The other approach by use of hollow beams was also studied, and is presented in [section 6.3](#). Because, in general, the cavity fields are stronger in the vicinity of the cavity gap on the drift-tube wall than near the symmetry axis, hollow beams are expected to enhance the klystron efficiency through more efficient interactions with the cavities than the solid beam whose innermost part least interacts. To examine this possibility, comparisons were made between hollow beams and the currently used solid beams by the KUBLAI simulations.

6.2. Direct Energy Recovery from Spent Beams

6.2.1. Configuration for Direct Energy Recovery

[Figure 6.1](#) shows schematic diagram of a klystron with a 3-stage depressed collector. In the depressed collector, the injected spent electrons are electrostatically decelerated, and, then, slightly accelerated in the opposing direction onto the electrodes. This configuration is expected to suppress the secondary electrons from the electrode surfaces [\[2,3\]](#), which is otherwise led to losses.

The recovered power P_r , and the recovery efficiency η_r by an N -stage depressed collector are defined, respectively, by

$$P_r = \sum_{n=1}^N I_n V_n, \quad (6.1.a)$$

$$\eta_r = \frac{P_r}{P_s} = \frac{P_r}{P_b - P_{out}}, \quad (6.1.b)$$

where V_n , and I_n denote, respectively, the n -th electrode potential, and the beam current collected by the n -th electrode. The P_s , P_{out} , and P_b denote the power of the spent beam at the collector entrance, the RF output power of the klystron, and the power of the incident beam to the klystron, respectively. The overall efficiency η is, then, given in terms of η_r by,

$$\eta = \frac{P_{out}}{P_b - P_r} = \frac{P_{out}}{P_b - \eta_r(P_b - P_{out})} = \frac{\eta_0}{1 - \eta_r(1 - \eta_0)}, \quad (6.2)$$

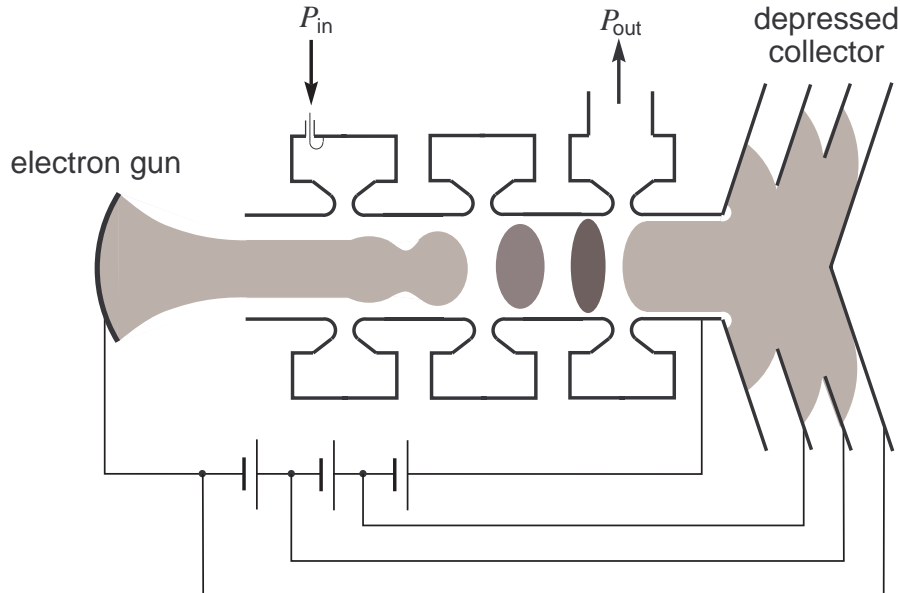


Figure 6.1. Schematic diagram of a klystron with a 3-stage depressed collector.

where η_0 denotes the efficiency without energy recovery, and is given by,

$$\eta_0 = \frac{P_{\text{out}}}{P_{\text{b}}} . \quad (6.3)$$

For the klystron with $\eta_0 = 60.5\%$, as shown in Fig. 6.2, around 75% efficiency could be achieved with 50% energy recovery.

In the following discussions in this chapter, the potential of the last stage electrode V_N is chosen to be equal to that of the cathode as shown in Fig. 6.1, just to simplify the power supply system without any additional higher voltages, and costs.

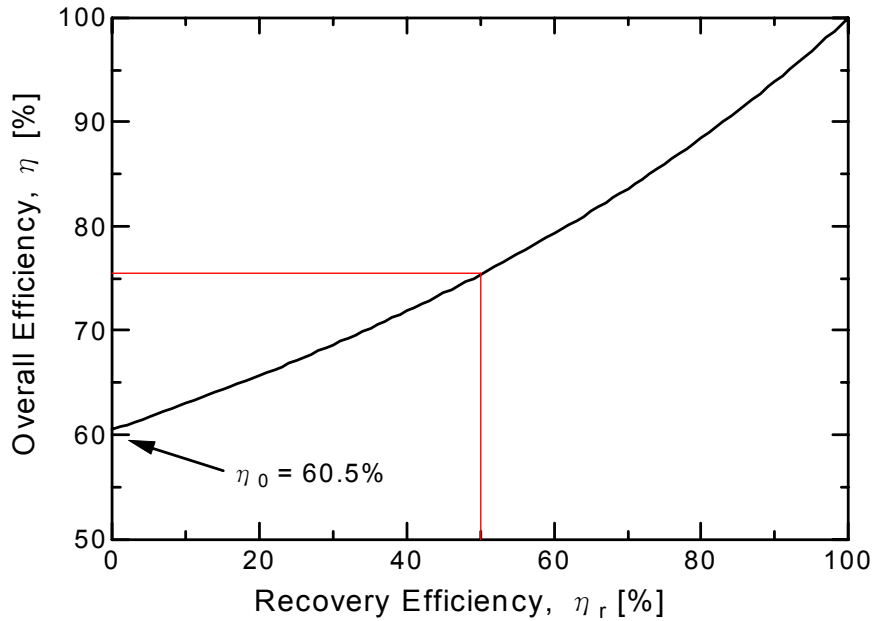


Figure 6.2. Overall efficiency as a function of recovery efficiency.

6.2.2. Evaluation of Theoretically Maximum Efficiencies

Figure 6.3 shows energy spectrum of spent beams for various output powers, obtained by the KUBLAI simulations. Under the following two assumptions that,

- (i) each electron is collected by the electrode with a potential slightly less than the incident kinetic energy,
- (ii) no secondary electron is yielded from the electrode surfaces,

then, the recovered power P_r is given from the energy spectrum dI/dV shown in Fig. 6.3, as follows,

$$P_r = \sum_{n=1}^{N-1} V_n \{I(V_{n+1}) - I(V_n)\} + V_N \{I_s - I(V_N)\}, \quad (6.4.a)$$

where, I_s denotes the total current of the incident spent beam, and is given by,

$$I(V) = \int_0^V \frac{dI}{dV} dV, \quad (6.4.b)$$

$$I_s = I(\infty). \quad (6.4.c)$$

From Eq. (6.4.a), the following expressions can be obtained, for $1 \leq n, m \leq N-1$,

$$\frac{\partial P_r}{\partial V_n} = I(V_{n+1}) - I(V_n) + (V_n - V_{n-1}) \frac{dI}{dV}(V_n), \quad (6.5.a)$$

$$\frac{\partial^2 P_r}{\partial V_n \partial V_m} = \begin{cases} -2 \frac{dI}{dV}(V_n) - (V_n - V_{n-1}) \frac{d^2 I}{dV^2}(V_n), & (n = m), \\ \frac{dI}{dV}(V_{\max(n,m)}), & (|m - n| = 1), \\ 0, & (|m - n| > 1). \end{cases} \quad (6.5.b)$$

With these expressions, the Newton method can be, then, applied, to find the optimized electrode potentials that give the theoretically maximum recovered power $P_{r,\max}$.

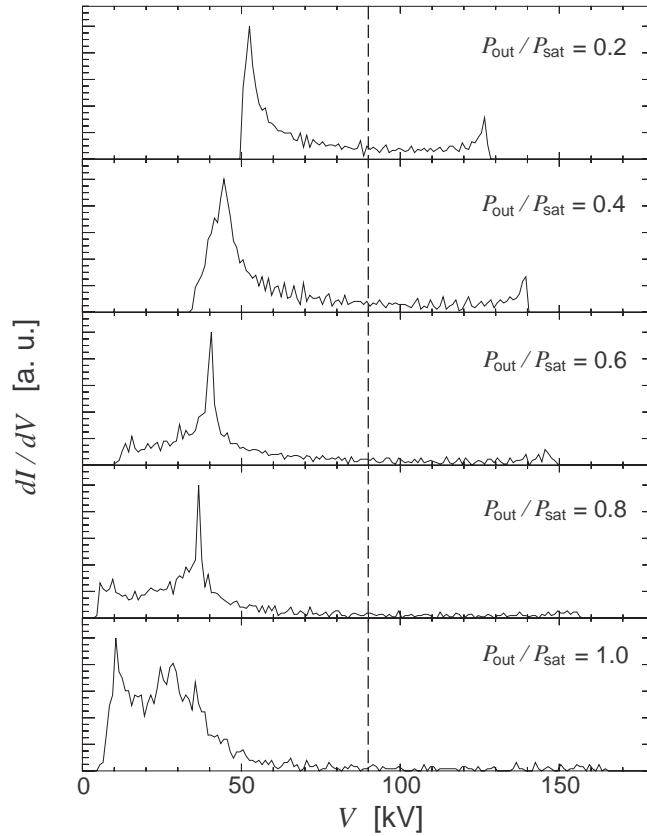


Figure 6.3. Energy spectrum of spent electron beams for various output powers (the saturated power $P_{\text{sat}} = 1.32 \text{ MW}$). The dashed line indicates the gun voltage $V_b = 90 \text{ kV}$.

The theoretically maximum recovery efficiencies $\eta_{r,\max}$, and overall efficiencies η_{\max} were calculated for the spent beams shown in Fig. 6.3, and for various number of stages N , with the optimized potentials.

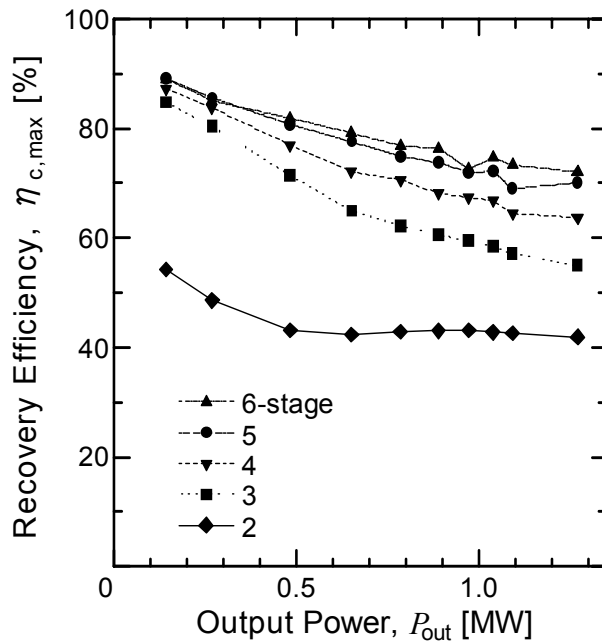
As shown in Fig. 6.4(a), it is found that the recovery efficiency $\eta_{r,\max}$ decreases with increasing P_{out} due to the broader energy spectrum of the spent beam. Nevertheless, as shown in Fig. 6.4(b), the overall efficiency η_{\max} is found to increase as P_{out} increases.

For the saturated P_{out} , more than 80 % overall efficiency could be theoretically achieved with a 5-stage depressed collector, and additional stages are found not to contribute appreciably to further enhancement. For the 5-stage collector at the saturated output, the optimized electrode potentials V_n , the currents I_n , and the heat loads $P_{\text{heat},n}$ onto the n -th electrode are summarized in Table 6.2, where the heat loads were calculated by,

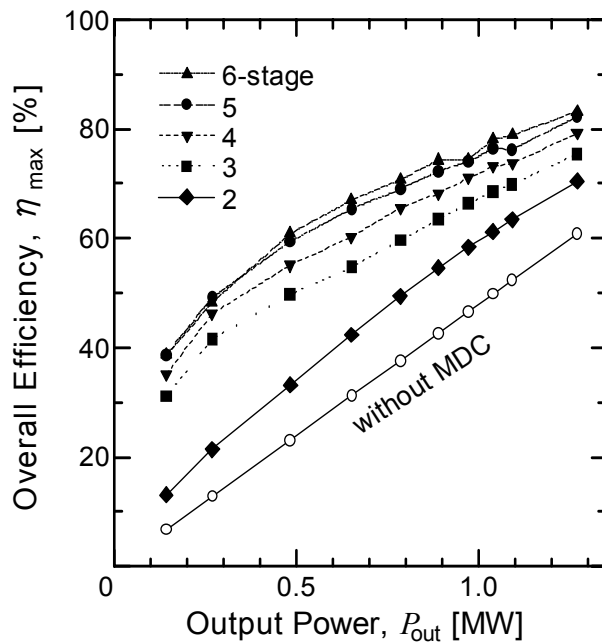
$$P_{\text{heat},n} = \int_{V_n}^{V_{n+1}} (V - V_n) \frac{dI}{dV} dV. \quad (6.6)$$

In the previous report on a collector design [1-3], the electrode potentials were chosen equally stepwise rather than the optimized ones, just to simplify the designing, and to reduce costs as well. To evaluate the degradation from the optimum value, the recovered power was also calculated from Eqs. (6.4) for the potentials equally stepwise, namely 18, 36, 54, 72, and 90 kV, and for the spent beam at the saturated output.

As summarized in Table 6.3, the overall efficiency was calculated as $\eta = 80.3$ %, which is very encouraging compared with $\eta_0 = 60.5$ %, although it is slightly less than the optimum, $\eta_{\max} = 83.7$ %.



(a) Theoretically maximum recovery efficiencies.



(b) Theoretically maximum overall efficiencies.

Figure 6.4. Theoretically maximum efficiencies as functions of output power.

Table 6.2. *Optimized electrode potentials for the saturated output, and corresponding electrode currents and heat loads, on the assumption of negligence of beam optics.*

electrode no.	potential [kV]	current [A]	heat-load [kW]
0	0	2.03	18.4
1	9.7	6.10	33.5
2	21.5	6.56	42.7
3	32.3	6.86	68.8
4	54.1	1.53	14.4
5	90	1.22	71.9

Table 6.3. *Recovery and overall efficiencies with the optimized potentials, and the potentials equally stepwise, on the assumption of negligence of beam optics.*

electrode potentials	recovery efficiency [%]	overall efficiency [%]
9.7, 21.5, 32.3, 54.1, 90 (optimized potentials)	71.1	83.7
18, 36, 54, 72, 90	62.4	80.3

6.2.3. Multistage Depressed Collector Design

A depressed collector was designed by use of the KUAD2 simulations, where the beam optics was taken into consideration.

The KUBLAI results on the positions and the velocities of the spent electrons were used as the injection conditions. Approximately, all the spent electrons were injected at a moment, and the electron trajectories were

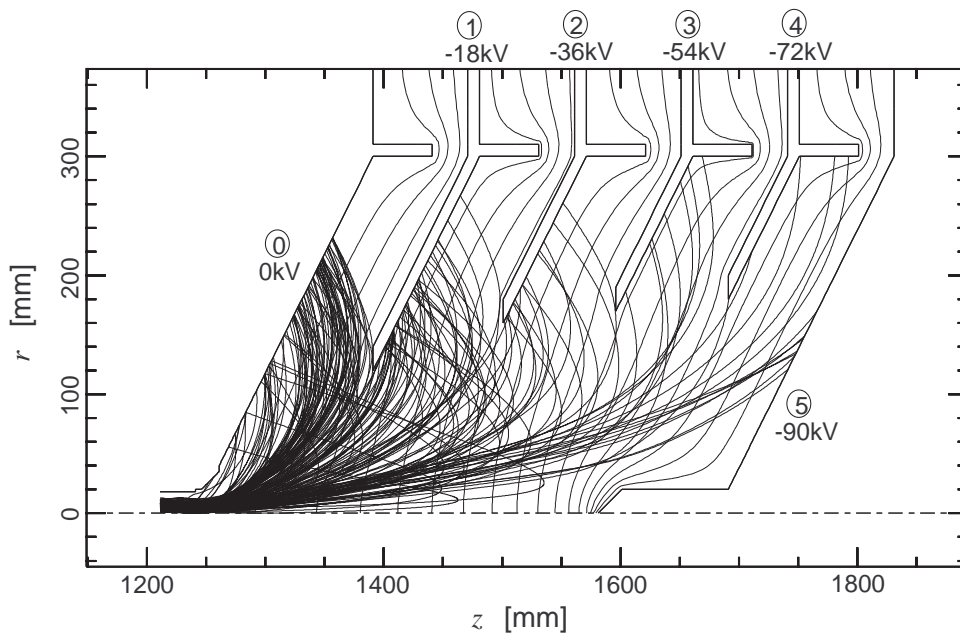
simulated in static fields. The trajectories of both the incident and the secondary electrons were simulated self-consistently.

Considering the results in [the previous subsection](#), the designed number of stages was chosen as $N = 5$, and the electrode potentials equally stepwise, for the reason that neither additional stages nor optimized potentials would result in appreciably further efficiency enhancement, while they would rather result in more complicated designing. Thus, only the electrode shapes were optimized, with trials and errors.

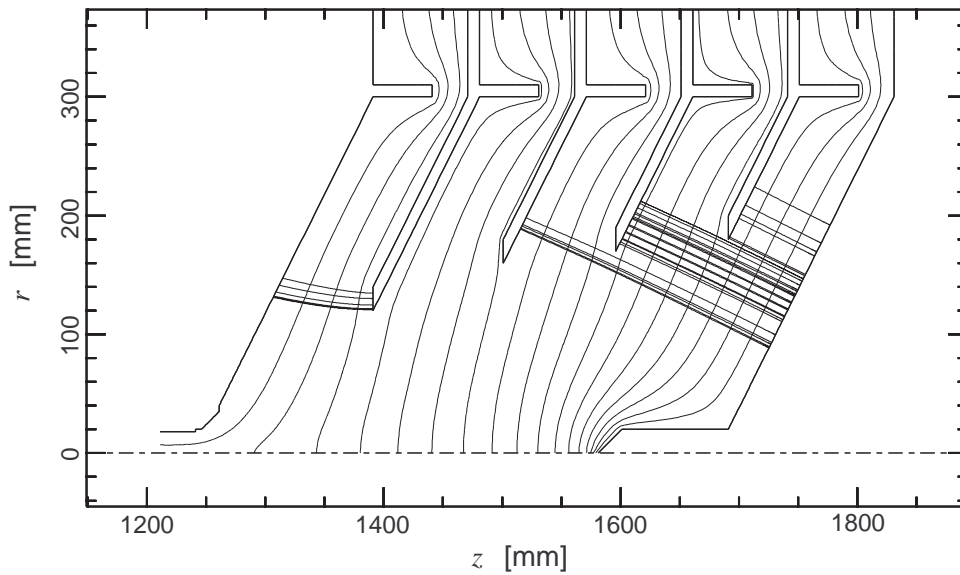
Repeated design refinements resulted in an optimized geometry shown in [Fig. 6.5](#). Care was taken to assure no electron backstreaming towards the collector entrance, which otherwise causes degradation in the klystron performance. The trajectories of the incident, and the secondary electrons from the electrode surfaces with the yield ratio of $\delta = 0.5$, are, respectively, shown in [Figs. 6.5\(a\) and \(b\)](#). The simulation results on the electrode currents are shown in [Table 6.4](#).

From [Table 6.4](#), the recovery efficiency was evaluated to be $\eta_r = 38.4\%$, leading to an overall efficiency of $\eta = 71.3\%$, which is also very encouraging compared with the 60.5% efficiency without a depressed collector. The obtained efficiencies are, however, lower than the theoretically maximum ones shown in [Table 6.3](#), and, therefore, there is still possibility of further enhancement by further design refinements.

As shown in [Fig. 6.5](#) and [Table 6.4](#), the secondary electrons from the 2nd to 4th electrodes are found to be suppressed successfully. Power loss due to the secondary electrons from the 1st and 5th electrodes is estimated to be 32 kW, leading to only 8.8% degradation in the recovered power (net of 332 kW).



(a) Incident electrons.



(b) Secondary electrons.

Figure 6.5. Equipotential lines and electron trajectories by the KUAD2 simulations in the 5-stage depressed collector.

Table 6.4. KUAD2 results on beam currents, and heat loads onto the MDC electrodes shown in Fig. 6.5.

electrode no.	secondary yield [A]	collected current [A]		heat load [kW]
		incident	secondary	
0	0.00	13.00	0.09	286
1	0.09	6.90	0.00	107
2	0.00	2.15	0.08	42
3	0.00	0.89	0.27	31
4	0.00	0.48	0.09	17
5	0.44	0.89	0.00	51

6.3. Efficiency Enhancement by use of Hollow Beams

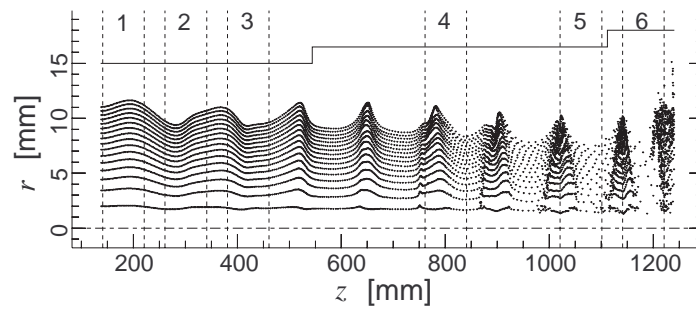
Hollow beams in the klystron drift-tube were simulated by the KUBLAI, and comparisons were made with the solid beam.

Figures 6.6(a), (b), and (c) show, respectively, the snapshots of the solid beam, and two hollow beams with different hollow radii r_h (see Fig. 6.7). The hollow beams were injected with the same beam radius $r_b = 11.2$ mm, and the same current of 24.3 A as the solid beam, while with different current densities according to their cross-sectional areas $\pi(r_b^2 - r_h^2)$.

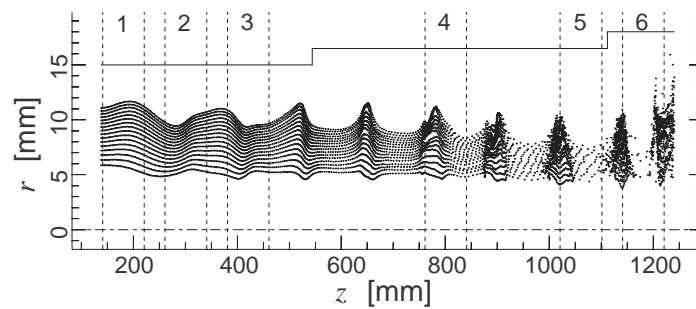
Table 6.5 shows calculated output powers with four different hollow radii, together with the solid beam. The hollow beams are certainly found to enhance the klystron efficiency, as was expected.

It is also found that the hollow radius of 7.92 mm results in less efficiency than the smaller hollow radii of 5.60, and 6.86 mm. The reason for this is supposed that a larger hollow results in a less bunched beam because of larger space-charge forces in the z -direction. Among the four hollow

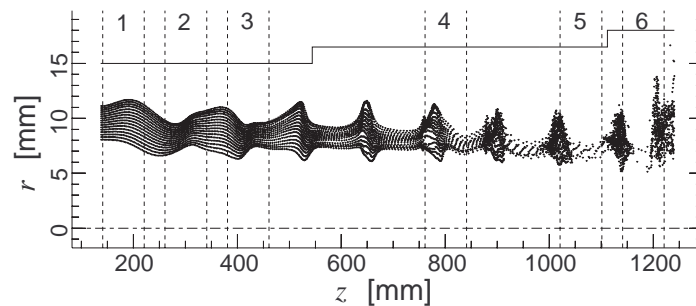
beams in [Table 6.5](#), the hollow radius of 5.60 mm gives the maximum efficiency of 67.0 %, which is very encouraging compared with the 60.5 % efficiency with the solid beam, although design of an electron gun to provide such a hollow beam with high accuracy is required.



(a) Solid beam.



(b) 5.6 mm hollow.



(c) 7.9 mm hollow.

Figure 6.6. Snapshots of solid and hollow beams in the drift-tube.

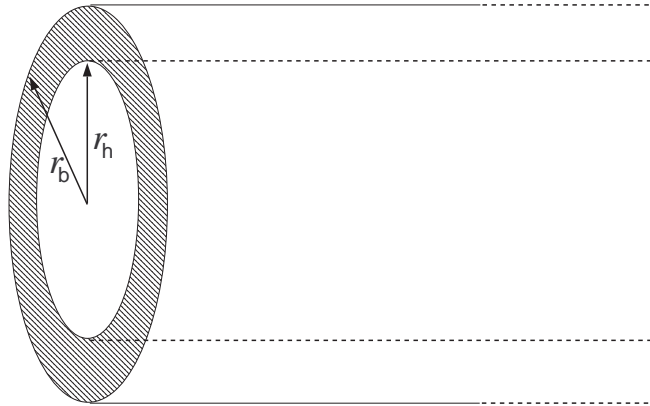


Figure 6.7. Description of the hollow radius r_h , and beam radius r_b of a hollow beam.

Table 6.5. KUBLAI results on efficiencies with hollow beams.

hollow radius* r_h [mm]	ratio of hollow area* r_h^2/r_b^2 [%]	efficiency [%]
0.00	0.0	60.5
3.96	12.5	64.6
5.60	25.0	67.0
6.86	37.5	66.8
7.92	50.0	66.2

*at injection boundary,

6.4. Concluding Remarks

In this chapter, the two approaches to the klystron efficiency enhancement were discussed.

Theoretical limit of energy recovery with depressed collectors was made clear. It is found that, as the RF output power increases, the overall

efficiency increases, despite the recovery efficiency decreases because of broader energy spread of the spent beam. It is also found that a 5-stage collector with electrode potentials equally stepwise could, theoretically, enhance the efficiency up to 80.3 %, from the 60.5 % efficiency without a depressed collector, and neither additional stages nor optimized potentials would result in appreciably further enhancement. A 5-stage depressed collector was designed by the KUAD2 simulations, to provide an enhanced efficiency of 71.3 %.

Hollow beams are found also to result in higher efficiencies than the currently used solid beam. With an optimum hollow radius, an enhanced efficiency of 67.0 % could be achieved. It is also found that a larger hollow than the optimum results in a lower efficiency due to larger longitudinal space-charge forces.

It is to be noted that the two above techniques could be applied simultaneously to a klystron, and are expected to enhance the efficiency much further.

Chapter 7

Summary

This thesis discusses performance characteristics of depressed collectors, and hollow beams aiming at appreciable enhancements of klystron efficiencies. Also presented are developments of a set of 2-dimensional numerical codes to investigate these two approaches. The results are summarized as follows.

(i) A new Finite Element eigenmode solver (KUEMS) has been developed in this study, aiming at improved accuracy in calculating cylindrically symmetric modes. Instead of H_θ , or rH_θ preferentially used so far in the existing codes, the quantity H_θ/r is newly used in this study to represent the electromagnetic fields.

This present Finite Element formulation is found to result in remarkably higher accuracy than the other formulations, particularly, in the eigenfrequency of the fundamental mode. It is also found to result in smoother convergence of the solutions with respect to number of the mesh points, to provide good extrapolation property.

(ii) Also developed was a solenoidal field solver (KUSOS) for calculating external focusing fields in klystrons. A new hybrid method is proposed,

which can deal with unbounded problems including nonlinear media by combining the Finite Element method and the Moment method.

The numerical results show good agreements with the analytical solutions, no difference in the numerical solutions for different choices of the picture frames, and excellent continuity of the calculated magnetic fields on the picture frames.

(iii) Two particle-in-cell simulation codes have been developed by modifying the existing codes. One is for simulations of electron trajectories in static fields (KUAD2). It was verified through comparisons of gun perveances with experiments, showing excellent agreements within $-2.3\% \sim +2.4\%$ relative errors.

The other is for simulations of interactions between electron beams and klystron cavities (KUBLAI). A modified Newmark method is proposed to stabilize the numerical instability in calculating simultaneously both electron motions, and beam-induced fields. Also proposed is a modified method for calculating cavity voltages, which eventually shows faster convergence to the steady-state solutions than the basic method.

Comparisons were also made between the KUBLAI simulations and experiments, showing excellent agreements within $-4.9\% \sim +6.9\%$ relative errors with respect to the saturated output powers of klystrons.

(iv) By use of the verified codes developed in this study, the aforementioned two approaches were investigated for the klystron efficiency enhancements.

Theoretical limit of the energy recovery with depressed collectors was evaluated. It is found that a 5-stage collector could, theoretically, enhance the efficiency up to 80.3% from the basic efficiency of 60.5%, and neither additional stages nor optimized potentials would enhance the

efficiency appreciably further. A 5-stage depressed collector was, then, designed through the KUAD2 simulations, leading to an enhanced efficiency of 71.3%, which is very encouraging compared with the 60.5% efficiency without depressed collectors.

Hollow beams are found also to result in higher efficiencies than the currently used solid beam. It is found that, with an optimized hollow radius, an enhanced efficiency of 67.0% could be achieved without depressed collectors. It is also found that larger hollows than the optimum tend to result in rather lower efficiencies.

In summary, the simulation codes newly developed in this study are found to be efficient in high-power klystron designing, and, also, by use of these numerical codes, either the depressed collectors, or the hollow beams are found, numerically, to result in appreciable efficiency enhancements of klystrons.

Acknowledgments

I am sincerely indebted to Professor Kiyoshi Yoshikawa for guiding and supporting my dissertation study, for his help at its various stages, and also for careful and patient elaboration of my thesis writing. I learned a lot from him on his rich background, deep insight, and his nonstop challenging spirit. Drs. Masami Ohnishi, Yasushi Yamamoto, and Mr. Hisayuki Toku also deserve my thanks for their support and many helpful discussions. I was truly fortunate to have advisors like them.

I would like to thank Professors Hiroshi Matsumoto, Kozo Hashimoto, and Dr. Masamitsu Nakajima for careful reading of this thesis, and many helpful discussions.

I would like to express my special thanks to Dr. Tsumoru Shintake, KEK, for giving me helpful advice from his experience of his FCI code development. His advice kept my code development out of trouble. I also would give my special thanks to Dr. Kohichiro Hirano, PNC, and research staffs of Toshiba for providing valuable experimental data for the code verifications. I could not develop my code without their help.

I also wish to thank Professor Shigeki Fukuda and Dr. Yong Ho Chin at KEK, Dr. Earl W. McCune at Varian, Professor Thomas Weiland and Dr. Ulrich Becker at Technische Hochschule Darmstadt, and also to Dr. Daryl Sprehn, SLAC, for many helpful discussions.

I also want to thank my friends at Yoshikawa Lab. for their help.

Finally, I want to thank my parents for their selfless encouragement and support.

References

- [1] K. Morita, *Microwave Tubes*, (Ohm, 1961), Chap. 4, in Japanese.
- [2] E. W. McCune, "A UHF-TV Klystron Using Multistage Depressed Collector Technology", IEEE, IEDM 86, pp. 160-163 (1986).
- [3] E. W. McCune, "Klystron Performance Using a Multistage Depressed Collector", IEEE, IEDM 87, pp.157-159 (1987).
- [4] Y. Yamamoto, T. Inamasu, K. Masuda, M. Ohnishi, K. Yoshikawa, H. Toku and E. Tanabe, "Simulation of Electron Backstream in a Microwave Thermionic Gun", Nucl. Instrum. Meth. A, vol. 393, pp.443-446 (1997)
- [5] D. Tsukahara, T. Inamasu, K. Yoshikawa, M. Ohnishi, Y. Yamamoto and K. Masuda, "Numerical Study of Electron Behaviors in RF-Gun", Proceedings of the 3rd Asian Symposium on Free Electron Lasers and 5th Symposium on FEL Applications, pp.183-188 (1997).
- [6] K. Masuda, T. Inamasu, M. Sobajima, J. Kitagaki, K. Yoshikawa, M. Ohnishi, Y. Yamamoto and H. Toku, "Short Pulse Electron Beam Characteristics in an RF Gun with a Photocathode", Proceedings of Towards X-Ray Free Electron Lasers Workshop, in press.
- [7] H. C. Hoyt, "Numerical Studies of the Shapes of Drift Tubes and Linac Cavities", Rev. Sci. Instrum., vol. 37, pp.153-155 (1965).

- [8] K. Halbach and R. F. Holsinger, "SUPERFISH-A Computer Program for Evaluation of RF Cavities with Cylindrical Symmetry", *Particle Accelerators*, vol. 7, pp.213-222 (1976).
- [9] A. G. Daikovsky, Y. I. Portugalov and a. D. Ryabov, "PRUD-Code for Calculation of the Nonsymmetric Modes in Axial Symmetric Cavities", *Particle Accelerators*, vol. 12, pp.59-64 (1982).
- [10] T. Weiland, "On the Unique Numerical Solution of Maxwellian Eigenvalue Problems in Three Dimensions", *Particle Accelerators*, vol. 17, pp.227-242 (1985).
- [11] A. G. Daikovsky Y. I. Partugalov and A. D. Ryabov, "PRUD-W: A New Code to Compute and Design Accelerating Structures", *Particle Accelerators*, 20, pp.23-43 (1986).
- [12] E. M. Nelson, "A 2D Field Solver for Periodic Structures with Special Corner Elements", SLAC-PUB-5532 (1991).
- [13] E. M. Nelson, "A Finite Element Field Solver for Dipole Modes", SLAC-PUB-5881 (1992).
- [14] T. Weiland, "High Precision Eigenmode Computation", *Particle Accelerators*, to be published.
- [15] K. Masuda, K. Yoshikawa, M. Ohnishi, Y. Yamamoto, H. Toku, M. Sobajima and J. Kitagaki, "Development of an Improved Two-Dimensional Finite Element Code for Cylindrically Symmetric Eigenmode", *IEEE Trans. Microwave Theory Tech.*, accepted on September 9, 1997, in press.
- [16] S. Yu, "Particle-in-Cell Simulation of High Power Klystrons",

SLAC/AP-34 (1984).

- [17] B. E. Carlsten and P. J. Tallerico, "Self-Consistent Klystron Simulations", IEEE Trans. on Nuclear Science, vol. NS-32, no. 5, pp. 2837-2839 (1985).
- [18] K. R. Eppley, "Algorithms for the Self-Consistent Simulation of High-Power Klystrons", SLAC-PUB-4622 (1988).
- [19] T. Shintake, "High Power Klystron Simulations Using FCI-Field Charge Interaction Code", KEK Report 90-3 (1990).
- [20] U. Becker, M. Dohlus and T. Weiland, "Three Dimensional Klystron Simulation", Particle Accelerators, to be published.
- [21] T. Shintake, "Development of FCI-Field Charge Interaction Code for High-Power Klystron Simulations", private communication.
- [22] K. Masuda, K. Yoshikawa, M. Ohnishi, Y. Yamamoto and M. Sobajima, "Direct Energy Conversion from Spent Electron Beam in High-Power CW Klystrons", Fusion Technology, vol.30, no. 3, pp.805-809 (1996).
- [23] K. Masuda, K. Yoshikawa, M. Ohnishi, Y. Yamamoto and M. Sobajima, "PIC Simulations on Improvement of Klystron Efficiency Enhancement for FEL Application", Proceedings of the 3rd Asian Symposium on Free Electron Lasers and 5th Symposium on FEL Applications, pp.213-219 (1997).
- [24] Y. Yamamoto, K. Yoshikawa and Y. Hattori, "Development of a Two-Dimensional Simulation Code (KUAD) Including Atomic Processes for Beam Direct Energy Conversion", IEEE, Proceeding of 12th Symposium on Fusion Engineering, pp. 1222-1226 (1987).

- [25] K. Fujisawa, *Microwave Circuits*, (Corona, 1960), Chap. 7, in Japanese.
- [26] C.R.I. Emson, "Methods for the Solution of Open-Boundary Electromagnetic-Field Problems", IEE Proceedings-A, vol. 135, no. 3, pp. 151-158 (1988).
- [27] X. Yuan, D. R. Lynch and J. W. Strohbehn, "Coupling of Finite Element and Moment Methods for Electromagnetic Scattering from Inhomogeneous Objects", IEEE Trans. Antennas Propagat., vol. 38, no. 3, pp. 386-393 (1990).
- [28] A. C. Cangellaris and R. Lee, "The Bymoment Method for Two-Dimensional Electromagnetic Scattering", IEEE Trans. Antennas Propagat., vol. 38, no. 9, pp. 1429-1437 (1990).
- [29] J. D. Collins, J. L. Volakis and J. M. Jin, "Combined Finite Element-Boundary Integral Formulation for Solution of Two-Dimensional Scattering Problems via CGFFT", IEEE Trans. Antennas Propagat., vol. 38, no. 11, pp. 1852-1858 (1990).
- [30] O. M. Ramahi and R. Mittra, "Finite Element Solution for a Class of Unbounded Geometries", IEEE Trans. Antennas Propagat., vol. 39, no. 2, pp. 244-250 (1991).
- [31] J. M. Jin and J. L. Volakis, "A Hybrid Finite Element Method for Scattering and Radiation by Microstrip Patch Antennas and Arrays Residing in a Cavity", IEEE Trans. Antennas Propagat., vol. 39, no. 11, pp. 1598-1604 (1991).
- [32] J. D. Collins, J. M. Jin and J. L. Volakis, "Eliminating Interior Resonances in Finite Element-Boundary Integral Methods for

- Scattering”, IEEE Trans. Antennas Propagat., vol. 40, no. 12, pp. 1583-1585 (1992).
- [33] M. A. Morgan and T. B. Welch, “Field Feedback Computation of Scattering by 2-D Penetrable Objects”, IEEE Trans. Antennas Propagat., vol. 40, no. 4, pp. 445-450 (1992).
- [34] G. Pelosi, A. Freni and R. Coccioli, “Hybrid Technique for analyzing Scattering from Periodic Structures”, IEE Proceedings-H, vol. 140, no. 2, pp. 65-70 (1993).
- [35] T. F. Eibert and V. Hansen, “3-D FEM/BEM-Hybrid Approach Based on a General Formulation of Huygens’ Principle for Planar Layered Media”, IEEE Trans. Microwave Theory Tech., vol. 45, no. 7 (1997)
- [36] B. H. McDonald and A. Wexler, “Finite-Element Solution of Unbounded Field Problems”, IEEE Trans. Microwave Theory Tech., vol. 20, no. 12, pp. 841-847 (1972).
- [37] T. Onuki, T. Nakata and S. Nemoto, *Finite Element Method for Electrical Engineering*, (Ohm, 1983), Chap. 7, in Japanese.
- [38] O. C. Zienkiewicz, *The Finite Element Method in Engineering Science*, (McGraw-Hill, 1971), Chap. 8.
- [39] D. Tsukahara, master thesis, Kyoto University (1997), in Japanese.
- [40] S. Humphries, *Charged Particle Beams*, (Wiley, 1990), Chap. 7.
- [41] H. Togawa, *Numerical Methods for Differential Equations*, (Ohm, 1973), Chap. 5, in Japanese.

